Polymer-Derived Microporous Ceramic Coated Sensors for Selective H₂/CO Sensing

A Thesis Submitted

In Partial Fulfillment of the Requirements

for the Degree of

DOCTOR OF PHILOSOPHY

by

Binod Kumar

(2016MSZ0001)

DEPARTMENT OF METALLURGICAL AND MATERIALS ENGINEERING
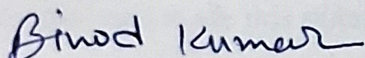
INDIAN INSTITUTE OF TECHNOLOGY ROPAR
September 2023

DEDICATED
TO
My Mother and Father
Dhanrajiya Devi & Sudarshan Ram

Declaration of Originality

I hereby declare that the work which is being presented in the thesis entitled **Polymer-Derived Microporous Ceramic Coated Sensors for Selective H_2/CO Sensing** has been solely authored by me. It presents the result of my own independent investigation/research conducted during the time period from July 2016 to September 2023 under the supervision of Dr. Ravi Mohan Prasad, Assistant Professor, Indian Institute of Technology Ropar. To the best of my knowledge, it is an original work, both in terms of research content and narrative, and has not been submitted or accepted elsewhere, in part or in full, for the award of any degree, diploma, fellowship, associateship, or similar title of any university or institution. Further, due credit has been attributed to the relevant state-of-the-art and collaborations (if any) with appropriate citations and acknowledgments, in line with established ethical norms and practices. I also declare that any idea/data/fact/source stated in my thesis has not been fabricated/ falsified/ misrepresented. All the principles of academic honesty and integrity have been followed. I fully understand that if the thesis is found to be unoriginal, fabricated, or plagiarized, the Institute reserves the right to withdraw the thesis from its archive and revoke the associated Degree conferred. Additionally, the Institute also reserves the right to appraise all concerned sections of society of the matter for their information and necessary action (if any). If accepted, I hereby consent for my thesis to be available online in the Institute's Open Access repository, inter-library loan, and the title & abstract to be made available to outside organizations.

Binod Kumar

Signature

Name: Binod Kumar

Entry Number: 2016MSZ0001

Program: Ph.D.

Department: Metallurgical and Materials Engineering

Indian Institute of Technology Ropar

Rupnagar, Punjab 140001

Date: 24-06-2024

Acknowledgements

I would like to give special thanks to my PhD supervisor, **Dr. Ravi Mohan Prasad**, Department of Metallurgical and Materials Engineering, IIT Ropar for all of his help, support, and encouragement during this research project. Despite their busy schedule, he always made time for me, encouraged me to think for myself, and was willing to have in-depth conversations with me about my research when I needed them. Their dedication to hard work, honesty, and humility have been tremendous role models for me.
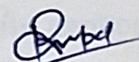
Dr. Pratik K. Ray, Chair of my Doctoral Committee and Head of the Department of Metallurgical and Materials Engineering, has been very helpful and supportive during my time in research work. Doctoral Committee members Dr. Prabhat K. Agnihotri, Dr. Dhiraj K. Mahajan, and Dr T. J. Dhilip from the departments of mechanical engineering and chemistry, respectively, for their unflagging attention to detail and constructive criticism during the course of the project.

I personally thank my colleagues, who have supported my work and stimulated my interest in research in various ways: **Mr. Rajesh Bura, Mr. Vishnu Girish C**. Moreover, I would like to thanks the efforts and help provided by **Mr. Ram Kumar** throughout my PhD work.

My deepest gratitude goes to my family for their constant love and support throughout my life. Thanks to my father **Mr. Sudarshan Ram** and my mother **Mrs. Dhanrajiya Devi** for their immeasurable sacrifices and blessings. They always soften the life difficulties for me and I owe all my achievements, including this, to them. It is due to all these individuals who had put forth the effort and made this uphill task possible for me.

Certificate

This is to certify that the thesis entitled **Polymer-Derived Microporous Ceramic Coated Sensors for Selective H₂/CO Sensing**, submitted by **Binod Kumar (2016MSZ0001)** for the award of the degree of **Doctor of Philosophy** of Indian Institute of Technology Ropar, is a record of bonafide research work carried out under my guidance and supervision. To the best of my knowledge and belief, the work presented in this thesis is original and has not been submitted, either in part or full, for the award of any other degree, diploma, fellowship, associateship or similar title of any university or institution. In my opinion, the thesis has reached the standard fulfilling the requirements of the regulations relating to the Degree.

Signature of the Supervisor

Dr. Ravi Mohan Prasad

Department of Metallurgical and Materials Engineering

Indian Institute of Technology Ropar

Rupnagar, Punjab 140001

Date: 24-6-2024

Abstract

Currently, most of the hydrogen is produced through steam reforming of methane. Methane reforming and water gas shift reactions are often not completed, leaving very small concentration of CO (∼50 ppm) in the fuel stream. Trace amount of CO (few ppm) causes a substantial degradation in the fuel cell performance as CO acts as poison for Pt-based catalysts, therefore, residual CO concentration in the hydrogen rich stream should be controlled. Rapid and accurate hydrogen detection in the presence of other interfering gases (e.g. detection of H_2 in the presence of CO) is necessary during the production, storage and use of hydrogen. It is also essential for monitoring/controlling the hydrogen concentration in nuclear reactors, coal mines, semiconductor manufacturing, etc.

The main goal of the present work is to investigate the suitability of polymer-derived microporous ceramic filters for their applications in enhancing H_2/CO gas sensing selectivity of chemiresistor gas sensors by integrating filters with chemiresistors. Polymer-derived ceramics possess thermochemical stability and tunable porosity, hence, can be applied for applications in harsh reducing conditions. In the present work, various types of ceramics are synthesized by polymer-pyrolysis route and their performance in the enhancement of gas sensing selectivity have been evaluated.

Commercially available vinyl-functionalized polysiloxane, polysilazane and ally hydrido polycarbosilane have been selected as pre-ceramic polymers and are pyrolyzed at 700 °C, 800 °C and 900 °C in argon atmosphere. Polymer-to-ceramic transformation, structural characterizations and porosity characteristics of the synthesized ceramics are investigated. All synthesized ceramics were x-ray amorphous. Porosity characterization of the synthesized ceramics shows that SiOC ceramics are microporous in nature where as SiCN and SiC derived from polymers are found to be non-porous. Moreover, SiOC ceramics obtained at 700 °C are microporous with a mean pore-size of about 4.6 Å as measured using nitrogen physisorption method.

Microporous SiOC ceramics layers are coated on SnO_2- and GaN-based planar chemiresistors with a thickness of about 5-6 μm by dip-coating of polysiloxane solution on planar chemiresistors followed by pyrolysis at 700 °C under argon atmosphere. The diameter of micropores in SiOC (~4.6 Å) is larger than the kinetic diameter of H_2 (2.89 Å) and CO (3.76 Å)

molecules, allowing in this way their diffusion towards the bottom sensing layer. Transient response characteristics and sensor signals of uncoated- and two-fold SiOC-coated sensors exposed to CO (50, 70 and 100 ppm) and H_2 (50, 500 and 1000 ppm) in nitrogen at 400 °C have been performed. The results indicate that uncoated sensors show high response towards both CO and H_2 whereas for microporous SiOC coated gas sensors the sensitivity towards the interfering gas CO is significantly reduced.

Keywords: Polymer-Derived Ceramics; Microporous; Filter; Hydrogen; Gas Sensor; Selectivity.

List of Publications

1. <u>B. Kumar</u> and R.M. Prasad, Polymer-derived microporous SiOC ceramic coated gallium nitride sensor for selective H_2/CO detection, *Sensors and Actuators B: Chemical*, 379 (2023) 133226.

2. R. Bura, <u>B. Kumar</u>, and R.M. Prasad, Polymer-derived SiOC ceramic coating for corrosion protection, *International Journal of Applied Ceramic Technology*, 21 (2024) 900-909.

3. <u>B. Kumar</u>, R. Bura, and R.M. Prasad, Amorphous microporous SiOC-coated SnO_2 sensor for selective hydrogen sensing application (*communicated*).

Table of Contents

List of Figures

List of Tables

Notations and Abbreviations

ATR-IR   Attenuated total reflection infrared

BJH   Barrett-Joyner-Halenda

BET   Brunauer-Emmett-Teller

CVD   Chemical vapour deposition

DFT   density functional theory

DAC   Data acquisition system

DC   Direct current

EDS   Energy dispersive spectroscopy

GPIB   General purpose interface bus

GUI   Graphical user interface

GFR   Gas flow rate

IDT   Interdigital transducer

LSPR   Localized surface plasmon resonance

LabVIEW   Laboratory virtual instrument engineering workbench

MFC   Mass flow controller

MF   Microfiltration

MOF   Metal oxide Framework

NIR   Near Infrared

NMR   Nuclear magnetic resonance

NF   Nanofiltration

PSD   Pore size distribution

PDC   Polymer-derived ceramic

RF   Radio frequency

SF   Saito and Foley

SPR   Surface plasmon resonance

SEM   Scanning electron microscopy

TGA   Thermal gravimetric analysis

UF   Ultrafiltration

USB   Universal serial bus

VISA	Virtual instrument software architecture
XRD	X-ray diffraction

Symbols

R_g	Resistance in gas
R_a	Resistance in air
S	Sensitivity
α	Absorption coefficient of the gas
$I(0)$	Emitted optical intensity
r_k	Radius of curvature of the gas-liquid interface
R	Universal gas constant
v_m	Molar volume of the gas phase
T	Temperature
P_{sat}	Saturated vapor pressure
γ	Surface tension of the gas-liquid interface
d_p	Pore diameter
r_p	Pore radius
λ	Mean free path
K_n	Knudsen number
P_K	Knudsen diffusion the permeance
M	Molecular weight
L	Membrane thickness
ε	Porosity of the membrane
E_a	Activation energy
P_o	Pre-exponential factor
J	Diffusive flux
k	Hydrogen permeability of the metal
P_p	Hydrogen partial pressures
$°C$	Degree celsius
h	Hour
m	Meter

K	Kelvin
C_g	Gas concertation
$sccm$	Standard cubic centimeters per minute
$\mathring{A}$	Angstrom
cm^{-1}	Wavenumber
ppm	Parts per million
ppb	Parts per billion
g	Gram
s	Second
τ	Tortuosity
p	Vapor pressure
W	Watt

Introduction and Motivation

Successful development of gas sensors should possess three important characteristics: sensitivity, selectivity and stability. Among the well-known gas sensitive oxides (SnO_2, ZnO, TiO_2, Cr_2O_3, WO_3 and In_2O_3), SnO_2 is most commonly used for detection of toxic and combustible gases. Metal oxide gas sensors generally show high sensitivity but poor selectivity if pure sensing material is used and are also not stable in hydrogen-rich atmospheres at high temperatures. In the last few years nitrides and oxynitrides, such as GaN and GaON have attracted an increased attention in the detection of H_2, CO, CH_4, and NH_3 in harsh reducing conditions. However, these sensors behave more or less similar to various reducing gases (H_2, CO, etc.), which could lead to false alarm and error in gas concentrations measured by detectors due to difficulty in separating the effects of different gases.

Currently, hydrogen is mainly produced through steam reforming of methane. Methane reforming and water gas shift reactions are aften not completed, leaving very small concentration of CO (~50 ppm) in the fuel stream. As CO acts as poison for Pt-based catalysts, even a few ppm of CO causes a substantial degradation in the fuel cell performance. Therefore, accurate hydrogen detection in the presence of other interfering gases (CO, humidity) is necessary during the hydrogen production and storage.

Among the various ways of enhancement of gas sensor selectivity ─ by use of (i) catalysts, (ii) temperature control, (iii) specific surface additives, and (iv) physical or chemical filters on the top of sensing materials ─ one of the effective methods of enhancing gas sensing selectivity is to apply a thermally stable porous filter layer on sensing materials. Recently reported works show improving H_2 selectivity against CO using Au-loaded SnO_2, palladium-capped copper oxide (Pd/CuO) thin films and by temperature modulation of the SnO_2-based metal oxide sensor with the addition of PdO_x. A well-defined microporous (pore diameter < 2 nm) filter layer can block larger CO molecules from diffusing towards sensing materials by allowing smaller H_2 molecules for selective H_2 detection. Microporous polymer-derived ceramics (SiC, SiOC, SiCN, etc.) are excellent candidates due to their thermochemical stability and tunable porosity.

The research work of this thesis is focused on:

(i)   Synthesis and characterization of microporous ceramics using polymer-pyrolysis route,

(ii)   Integration of microporous polymer-derived ceramics with chemiresistors,

(iii)   Enhancing gas sensing selectivity of H₂ with respect to CO using microporous ceramic-coated sensors.

This thesis is organized as follows:

Chapter 1. **Introduction and literature review**: The first chapter of the thesis provides an introduction to chemiresistive gas sensors and polymer-derived ceramics with exhaustive literature survey, definition of problem, and specific objectives of the thesis.

Chapter 2. **Experimental procedures**: This chapter presents the experimental procedure used for the synthesis of ceramic materials (using polymer-pyrolysis route), gas sensors (using RF/DC sputtering and screen printing methods) and also briefly describes various structural characterization methods applied in this work.

Chapter 3. **Design and realization of experimental gas sensing set-up**: This chapter describes the design and operation principle of a laboratory-scale gas sensing set-up and which has been realized during the present research work. The set-up mainly consists of mass flow controllers, multimeters, power sources and communication systems. A LABVIEW program was developed to control the set-up and acquire real time data during gas sensing measurements.

Chapter 4. **Synthesis of microporous polymer-derived ceramics**: This chapter investigates various types of precursors (polysilazane, polysiloxane and polycarbosilane) used for the synthesis and selection of suitable microporous (pore size < 2 nm) ceramics. Precursors were pyrolyzed under inert environment up to 800 °C and pore-size characteristics were studied using nitrogen adsorption-desorption method.

Chapter 5. **Microporous SiOC-coated SnO₂ and SiOC-coated GaN sensors**: In this chapter enhancement of H₂/CO selectivity of SnO₂ and GaN sensors coated with amorphous microporous silicon oxycarbide (SiOC) filter layer has been discussed. Amorphous SiOC ceramic has been synthesized by pyrolysis of vinyl-functionalized polysiloxane at 700 °C under argon. SiOC layer

was coated on sensor substrate by two-fold coating/pyrolysis steps. Transient response characteristics and sensor signals of uncoated sensors and SiOC-coated sensors were measured towards H_2 and CO at 400 °C.

Chapter 6. **Conclusions and outlook**: This chapter summarizes the present study and underlines its prospective future by evaluating the obtained results in terms of gas selectivity performances of integrated porous ceramic and sensor combinations.

Chapter 1. Literature review

Hydrogen is an odorless and colorless gas with highly flammable properties, commonly used in various industrial research applications. For instance, it has significant affinity towards moisture, which must be prevented in aluminum melting processes and galvanic plating to avoid hydrogen embrittlement. In nuclear reactors, hydrogen gas is used for safety monitoring, while in coal mines, its low-temperature oxidation produces gas at the ppm level, requiring monitoring to prevent accidental explosions. In transformer lubrication oil, there is a possibility of hydrogen gas leakage in power plants. In the semiconductor industry, hydrogen gas is used for thin film deposition, making controlled monitoring and detection crucial. Additionally, in the shuttle launching and aerospace industries, hydrogen leak detection is necessary. As the use of hydrogen as an energy source is rapidly growing, continuous monitoring of hydrogen leakage is essential for safety in hydrogen production, storage, and transportation[1].

1.1 Gas sensors

A gas sensor is a transducer that responds to changes in the concentration of a specific gas by producing a measurable output signal, typically in the form of voltage, current, or resistance, through a chemical, physical, or electronic process [2].

Gas Sensor

Gas molecules ⟶ | Receptor (Chemical) : Transducer (Physical) | ⟶ Signal
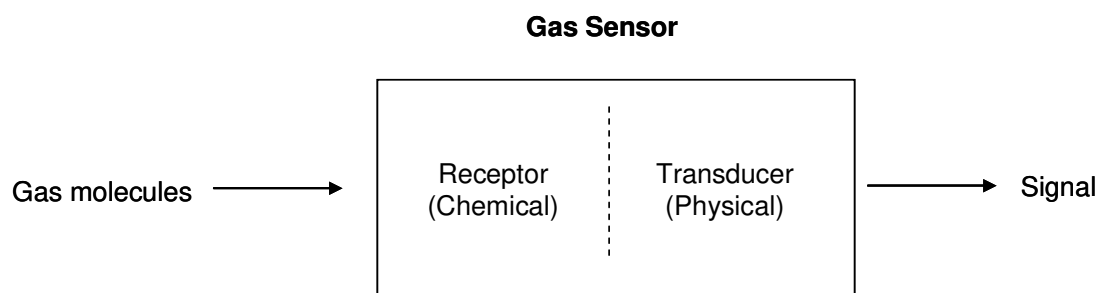
Figure 1.1 Construction of gas sensors with receptor and transducer (adapted from reference [3]).

Gas sensors are typically assembled by integrating two primary functions — the first function involves the identification of gas molecules, while the second function is responsible for converting this identification into a signal output, as illustrated in Figure 1.1. Gas recognition primarily occurs through the interaction of gas molecules, including adsorption and chemical reactions, with a selected material known as the receptor. This interaction results in various

physical or chemical effects that affect the receptors or their surroundings, such as the formation of reaction products, the generation of heat, or changes in the mass or dimensions of the receptor. These effects can then be transformed into electrical or optical signals by exploiting specific material properties, known as transducers.

1.1.1 Basic characteristics of gas sensors

Chemiresistor sensors, which are based on semiconductors, are commonly used for detecting poisonous and flammable gases because of their low cost and ease of use. In a chemiresistive gas sensor, the interaction between the gas and the semiconductor causes the electrical resistance to change. When exposed to the analyzing gases, the electrical resistance of the chemiresistive sensor changes (increases or decreases). As can be seen in Figure 1.2, the change in resistance is caused by the presence of either a reducing or oxidizing gas, and the type of sensing materials used. Under normal (with oxygen and humidity) atmosphere, optimal operating temperature range of these sensors is between 100 and 500 °C.
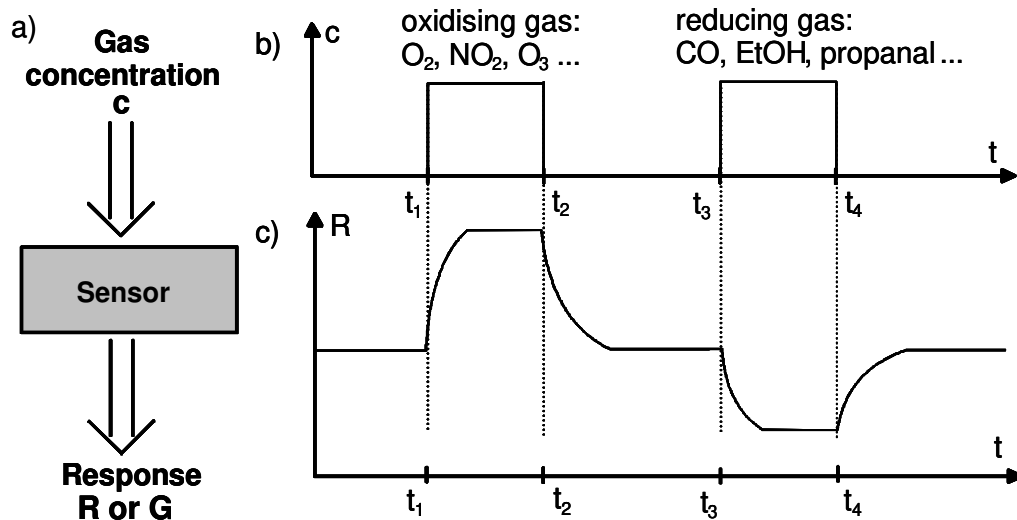
Figure 1.2 Sensor working principle: (a) functioning of a metal-oxide-based gas sensor, (b) the gas is applied at t_1, t_3 and removed at t_2, t_4, (c) which lead to changes in the resistance R or conductance G of the sensor (adapted from reference [4]).

Some of the important characteristics (basic terminologies) of gas sensors are mentioned below [3]:

1.1.1.1 Sensitivity or Response

It is defined as response to small concentration change of gases. It is mathematically expressed as sensor signal (S) which is the ratio of resistance of sensor in air to that in target gas. Under reducing type of target gases S is determined as R_a/R_g, while for oxidizing target gases it is calculated as R_g/R_a. Here, R_a signifies the resistance of gas sensors in the reference gas, typically air, while R_g denotes the resistance in the target gas.

1.1.1.2 Response Time and Recovery Time

In gas sensors, "response time" denotes the time taken by the sensor to respond as the sensor resistance changes moves from its initial state to a specific value and stabilizes at roughly 90% of its maximum value. "Recovery time" is defined as the time during which the sensor resistance reduces to the 10% of the saturation value after the gas flow stops.

1.1.1.3 Selectivity

Selectivity in gas sensors refers to the ability of a sensor to distinguish between different gases or vapors in a mixture. It is determined by the degree of response of the sensor to a target gas relative to other interfering gases in the environment. In other words, the selectivity of a gas sensor is its ability to respond to a specific gas while being insensitive to other gases. This property is critical for accurate and reliable detection of target gases in complex and diverse environments. A high level of selectivity is often achieved through the use of advanced sensing materials, such as selective coatings, functionalized nanostructures, and molecularly imprinted polymers, as well as through signal processing algorithms and pattern recognition techniques.

1.1.1.4 Stability

It is defined as the ability of the sensor to maintain its properties when operated continuously for long time under extreme conditions. A good sensor should work for several years without showing significant degradation in the performance.

1.1.2 Types of gas sensors

The choice of gas sensor depends on factors such as the target gas, sensitivity, selectivity, response time, and the intended application. Different sensors are suited for different environments and

requirements. Some of the commonly used type of gas sensors are categorized below based on their working principle.

1.1.2.1 Optical sensor

Optical sensors possess the capability to perceive light within specific segments of the electromagnetic spectrum, including ultraviolet, visible, and infrared regions. These optical gas sensors operation principle are based on parameters that detects wavelength, frequency, or polarization of light by converting this parameters into electrical signals through the photoelectric effect. The presence of gas molecules causes the change absorbance, luminescence, or refractive index of the material resulting in a change in the output signal [5].

In Figure 1.3, an illustrative example of an operational optical methane gas sensor is shown. This sensor comprises three main components: a light source that generates mid-IR light, a tube that contains the gas sample under examination, and an optical spectrum detector. The mid-IR light emitted by the light source travels through the gas sample, bouncing off the inner walls of the tube. Within the gas, molecules resonate at infrared frequencies, leading them to absorb some of the infrared radiation emitted by the light source. After passing through the gas sample, the infrared light reaches the optical spectrum detector, which measures the intensity of the emitted light. By comparing the input and output light intensities from the light source and considering the distance the light traveled, we can calculate the effective absorption coefficient of the gas. This coefficient is a crucial parameter used to determine the presence of methane in the gas sample."
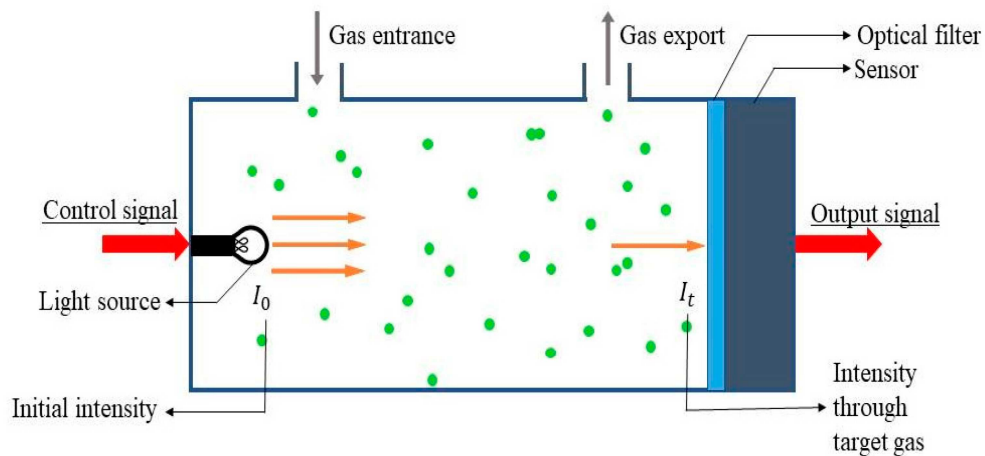
Figure 1.3 Schematic of an optical gas sensor (adapted from reference [6])

1.1.2.2 Electrochemical sensor

Electrochemical sensors measure a target gas's concentration by generating a voltage or current signal in response to a chemical reaction. The sensor, which has two electrodes (a working electrode and a counter electrode), functions by enabling charged molecules to diffuse across an electrolyte membrane. As shown in the Figure 1.4.
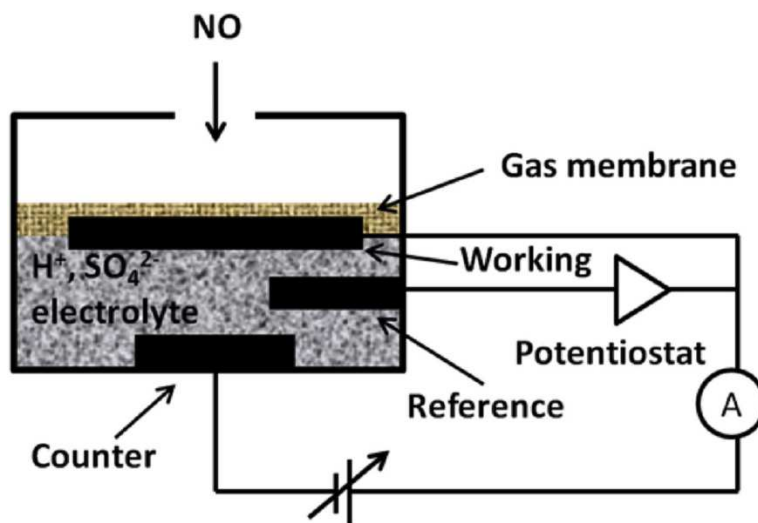
Figure 1.4 Schematic of electrochemical gas sensor (adapted from [7]).

1.1.2.3 Acoustic sensor

Microphones and other acoustic sensors (also known as "sound sensors") function by transforming acoustic energy into electrical currents. Sound-induced pressure changes in the air are detected by these sensors, and the resulting changes are converted into electrical signals.

Sound is absorbed in two ways: the first, classically, is caused by transport phenomena such heat conduction, viscosity, and diffusion; the second, non-classically, is caused by thermal relaxation involving the vibrational and rotational levels of the molecules. Energy is transferred between molecules in a gaseous medium through collisions. Without any external disturbances, the gas molecules' inherent degrees of freedom, such as vibration and rotation, quickly become thermalized. The gas thus remains at a fixed temperature in a state of thermal equilibrium. The release of an acoustic wave into the gas disrupts this equilibrium, causing the internal degrees of freedom DOF activated by collisions to return to their thermal state at the acoustic temperature. In

most cases, the acoustic wave does not quickly regain the energy it expended in order to activate the internal degrees of freedom of the molecules [8].

1.1.2.4 Catalytic Sensor

For almost a century, catalytic sensors have been utilized for fuel gas detection. In 1923, Jonson invented the first catalytic combustion sensor for detecting methane in mines[9, 10]. These sensors are primarily used for detecting fuel petrol and vapors. A chemical reaction occurs when fuel gases reach the temperature of combustion, and they are not ignited until that point. The detector element is made of catalytic material that reacts with fuel gases, while the compensator element remains inert. When fuel gas burns on the detector element, it decreases its resistance by increasing its temperature. The compensator temperature and resistance, however, remain constant as the fuel gas does not burn on the compensator. In the past, platinum filaments were used to achieve the ideal electrical current temperature, but they evaporate at temperatures exceeding 1000 °C. This issue was resolved by coating platinum with metal oxides [11]. A Wheatstone bridge circuit maintains formal equilibrium in pure air without fuel gases by using a variable resistor. When fuel gases are present, the detector device's resistance increases, causing a bridge circuit difference and an output voltage signal. The output voltage signal is determined by the concentration of combustible gas. These detectors are not sensitive at ppm levels.

1.1.2.5 Colorimetric sensor

Colorimetric gas sensors are devices that utilise colour change reactions to detect the presence and concentration of a particular gas. These sensors can be used in a variety of applications. This is accomplished through the utilisation of chemically sensitive materials, which, when exposed to the target gas, go through a noticeable colour change.

1.1.2.6 Metal oxide based gas sensors

In 1950s two scientist Brattain and Bardeen demonstrated the change in resistance of Ge depending upon the atmosphere in the bel laboratories [12]. Later on the first resistive gas sensor was introduce in early 1960 by Seyama, which was based on ZnO sensing layer based gas sensor operated at 485 °C [13]. Taguchi fabricated the first SnO_2 based gas sensor and patented in the 1970s. Seyama and Taguchi pioneered the use of metal oxide semiconductors (MOS) as gas sensors [14]. As flammable gases come into contact with metal oxides they excite a new electron level inside the solid and alter the electrical resistance of the gas sensing component. As a result,

this type of gas sensor involves altering the resistance or conductivity of the sensing material in response to target gas contact. Since metal salts are abundant on the earth surface further gas sensitivity research is focusing on them because they are readily accessible, cost-effective, simple to handle, highly stable, strong, durable, and unreactive when metal oxides are formed as well as being environmentally friendly. They can be transformed into their nanostructured oxides using a variety of techniques including sol-gel, chemical vapor deposition, hydrothermal and microwave. Metal oxides have attracted researchers due to their practical applications in optoelectronics, catalysis, medicine, environmental remediation, renewable energy, solar cells, biological applications, and sensors.

Numerous metal oxide semiconductors exhibit wide band gaps and electrical conductivity differences depending on the amount of gases that surround it. Due to their high sensitivity, rapid reaction selectivity and ability to recovery for more gases than any other detector semiconductor gas sensors produce substantial results [15]. Far more work is being done to optimize sensor efficiency through the addition of catalysts, noble metal doping, and metal oxide doping, increasing porosity, decreasing particle size, and increasing the sensor surface area. By carefully controlling all of these parameters metal oxide semiconductors can achieve high sensitivity and selectivity owing to the ease with which chemical reactions occur and charges are transferred to the surface semiconductor [16].

Table 1.1 Various metal-oxide based chemiresistive materials, additives and the analyzing gases which can be detected (data taken from reference [3]).

Base metal-oxides	Additives	Analyzing gas
Al_2O_3	Al, SiO_2/Si	Humidity, CH_4, NH_3
Bi_2O_3	Sb_2O_3	Smoke, CO, NO
CdO	$ZnFe_2O_4$	Ethanol
Cr_2O_3	TiO_2	NO_2, O_2, NH_3, Humidity

Co_3O_4	SiO_2	NH_3, CO_2, CH_4, C_3H_8, H_2, NO_2, Cl
CuO	SnO_2	CO, Ethanol, H_2S
Fe_2O_3	Au, Zn	Methane, propane, Benzene,
	(Pt, Pd, RuO_2)	Toulene, CO_2, NO_2, Methanol, Acetone
Ga_2O_3	SnO_2, Pd, Ta_2O_5, WO_3, NiO	O_2, CO_2, NO, NH_3
In_2O_3	MoO_3, Au, Al, SnO_2	O_3, NO_2, H_2, CO, C_3H_8, H_2S, Cl_2, CO_2, SO_2, NH_3, Ethanol, Acetone
MoO_3	Ti	NH_3, CO_2, NO_2
Nb_2O_5	SnO_2	NH_3, CO_2, C_2H_5OH, H_2
NiO	Li, TiO_x	H_2, HCHO, CH_4, CH_3, COOH, CO, NO_2
Ta_2O_5	-	Humidity
SnO_2	Pt, Ag, Pd, Os, Fe, Au, In, Ru, Bi_2O_3, CeO_2, CuO	CO, CH_4, SO_2, N_2O, CO_2, NO_2, CH_3OH, C_2H_5OH, C_3H_8, H_2, LPG, H_2S, NH_3, C_nH_{2n+2}
TiO_2	La, Pt, Cr_2O_3, WO_3	CH_3OH, C_2H_5OH, C_3H_7OH, O_2, H_2, NH_3, NO_2
WO_3	Mg, Zn, Mo, Re, Au, Pd	NO_2, NH_3, C_2H_5OH, Butylamines, Propanaol, Toulene
ZnO	Al, Sn, Cu, Pd, Fe_2O_3	NH_3, H_2, NO_2, LPG, CH_4, CO, H_2S, CH_3OH, C_2H_5OH, C_3H_7OH

Besides metal oxides, III-nitrides such as GaN [17-19], InN [19], and gallium oxonitride [20] have also shown chemical gas sensing application at higher temperatures for the detection of H_2, O_2, NH_3 etc.

1.1.3 Gas sensing mechanism in semiconductors

A simple model to explain the mechanism of gas sensing (resistance change in a metal-oxide based gas sensors) is that, in air, oxygen adsorbs on the surface (to form oxygen ion), where the electron on the oxygen is extracted from the conduction band of semiconductor. This electron extraction tends to increase the resistance for an n-type semiconductor, such as SnO_2. This model is known as "*Ionosorption model*". At lower temperature of adsorption (150–200 °C) oxygen adsorbs on SnO_2 nondissociately to form molecular oxygen ion (O_2^- $_{(ads)}$) and at higher temperature between 200–400 °C, it dissociates to atomic oxygen ion (O^- $_{(ads)}$) [21-23]. Combustible gas like H_2 reacts with the adsorbed O^-, to form water and electron is send-back to the semiconductor which tends to decrease resistance. These competitive processes are illustrated by the following equations:

$$O_2 \,_{(ads)} + e^- \rightarrow \ O_2^- \,_{(ads)}$$

$$O_2^- \,_{(ads)} + e^- \rightarrow 2\, O^- \,_{(ads)}$$

$$H_2 + O^- \,_{(ads)} \rightarrow H_2O + e^-$$
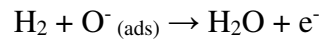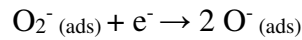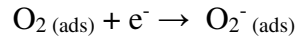
In the case of reducing gases such as CO in the presence of oxygen, the oxidation of CO into CO_2 by reaction with ionosorbed oxygen is responsible for the decrease in electrical resistance by generating delocalized electrons:

$$CO + O^- \,_{(ads)} \rightarrow CO_2 + e^-$$
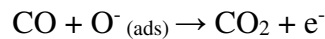
In the absence of oxygen, CO acts as electron doner: it is adsorbed as a CO^+ ion, thus inserting an electron into the conduction band [22], according to following equation:

$$CO \rightarrow CO^+ + e^-$$
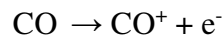
1.1.4 Selectivity problem in semiconducting gas sensors

Metal oxide-based gas sensors generally show high sensitivity but poor selectivity if pure sensor materials are used. Sensitivity is often improved by incorporating noble catalyst particles.

Reproducible performance may be improved by using highly stable materials, which can be operated at quite high temperature, but this cannot solve selectivity problem. Among the well-known gas sensitive materials (SnO_2, ZnO, TiO_2, WO_3, In_2O_3, etc.), SnO_2 is most commonly used and often doped with noble metals such as Pt and Pd to enhance sensing performance. These sensors behave more or less similar to various reducing gases (H_2, CO, etc.) and therefore, this could lead to false alarm and error in the concentrations measured by the detector due to lack of difficulty in separating effects of different gases.

Figure 1.5 shows results obtained with commercial thick film SnO_2 based gas sensors [24]. SnO_2 based sensors show good sensitivity for many reducing gases, resulting in a poor selectivity. One can observe that the effects of the different gases are very difficult to separate. Also, the effect of the presence of humidity in various amounts can significantly affect the sensor signal, causing an uncertainty in interpreting sensor data [25].
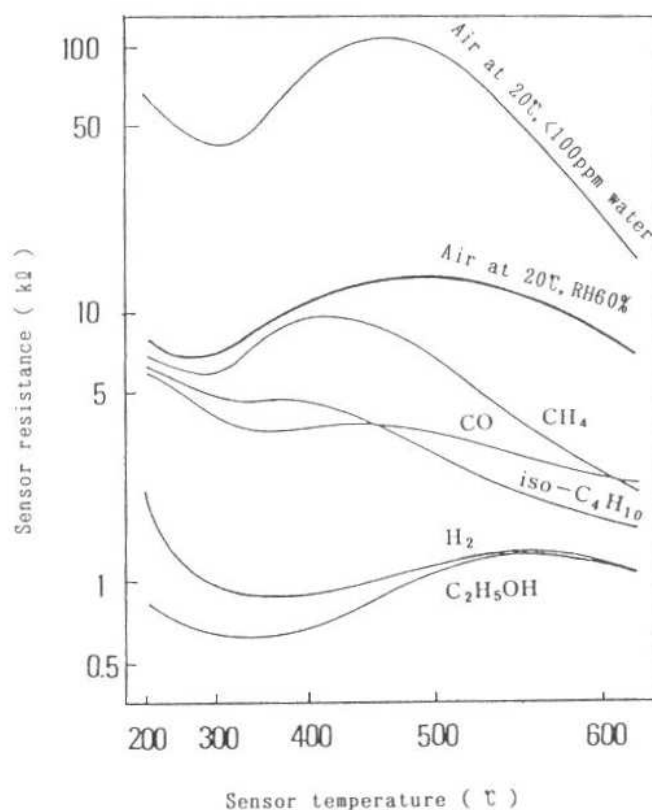
Figure 1.5 SnO_2 sensor response to different gases (1000 ppm) indicates difficulty in separating effects of different gases [24].

1.1.5 Approaches towards selectivity enhancement

Selectivity of semiconductor gas sensors can be enhanced in different ways [26]: (i) by applying catalysts and promoters, (ii) controlling temperatures, (iii) depositing filters (physical or chemical filters).

1.1.5.1 Catalysts and promoters

Catalysts are substances that facilitate chemical reactions without being consumed in the process. When added to a gas sensor, a catalyst can increase the rate of the desired chemical reaction between the target gas and the sensor material. This enhanced reaction rate leads to a faster and more specific response to the target gas. With coating of Pt-HZSM-5 zeolite, a commercial product, onto top of Pd-SnO$_2$ films, the sensors became selective and sensitive to CH$_4$, even with a co-existence of high concentrations of CO and ethanol [27]. Some of the reported catalytic filters are as mentioned in the Table 1.2.

Table 1.2 Selective gas sensing using various catalytic additives and promoters.

Catalyst material	Sensing material	Target gas	Interfering gas	Concertation (ppm)	Reference
Pt, Pd, Ag	SnO$_2$	H$_2$, Co, CH$_4$	air	1000	[28]
V$_2$O$_5$	MoO$_3$	H$_2$	CH$_4$, CO, NO$_2$, NH$_3$, SO$_2$	1000	[29]
Ferrierite zeolite	La$_2$O$_3$ Au/SnO$_2$	H$_2$	CH$_4$, C$_4$H$_{10}$, C$_2$H$_4$, Ethanol	55	[30]
Pt/ZSM-5 zeolite	SrTi$_{0.8}$Fe$_{0.2}$O$_3$	Propane	CO, NO, NO, propene, H$_2$		[31]
Nafion	SnO$_2$	CO	Ethanol	50	[32]

1.1.5.2 Controlling temperatures

Gas sensors often exhibit different sensitivities to various gases at different temperatures. By carefully controlling and adjusting the operating temperature of the sensor, it is possible to enhance the sensor's selectivity for specific gases [33]. Depending on the target gas under study it is found

that there is temperature were the metal oxide gas sensor shows very high sensitivity based on the reaction rate of target gas with sensing surface at a particulate temperature [26]. These temperature ranges are used as selective detection with the temperature control.

1.1.5.3 Applying filters

One of the effective ways of transforming a sensor to a highly selective and sensitive sensor is to apply a filter directly on the sensing layer as shown in the Figure 1.6.
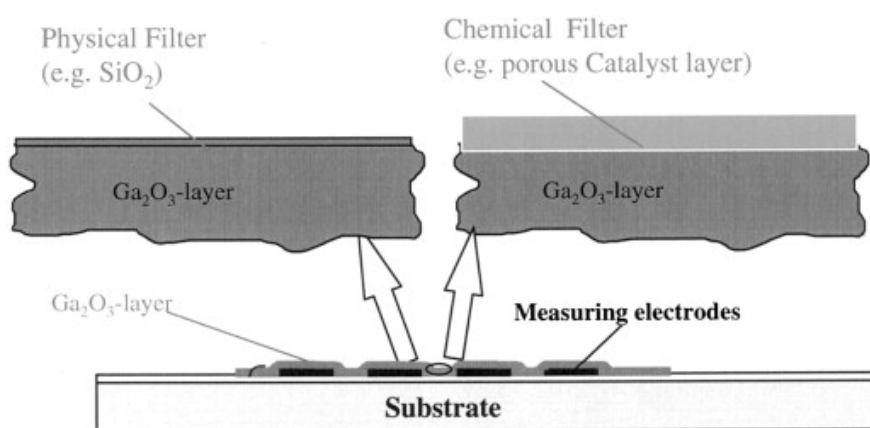
Figure 1.6 The concept of physical and chemical filters [34].

A physical filter with well-defined pore size hinder the interfering gas (bigger molecules) from reaching the sensing layer but allow the gas to be detected to reach sensors surface. Dense [35, 36] or mesoporous [37] SiO_2, zeolites [38] and charcoal [39] are few of the examples. These filters are included as sensor add-ons, e.g., in the housing above the sensor element and there are many commercial sensors that are offered in such form. Chemical filters eliminate interfering gases via a chemical reaction [40] or preferentially transform the target gas into a more active species [41].

1.2 Membranes (filters) for hydrogen separation

A membrane is a physical barrier that lets only specific molecules flow between phases. Membranes may filter microorganisms, separate gases, and cleanse water, as in reverse osmosis. Since 1965, metal membranes have been used for hydrogen purification, and in 1979, Monsanto released the commercially significant gas separation membrane "PRISM," made of polysulfone membrane material [42]. Over the last two decades, significant advancements have been made in the development of gas separation membranes. These membranes can be categorized based on

their composition (whether they are polymeric or inorganic), their structure (whether they are symmetric or asymmetric), and their porosity or density. Membrane gas separation is a promising alternative that offering low energy consumption, continuous operation, lower investment costs, ease of operation and control, mild process conditions, and the potential to combine with other separation technologies [43, 44]. In recent years, significant efforts have been made to develop inorganic H_2-selective membranes due to their high thermal resistance and mechanical strength. The use of membrane separation processes is growing slowly but steadily, with many companies, nations, and organizations viewing clean hydrogen as essential to meeting the Paris Agreement goal of keeping global warming below 2 °C and moving in the direction of 1.5 °C [45]. The development of inorganic H_2-selective membranes is expected to further enhance the efficiency and cost-effectiveness of hydrogen production.

According to membrane pore-size, membranes can be divided into microfiltration (MF), ultrafiltration (UF), nanofiltration (NF) and gas separation membranes. According to the definition of IUPAC in terms of the pore size [46], the MF, UF and NF membranes correspond to macroporous (pore diameter $d_p > 50$ nm), mesoporous (2 nm < d_p < 50 nm) and microporous (0 < d_p < 2 nm) membranes, respectively.

The microporosity analyzed by various semi-empirical methods, such as the HK method of Horvath and Kawazoe [47], the CY method of Cheng and Yang [48] and the S&F method of Saito and Foley [49], exist for estimating pore size distributions (PSDs) in the micropore size range. However, these methods generally underestimate true pore sizes. A more accurate approach is based on the statistical mechanics of adsorption and phase behavior of fluids confined within well-defined pore structures. Density functional theory (DFT) [50] and Monte Carlo (MC) [51] simulation are two widely used approaches for PSD analysis over the complete micropore range. Similarly, the analysis of mesopore size distributions has traditionally relied on the Kelvin equation [52] and with the modified Kelvin equation proposed by Barrett, Joyner, and Halenda (BJH) [53]. Sometimes, Peromporometry method is also applied to determine pore-size of mesoporous materials. In this method, a mixture of non-condensable gas (e.g. He) and condensable vapor (e.g. hydrocarbon) is fed to a porous membrane and the permeation rate of non-condensable gas is measured. For the characterization of macroporous materials (up to 1000 μm pore size) is often done using Mercury Intrusion Porosimetry (MIP) and Bubble Point Test methods [54].

1.2.1 Gas separation mechanisms

Many factors such as feed composition, operating pressure and temperature, membrane pore size, and interactions between molecules passing through the membrane and the membrane's pore surface, all play a part in the processes by which gases are separated by porous membranes. With respect to hydrogen separation, separation can be through one or combination of five separation mechanisms [44]: (i) Knudsen diffusion, (ii) surface diffusion, (iii) capillary condensation, (iv) molecular sieving, and (v) solution diffusion. Separation mechanisms are different for porous membranes and dense (nonporous) ones. Generally, transport and separation mechanisms in porous membranes are Knudsen diffusion, surface diffusion, capillary condensation and molecular sieving, whereas in dense membranes the transport is by solution diffusion. In the following sections, aforementioned five mechanisms are described in detail.
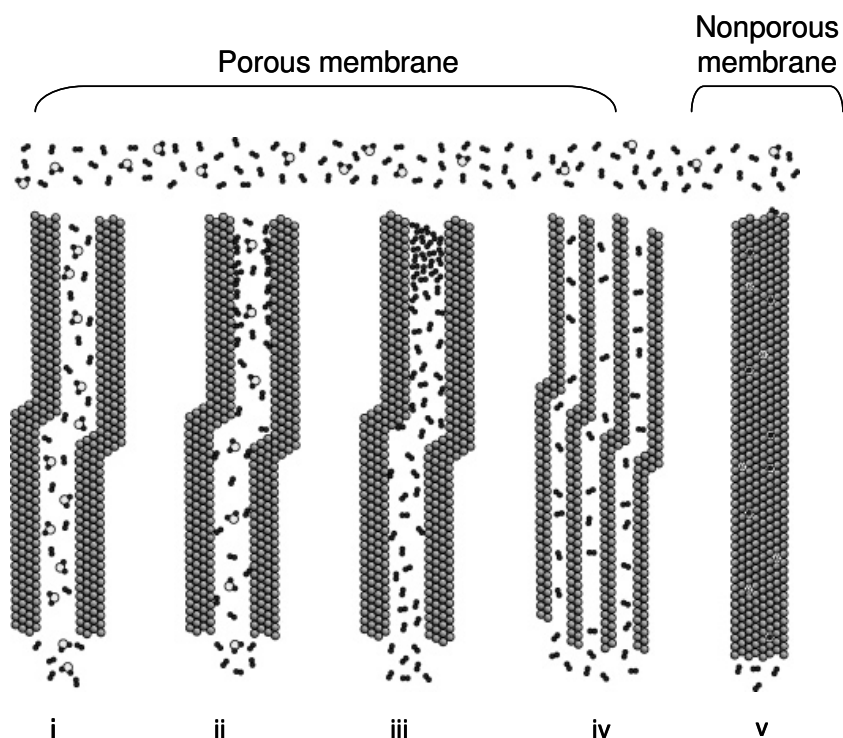
Figure 1.7 Hydrogen separation mechanisms in porous/non-porous membranes (adapted from reference [44]): (i) Knudsen diffusion, (ii) surface diffusion, (iii) capillary condensation, (iv) molecular sieving, and (v) solution diffusion.

1.2.1.1 Knudsen diffusion

Knudsen diffusion takes place when gas molecules have a mean free path much longer than the pore size. In mesoporous materials the mean free path of a gas molecule is larger than the size of the pore. Therefore, the interaction between gas molecule and pore wall is more important than the molecule-molecule interaction. The Knudsen number K_n is a characteristic parameter defined as the ratio of the mean free path of gas molecules [55]. Its value is given by $K_n = \lambda/d_p$, where λ being the average free path of the gas molecules and d_p is the pore diameter. When $\lambda \gg d_p$ the movement of molecules inside the narrow pore channels takes place through collisions of diffusing molecules with the wall rather than with each other. In the regime of Knudsen diffusion the permeance (P_K) is given by following equation [56]:

$$P_K = \frac{\varepsilon d_P}{\tau L} \left(\frac{8}{9\pi MRT} \right)^{\frac{1}{2}}, \tag{1.1}$$

where ε is the porosity of the membrane, d_P is the pore diameter, τ is the tortuosity, L mean membrane thickness, R is the gas constant, T is the temperature, and M is the molecular weight of the diffusing gas.

As the driving force for transport is the partial pressure of the gas species, Knudsen transport can occur either by concentration gradient or by pressure gradients. The permeation rate of each component is inversely proportional to the square root of its molecular weight. Gas permeance selectivity is calculated as the ratio of square root of the molar masses of gases involved (based on equation 1.2). For example, the selectivity of H_2 with respect to CO_2 by Knudsen diffusion will be 4.7. Hence, separation by Knudsen diffusion has a limited selectivity and it depends on the molecular masses of gases and is therefore only for applied for the separation of light gases from heavier ones.

1.2.1.2 Surface Diffusion

Gas molecules may move freely over a surface, adsorb on specific locations there, and interact with the surface itself. As part of the surface diffusion processes, the diffusing species first adsorb on the pore walls before being easily transported over the surface in the direction of decreasing surface concentration. The membrane surface preferentially adsorbs molecules with a higher molecular weight, polarity, and polarizability [57]. The transport of non-selectively adsorbed

molecules through the pore may also be significantly reduced or eliminated by the adsorbed species on the membrane pores. When the pore size is between 2 and 3 molecular diameters of the adsorbed species, a hindrance effect is introduced that causes non-adsorptive separation selectivity for the adsorbed species. Conditions like as temperature, pressure, and surface type affect the adsorption efficiency. Even at mild temperatures, the surface diffusion effect is noticeable. Adsorption weakens with increasing temperature, therefore surface diffusion slows down as well. To use surface diffusion as a separation method, the pores must be very tiny (pore radius 3 nm) and the temperature must be maintained low (300 °C) owing to the required physical adsorption of the gas [58].

1.2.1.3 Capillary condensation

At temperature below the critical temperature point of the diffusing gas, in porous system the increase of pressure first leads to multilayer adsorption until all pores are filled with liquid. This phenomenon is known as capillary condensation [59]. In the capillary condensation process, vapor condensation occurs below the saturation vapor pressure, P_{sat}, of the pure liquid. When the pores are completely filled with condensed phase, then only the species soluble in the condensed phased can permeate through the membrane, therefore, fluxes and selectivities are generally high for capillary condensation. Although this separation mechanism appears to be effective, it is limited by the need for a condensable component. This limits its applicability range due to the temperature and pressure range needed for capillary condensation.

1.2.1.4 Molecular sieving and activated diffusion

Molecular sieving is a technique for separating molecules that works when the pore diameters of membranes are very narrow (< 2 nm). As the pore size decreases to a certain point, only molecules of a certain size are able to pass through the membrane. Molecular sieving may be used to provide high selectivity and permeability for the smaller gas molecules in a mixture, but it requires extremely fine-tuning of the membrane pore sizes to achieve the appropriate separation efficiency [60]. One of the most important characteristics of microporous membranes which results in very high separation factors is the "activated gas transport"; microporous materials have a permeance (P_{MS}) that rises as a function of temperature [61] as shown in the equation 1.2.

$$P_{MS} = P_o \exp\left(-\frac{E_a}{RT}\right),$$ (1.2)

where P_o is pre-exponential factor, E_a is activation energy, R is gas constant, and T is temperature.

1.2.1.5 Solution diffusion

In dense membranes, normally pores are not available for gas diffusion using the above mentioned mechanisms. The most common model to describe gas transport through dense membranes is solution diffusion mechanism. Gases are soluble in the dense membrane to a certain extent. Separation of gases occurs due to difference in solubility and diffusivity of gases in the membrane, separation occur [62]. A gas molecule is firstly adsorbed on one side of the membrane, dissolves in membrane, diffuses through the membrane and desorbs on the other side of the membrane. When diffusion through the membrane takes place in the form of ions and electron or as atoms, the molecules first split up after adsorption and recombine after diffusing through the membrane. Separation through polymeric membranes is based on this mechanism as well as in dense inorganic membranes. Although selectivity by solution diffusion mechanism is quite high, but the flux is quite low, in comparison that is observed in porous membranes.

1.2.2 Materials

Gas selective membranes can be broadly categorized into four types: polymeric (organic), metallic, carbon and ceramic (the latter three are named as inorganic). Much work has been done in the development of polymeric membranes compared to inorganic membranes due to relatively lower cost of the polymer. Interest in the field of inorganic membranes development has grown rapidly in the last two decade due to their ability to be operated under higher temperature than polymeric membranes and relatively higher chemical stability.

1.2.2.1 Metallic Membranes

Metallic materials are of great interest for hydrogen-selective membranes. The fundamental mechanism governing the performance of dense metallic membrane is quite different from porous membranes. In a dense metallic membranes, H_2 permeates through the solid material via the solution diffusion mechanism that involves a total of seven steps [44]: (i) arrival of a mixture of H_2 and undesired gas stream to the feed end of the membrane; (ii) dissociation of chemisorbed H_2 into H^+ ions and electrons (e^{-1}); (iii) adsorption of H^+ ions into the membrane bulk; (iv) diffusion of H^+ ions and electrons through the membrane; (v) desorption of H^+ ions and the electrons into discrete molecules of H_2; (vi) reassociation of the H^+ ions and the electrons into H_2 molecules; and

(vii) diffusion of the H_2 from the permeate-end of the membrane. The diffusive flux of hydrogen through a bulk metal membrane of thickness L is generally described by Sievert's law [63][63]:

$$J = \frac{-k(\sqrt{P_f} - \sqrt{P_p})}{L}, \qquad (1.3)$$

where J is diffusive flux ($molm^{-2}s^{-1}$), k is the hydrogen permeability of the metal ($molm^{-1}s^{-1}Pa^{-0.5}$), L is the membrane thickness (m), P_f and P_p are the hydrogen partial pressures (Pa) on the feed side and permeate side of the membrane surface. The square-root proportionality of hydrogen flux with respect to the partial pressure driving force is indicative of the bulk phase diffusion as the rate-limiting step [64]. As hydrogen is transported through a unique dissociated atomic form through the metal, the metal membranes are 99.9% selective to hydrogen and allow the permeation of undesired gas species through pin-holes and defects in the metal membrane.

High-purity hydrogen could be available through dense metallic membranes especially through Pd and its alloys. Hydrogen selectivity is typically very high in these systems, since dense structure prevents the passage of large atoms and molecules such as CO, CO_2, O_2, N_2, etc. This high selectivity translates to very high purity hydrogen and the increased thermal stabilities allow higher operating temperatures. The metals which are most suitable for H_2 separation membranes typically have high H_2 permeabilities [65], high diffusivities or solubilities [66], and good thermal stability elevated temperatures [67]. Metallic membranes for hydrogen separation could be of many types, such as (i) pure metals: Pd, V, Ta, Nb, and Ti; (ii) binary alloys of Pd: Pd-Cu, Pd-Ag, Pd-Y etc.; (iii) complex alloys: Pd alloyed with more that two other metals; (iv) amorphous alloys: typically Group IV and Group V metals; and (v) coated metals: Pd over Ta, V, etc. The permeability of H_2 through these types of membranes is a function of the lattice structure and various types of lattice defects (vacancies, dislocation) and reactivity towards H_2. Body centered cubic (BCC) metals such as Fe, V, Nb, and Ta exhibit high H_2 permeabilities [65, 66] than face centered cubic (FCC) metals such as Pd and Ni [68]. Pd possessing significantly higher H_2 permeability than Ni. H_2 permeability decreases with increasing temperature in the case of Nb, V, and Ta. This is due to the decrease of hydrogen solubility more rapidly that the increase of the diffusion coefficient. Although Nb, V, and Ta have higher permeabilities (10–15 times greater than Pd), these metals form oxide layers and are difficult to use as hydrogen separation membranes [68].

Historically, H_2 separations were performed with Pd-based membranes, since they naturally catalyzed the surface dissociation/reassociation processes and are highly permeable to hydrogen. Extensive research works have been done in the field of Pd-based membranes [69-75]. Pd is the most widely researched material since it is highly permeable to the H_2, resistant to ambient conditions of air, oxygen and moisture, and is able to rapidly dissociate H_2 molecules into atoms on the surface. Pd alloy membrane can be used to produce H_2 for practical purposes with a purity of up to 99.99%. Earlier in United States and former Soviet Union, relatively thick-walled tubes of Pd were employed. The nearly perfect hydrogen permselectivity of thicker Pd membranes enables them to provide very high purity H_2 for use in semiconductor manufacturing industry. But monolithic Pd foils and tubes are very costly and hence prohibitive for most purposes. There, to produce economic means of H_2 separation on industrial scale, a thin layer of about < 20 µm, adherent and durable Pd film must be applied to a hydrogen-permeable support [76]. Kikuchi and Uemiya have done an extensive work on Pd composites that uses porous membranes as supports [77-80]. Over the last decade, composite Pd membranes coupled with high permselectivity and reasonable H_2 fluxes have been fabricated using a range of deposition methods and supports. Composite membranes consist of a thin layer of Pd on H_2 permeable support so that Pd films with micron thicknesses or less are attainable. Very high H_2 permselectivity is possible if a defect-free Pd can be deposited onto the membrane support. In addition, the membrane can be operated at high transmembrane pressure differentials because the substrate provides mechanical supports for the thin Pd film.

A major limitation of Pd membrane is the high cost of this metal and difficulty of fabricating defect free membranes with films of the order of micron or less. There are several other problems that impede the use of Pd membrane technology. Additionally, Pd may undergo a phase transition ($\alpha \rightarrow \beta$) in the presence of H_2 at temperature below 300 °C [81, 82]. This leads to an increase in lattice size as it absorbs H_2, leading to wraping and embrittlement. To avoid metal embrittlement and resulting membrane cracking or distortion, pure Pd should not be exposed to H_2 at temperatures below 300 °C. Pd is also susceptible to contamination/poisoning by common industrial constituents such as hydrogen sulfide, chlorine, carbon monoxide, and hydrocarbons. Long-term stability at high temperature, above 450 °C, has been a problem, mainly deactivation by carbon under reaction conditions in a membrane reactor [83-85]. To increase resistance to

embrittlement, Pd is alloyed with other metals such as Ag and Cu. In addition to providing thermal stability, alloying Pd with other metals also increases its resistance to chemical contaminants. Pd-Ag alloy is found to maximize the hydrogen permeability. Alloying of Pd with Cu has been reported to offer significant tolerance to the presence of hydrogen sulfide in the hydrogen gas stream [86, 87]. Several other alloying elements, such as Au, Y, and Ce have been identified with significant increase in hydrogen permeability [88]. Ternary alloy compositions (Pd-Cu-transition metal) are also being investigated for maximizing membrane permeability and stability.

For Pd membranes to be economically attractive in H_2 separations one must try to increase their flux by a factor of 2–4. Hence, research is focused on the preparation of thin metallic films. Thin membrane would reduce the cost as well as increase the H_2 flux. Thin Pd membranes are deposited on porous supports. Two supports were widely used, such as porous Vycor (silica glass), and porous alpha-alumina [68]. These supports are used because of their smooth surface. However, fitting ceramics to metals gives the mechanical stability. Therefore, stainless steel could be used as a support material because of its mechanical stability, its thermal expansion coefficient close to that of Pd, and its ease of sealing. Generally there are three methods for coating thin metallic films onto supports: electroless-plating, chemical vapour deposition (CVD), and physical sputtering [89]. Under controlled conditions all these methods produce good quality membranes with high hydrogen selectivity. Table 1.3 presents some of the selected metallic membranes, substrate used for coatings, and their hydrogen permeance and selectivity.

Table 1.3 Selected hydrogen separation metallic membranes.

Method (material)	Support	H_2 Permeance $(10^{-6}\ molm^{-2}s^{-1}Pa^{-1})$	Selectivity
CVD (Pd)	γ-Al_2O_3	0.1–0.2 at 773 K [90]	200–300 (H_2/He)
electroless (Pd)	TiO_2	6.3 at 773 K [91]	1140 (H_2/N_2)
electroless (Pd)	stainless steel	0.22 at 623 K [92]	110 (H_2/N_2)
electroless (Pd-Cu)	γ-Al_2O_3/ZrO_2	0.023 at 723 K [86]	1150 (H_2/N_2)
electrodeposition (Pd-Cu)	Ni-porous stainless steel	8.4 at 723K [93]	3000 (H_2/N_2)

electrodeposition (Pd-Ni)	stainless steel	6.7 at 723 K [94]	10000 (H_2/N_2)
electrodeposition (Pd-Ag)	silicon wafer	45 at 723 K [95]	4000 (H_2/N_2)

1.2.2.2 Polymer

In the past few decades, a considerable amount of attention has been paid to polymeric membranes for gas separation applications. Polymer membranes are used industrially for hydrogen separation from gaseous mixtures consisting of N_2, CO, or hydrocarbons. Polymeric membranes such as UOP Polysep membrane systems and Monsanto PRISM membrane systems are used to recover hydrogen from refinery, petrochemical, and chemical process streams [96].

Polymeric membranes are generally used generally in lower-temperature hydrogen-recovery where the operating temperatures are limited to 90–100 °C [97]. These membranes are cost effective, easier to process, and more mechanically tunable than inorganic membranes. Good ability to sustain high pressure drops and lower costs are key advantages of polymer membranes. However, limited mechanical strength, relatively high sensitivity to swelling and compaction, and susceptibility to chemicals such as HCl, SO_x, and CO_2 make them less attractive.

Polymer membranes are dense type and are further divided into glassy (prepared at temperature below the glass transition temperature) and rubbery (prepared at temperature below the glass transition temperature) polymeric membranes. Glassy membranes have higher selectivity and lower flux, whereas rubbery membranes have higher flux but lower selectivity [97]. Glassy polymers are dominated by diffusivity selectivity and are often employed to remove lighter gases such as H_2, whereas rubbery polymers are dominated by solubility selectivity and are used to remove gases like CO_2. Polymer membrane used for gas separation processes generally follow solution-diffusion mechanism. Some of the polymers which have been tested with respect to hydrogen permeation are polysulfone, polystyrene, polymethyl methacrylate, polyvinylidene fluoride [98]. Polysterene shows the best combination of H_2 gas permeability and selectivities over N_2, CH_4, and CO_2 [99], with H_2/N_2 and H_2/CO_2 selectivity of about 39.7 and 2.3, respectively.

As known that metal and alloys membranes are sensitive to gases such as CO or H_2S, ceramic membranes which are inert to these poisonous gases would be of better choice for H_2 purification. In microporous ceramic membranes, the flux is directly proportional to the pressure, where as in

Pd membranes, it is proportional to the square root of the pressure. Hence, microporous ceramic membranes become more attractive options when systems are operated at higher pressures. Also, in microporous inorganic membranes permeance increase with temperatures. Therefore, microporous ceramic membranes can be operated at higher pressures and temperatues. In the following sections zeolite and polymer-derived ceramics based membranes are described.

1.2.2.3 Zeolite

Zeolites are crystalline aluminosilicates materials that have uniform, molecular-sized pores. Zeolite structure is made up of TO_2 units, where T is a tetrahedral framework atom (Si, Al, B, Ge, etc.) [44]. Since the development of first zeolite membrane in 1987 [100], significant progress has been made to improve membrane quality. Today more than 14 zeolite structures, including MFI, LTA, MOR, DDR, and FAU have been employed as hydrogen separation membranes. Among various types of zeolite membranes available, the 10-membrane ring MFI structure (silicalite-1 and ZSM-5) is the most extensively studied for gas separation. MFI membranes with high Si/Al ratios possess outstanding thermal and chemical stabilities. Highly siliceous DDR-type zeolite consists of cages connected by narrow elliptical windows of 8-member ring openings [101]. Molecular transport through DDR-type zeolite is mainly controlled by the narrow windows which have dimensions of 3.6×4.4 Å^2 [101]. The DDR zeolite has excellent thermal stability allowing high temperature operations in moist atmosphere.

Zeolite materials are commonly prepared by precipitation under hydrothermal conditions in the presence of a template that dictate the zeolite structure during crystal growth. Generally tetrapropyl ammonium hydroxide (TPAOH) is used as a common template, which is burned off after zeolite crystal growth. In the secondary growth (template-free method), a zeolite seed layer is dip-coated on the support followed by the growth of seeds into continuous zeolite layer [102].

Mechanism of gas permeation through the MFI-type zeolite membrane depends on the gas adsorption properties on the zeolite. Nonadsorbing gas molecules may directly enter the zeolite pores. Permeation of strongly adsorbing gases through MFI membrane is controlled by either adsorption or activated diffusion, or both. In MFI zeolites, H_2 selectivities over other gases were observed to be rather moderate at higher temperatures because gas transport through the 5.6 Å diameter MFI channels is governed by Knudsen-type diffusion. Dong et al. obtained a H_2/CH_4 selectivity of 2 with H_2 permeance of about 10^{-7} mol m^{-2} s^{-1} Pa^{-1} [103]. All the MFI type membranes

exhibited ideal H_2/CO_2 selectivities below the theoretical Knudsen diffusion selectivity ~ 4.69. This low H_2 selectivity was attributed to the existence of nonselective membrane defects, such as, pinholes and sealing leakage as well as possible chemical interactions between the molecules and the chemical impurities in the zeolites structure. DRR-type zeolite membranes having an effective pore-size of 4 Å was expected to offer high H_2 selectivities over gases such as CO_2, CO, CH_4, etc. The DDR zeolite membranes achieved H_2/CO_2 ideal selectivity slightly greater than the Knudsen factor at 500 °C, but the selectivity was far lower than that was expected [104]. Also, the H_2 permeance was lower than that in the MFI membranes by an order of magnitude because of relatively large membrane thickness (~ 10 µm). Low H_2 selectivity in DDR membranes has been attributed to the presence of intercrystalline path in the membranes [101], as shown in Figure 1.8.
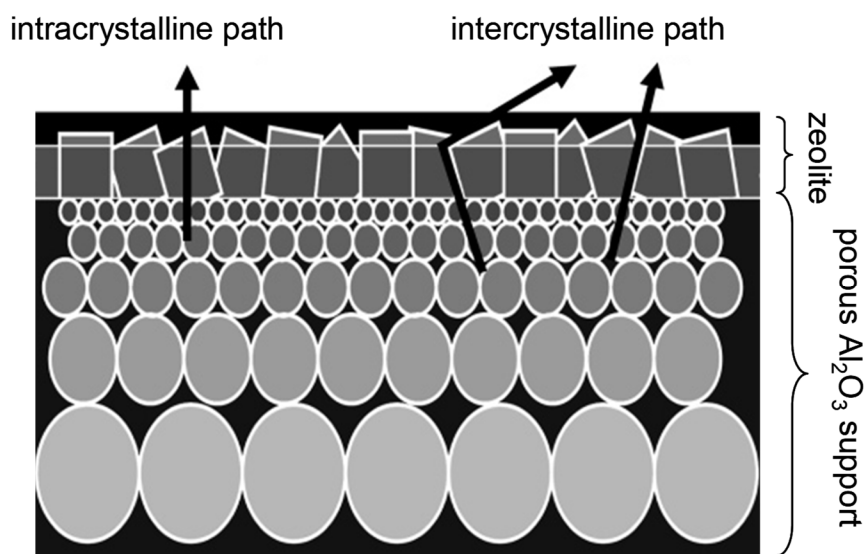
Figure 1.8 A general representation of a zeolite membrane deposited on a porous Al_2O_3 support, showing possible gas permeation pathways either through interzeolite crystals or intrazeolite crystals (adapted from reference [44]).

To improve the performace of zeolite membranes, surface modification techniques have been employed by different research groups. To enhance the H_2 selectivity, MFI membranes must be modified to reduce the intercrystalline pore size as well as to minimize the non-selective intercrystalline pores. In case of DDR-type membranes, improvements are needed to eliminate the intercrystalline pores and to significantly reduce membrane thickness to enhance H_2 permeance.

Masuda et al. [105][105] modified zeolite membranes by catalytic cracking of silanes molecules (methyldiethoxysilane) preadsorbed at the active sites. After calcination, mono-SiO_2 units formed in the zeolite channels that reduced the effective MFI pore-size. H_2 separation factor for H_2/N_2 mixture was increased by more than 50 times at 110 °C but the H_2 permeance was reduced by an order of magnitude from 2.8×10^{-7} to 2×10^{-7} mol m^{-2} s^{-1} Pa^{-1}. Zheng et al. [106] used the counterdiffusion CVD technique to modify the intercrystalline pore in an in situ made DDR zeolite membrane (thickness ~ 10 µm). They used TEOS as silica precursor. H_2/CO_2 permeselectivity of the membrane was increased from 2.6 to 32.7 after modification. However, H_2 permeance was decreased of magnitude from about 10^{-6} to 10^{-8} mol m^{-2} s^{-1} Pa^{-1}. Enhancement in H_2/CO_2 selectivity for the modified DDR membrane was attributed to the reduction in intercrystalline pore.

One of the main hurdles to the industrial applications of zeolite membranes is the high cost associated with the time-consuming, energy intensive membranes preparation processes. Another challenge in zeolite membrane development is the minimization of intercrystal pores formed in polycrystalline zeolite films. The existence of intercrystal pores with sizes large than the zeolitic pores is the major cause for decline in molecular separation efficiency. Presently the zeolite membrane development is at a laboratory scale. For commercial applications, greater H_2 flux and selectivity needs to be demonstrated.

1.2.2.4 Polymer-derived ceramic (PDC)

Since the last few decades ceramics derived from preceramic polymers have attracted great attention due to their advantages over traditional ceramic processing methods. Traditional method to prepare SiC and Si_3N_4 ceramics, powder technology, requires sintering additives and very high temperature (1700–2000 °C) [107, 108]. Polymer-derived ceramics (PDCs) offer an easier route to synthesize ceramic fibers, thin layer or composites materials which in principle cannot be produced using powder technology [109]. Relatively low temperature (1000–1300 °C) to produce Si-based ceramics is of economical interest. PDCs exhibit exceptional properties, such as, thermal, chemical and oxidation stability up to 1500 °C and above [110].

The first synthesis of non-oxide ceramic 'SiC' was reported by Fritz in 1956 [111] and and later by Yajima in 1975 [112]. However, the production of these ceramics starting from polymeric precursors was reported for the first time in the early 1960s. Later the first practical application — manufacturing of small-diameter Si_3N_4/SiC fibers for high-temperature applications — from

polyorganosilicon compounds (polysilazanes, polysiloxanes, and polycarbosilanes) to ceramic was reported by Verbeek and colleagues [113, 114]. Different classes of preceramic precursors (polysilazane, polycarbosilane, polycarbosiloxanes, polysiloxanes, etc.) which are generally used for the synthesis of PDCs are illustrated in Figure 1..
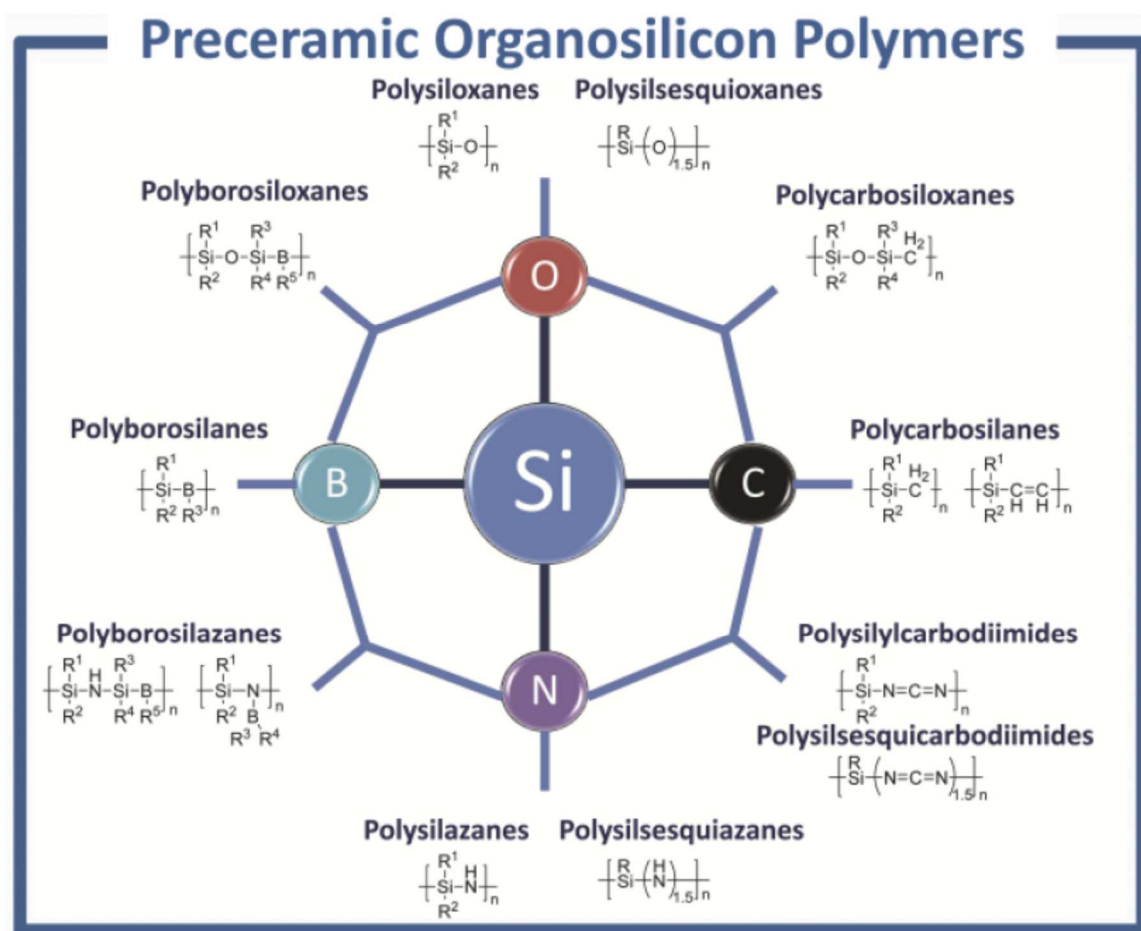
Figure 1.9 Classification of Si-based pre-ceramic polymers [115]: polysilazanes, polyborosilazanes, polyborosilanes, polyborosiloxanes, polysiloxanes, polycarbosiloxanes, polysilylcarbodiimides, etc.

These polymers are characterized by an inorganic backbone and organic substituents. The backbone provides thermal resistance and the substituents can possess the ability to modify properties, such as, solubility, hydrophobicity/hydrophilicity. These substituents also affect the

cross-linking ability between polymeric chains. The molecular structure of preceramic polymer influences — the composition, number of phases and phase distribution, microstructure of the final ceramic materials.

Formation of PDCs consists of mainly three main steps [116]: (i) synthesis of preceramic polymer; (ii) cross-linking of polymer at moderated temperature to get organic/inorganic network; (iii) ceramization process of the cross-linked polymer – polymers are converted to inorganic amorphous/crystalline materials depending of the pyrolysis temperature between 800 °C to 1800 °C. One of the main advantages of using PDCs route is — control over the final composition of ceramic using different preceramic polymeric precursors, cross-linking and pyrolysis conditions.

Chlorosilanes R_xSiCl_{4-x} (x=0, 1, 2, 3) are the most common used starting material used for the synthesis of above shown different preceramic organosilicon polymers (Figure 1.10). The monomer used in the synthesis of organosilicon polymers contain active sites such as Si-H, Si-Cl, Si-C=C, which allows polymerization by means of elimination, substitution or addition reactions. These polymers are generally produced in large scale by the Müller-Rochow process — involving the reaction of gaseous methyl chloride with silicon, containing copper as catalyst in a fluidized-bed reactor at 250-300 °C. Different syntheses routes of organochlorosilicon polymers are shown in Figure 1.10.
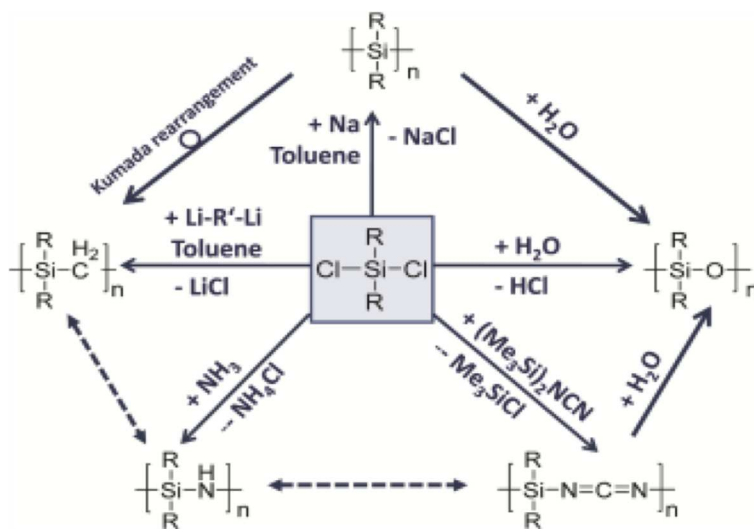
Figure 1.10. Synthesis routes of most representative classes of Si-based preceramic polymers from organochlorosilanes [116].

As already mentioned above, the second step in the processing of PDCs is cross-linking process. During this step polymeric precursors are converted into organic/inorganic materials at low temperatures (150–300 °C). This transformation prevents the loss of low molecular weights of components (monomers) of the precursors, and thus increases the ceramic yield. Various reactions occurring during cross-linking of polysilazane is illustrated in Figure 1.11.
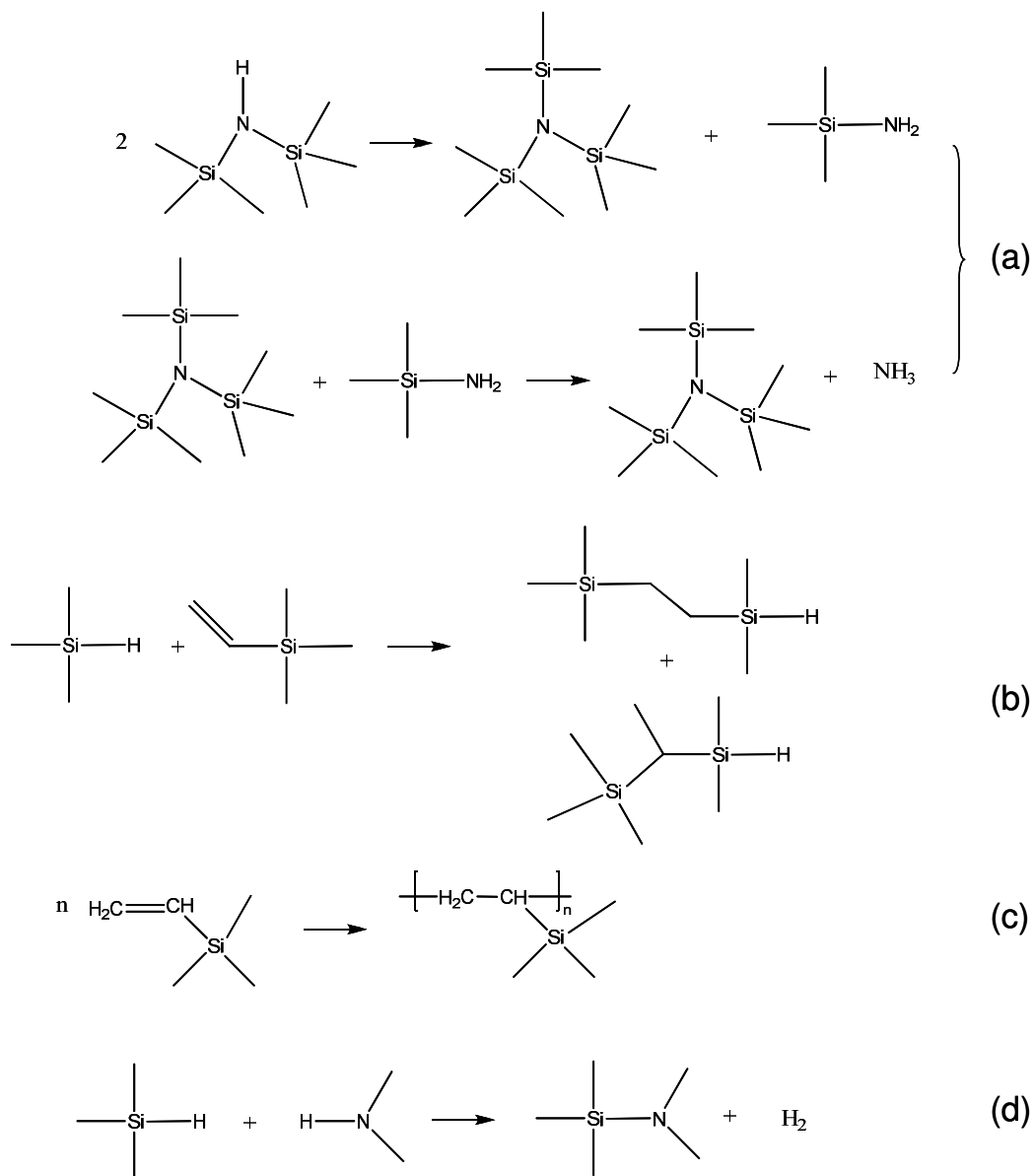
Figure 1.11 Cross-linking reactions of polysilazanes: (a) transamination, (b) hydrosilylation, (c) vinyl polymerization, (d) dehydrocoupling (adapted from reference [116]).

Cross-linking of polysilazanes occurs via four major reactions: transamination, dehydrocoupling, vinyl polymerization and hydrosilylation. *Hydrosilylation* reaction occurs for the precursors which contain Si-H and vinyl groups, which leads to formation of Si-C-Si and Si-C-C-Si bonds. This is a fast reaction which can even occur starting from 100-120 °C. Higher ceramic yield as well as higher carbon can be achieved in the final ceramic due to hydrosilylation reaction [117]. *Dehydrocoupling* of Si-H/N-H or Si-H/Si-H lead to Si-N and Si-Si bond formation and hydrogen evolution. This reaction generally starts at 300 °C. *Vinyl polymerization* occurs at higher temperatures with no mass loss. *Transamination* reactions (200–400 °C) are associated with the evolution of amines, ammonia etc. and hence mass loss occurs. This reaction leads to decrease in nitrogen content.

During the last step, polymer-to-ceramic conversion, thermal decomposition of basic organosilicon polymer occurs — ceramization process [116]. The ceramization process of cross-linked precursors involves thermolysis and volatilization of their organic groups in the temperature range of 600–1000 °C, which finally transforms into amorphous ceramics. Investigation of volatile species and fragments of the decomposition products during organic/inorganic transformation is monitored by simultaneous thermal analysis coupled by mass (TGA) and FTIR spectrometery. During ceramic formation evolution of gases, such as, CH_4, NH_3, H_2, etc., leads to generation of pores in the ceramic. This process of pore generation is used for the development of microporous ceramic membrane by depositing polymeric precursor on porous support followed by pyrolysis process. Thermal decomposition behavior of different organosilicon polymers is illustrated in Figure 1.12 After thermal treatment above 800 °C different preceramic polymers like polycarbosilane, polysiloxane and polysilazanes/polysilylcarbodiimides are transformed to amorphous SiC, $Si_xC_yO_z$ and $Si_xC_yN_z$ ceramics, respectively.
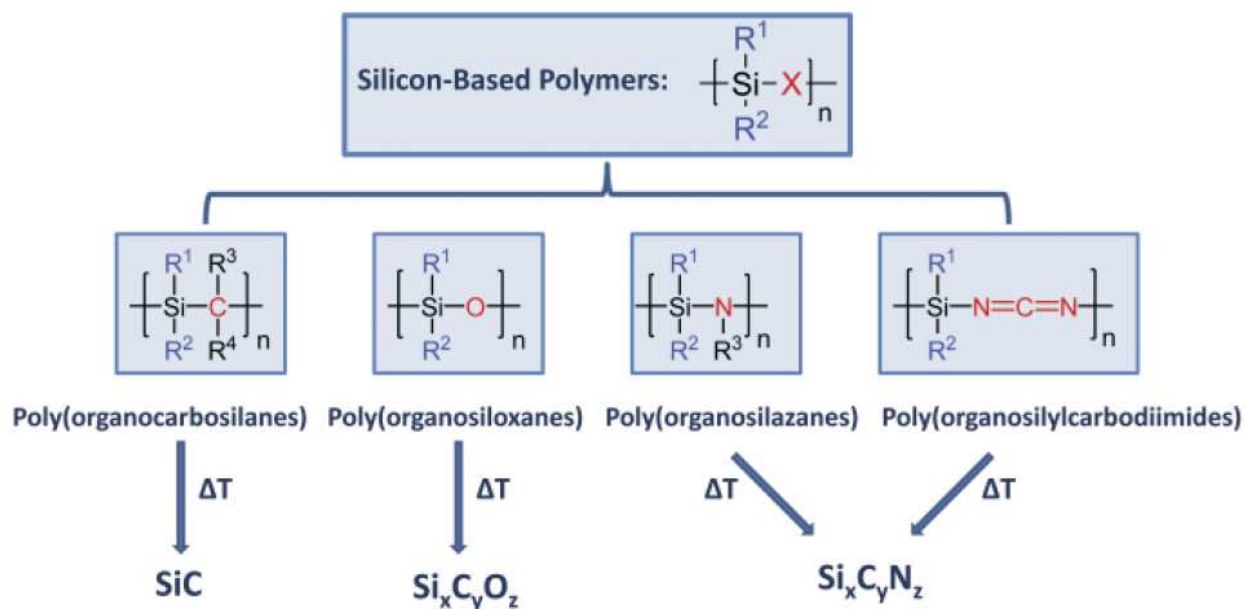
Figure 1.12 Thermal decomposition of silicon-based polymers [115]. Polymer-derived silicon carbide (SiC), silicon oxycarbide ($Si_xC_yO_z$) and silicon carbonitride ($Si_xC_yN_z$) ceramics are obtained after the thermal treatment of polycarbosilane, polysiloxane and polysilazanes/polysilylcarbodiimides, respectively, at $T \geq 700$ °C under inert atmosphere (Ar or N_2).

The detection of H_2 and CO in oxygen-free conditions is crucial for various applications, including online control of hydrogen fuel cell performance [118]. Most hydrogen is produced through steam reforming of methane, which leaves small concentrations of CO in the fuel stream [119]. CO is an effective poison for Pt-based catalysts, causing substantial degradation in fuel cell performance. Therefore, if hydrogen from steam reforming is used as fuel in fuel-cells, the residual CO concentration should be precisely controlled. Previous works on filter/sensor integration have not focused on small molecules like H_2 and CO, nor studied amorphous ceramic materials or applied filter/sensor combination in oxygen-free conditions. Therefore, the present thesis works aims to investigate the suitability of polymer-derived ceramics for gas separation filters integrated with chemiresistors. Polymer-derived ceramics due to their thermochemical stability and tunable porosity could be a prospective filter material for application in enhancing gas selectivity under harsh reducing conditions.

Chapter 2. Experimental procedures

This chapter presents the experimental methods and equipment used for the synthesis and characterization in this work. Pyrolysis conditions applied to obtain ceramics from polymeric precursors, structure of gas sensor substrate, deposition methods of sensing materials on sensors substrate and coating process to deposit polymer-derived filter layer on sensor substrate is described in this chapter. Also, various characterization equipment and applied parameters to characterize the structure of synthesized samples are briefly discussed at the end.

2.1 Pyrolysis parameters to obtain polymer-derived ceramics

In this work pyrolysis (a heat treatment process in inert environment to cross-link and decompose precursors at high temperatures) of three pre-ceramic polymers were done to obtain ceramics for structural characterization. The temperature of pyrolysis was calculated based on thermal analysis data described in sections 4.1.3, 4.2.3 and 4.3.3 of chapter 4. The applied parameters of heat treatments are mentioned below:

SiOC ceramic derived from polysiloxane: To prepare the SiOC ceramic powder commercial vinyl-functionalized polysiloxane precursor (XP RV200, Evonik Hanse GmbH) was taken and pyrolyzed at various temperatures (700 °C, 800 °C and 900 °C). The polymer was kept in a quartz boat under glove-box and transferred to a high temperature furnace. The polymer was heated from room temperature to 200 °C at a heating rate of 100 °C h^{-1}, hold for 1 h at 200 °C to facilitate cross-linking and further heated to the required temperatures (T_R) with a heating rate of 100 °C h^{-1}, hold for 1 h at T_R and then cooled to room temperature [120].

SiCN ceramic derived from polysilazane: SiCN ceramic power was synthesized by pyrolyzing commercially available polysilazane (Durazane 1800, Merck) at various temperatures (700 °C, 800 °C and 900 °C). The polymer was kept in a quartz boat under glove-box and transferred to a high temperature furnace. The polymer was heated from room temperature to 250 °C at a heating rate of 100 °C h^{-1}, hold for 1 h at 250 °C to facilitate cross-linking and further heated to the required temperatures (T_R) with a heating rate of 100 °C h^{-1}, hold for 1 h at T_R and then cooled to room temperature.

SiC ceramic derived from polycarbosilane: To prepare SiC ceramic powder commercial allyl-hydrido polycarbosilane precursor (SMP10, Starfire Systems) was taken and pyrolyzed at various temperatures (700 °C, 800 °C and 900 °C). The polymer was kept in a quartz boat under glove-box and transferred to a high temperature furnace. The polymer was heated from room temperature to 200 °C at a heating rate of 100 °C h^{-1}, hold for 1 h at 200 °C to facilitate cross-linking and further heated to the required temperatures (T_R) with a heating rate of 100 °C h^{-1}, hold for 1 h at T_R and then cooled to room temperature.

2.2 Gas sensor substrate
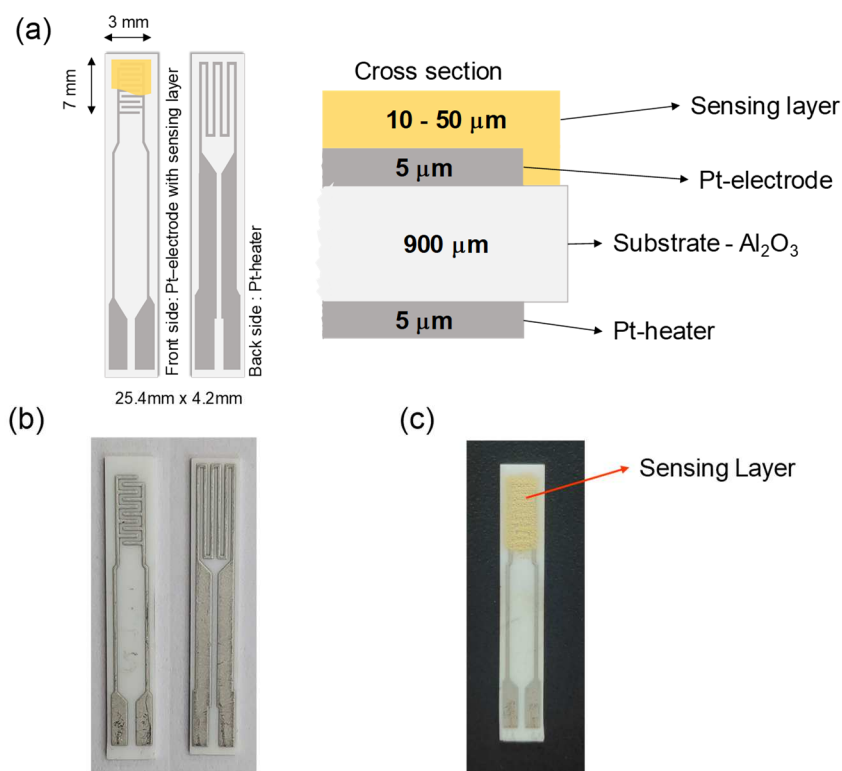
Figure 2.1 Gas sensor substrates: (a) schematic layout of planar alumina substrate with Pt-electrode and Pt-heater, (b) actual photo of sensor substrate, (c) screen-printed GaN sensing layer on the front side of sensor substrate.

Figure 2.1 shows schematic design of sensor substrate used for coating of sensing materials. It consists of planar Al_2O_3 substrate with Pt-electrodes on the front side for measuring resistance and a Pt-heater on the backside to heat the sensor at the required temperature of sensing measurement. The interdigited structure of electrodes allow measuring resistance even if a small area is coated

with sensing material. Before using sensor substrate, it was cleaned with acetone and then dried in a hot air oven for 4 h at 120 ℃ to remove any contaminants and moisture.

2.3 Deposition of sensing layer on sensor substrate

Gas sensing materials were deposited on sensor substrates using two methods to study the effect of sensing layer thickness on sensing behavior.

2.3.1 Radio frequency (RF) sputtering

In order to deposit thin film of SnO_2 of various thickness on sensing substrates, radio frequency (RF) sputtering method was used. Schematic of the set-up is shown in Figure 2.2. The radio frequency (RF) sputtering equipment is consisting of a vacuum chamber to ensure a clean, contaminant-free environment during the process. Inside the vacuum chamber, there is a substrate holder or stage where the target material is to be deposited. The target holder is typically made of a conductive material at which target material is attached. RF sputtering process utilizes radio frequency (RF) power to create a plasma within the vacuum chamber. This field ionizes the sputtered gas (argon) present in the chamber. The positive ions bombard the target surface with high energy, dislodging atoms or molecules from the target material through a process known as sputtering. These ejected particles then travel through the chamber and deposit onto the substrate, forming a thin film. The sputtering process parameters, such as the gas pressure, RF power, and deposition time, are carefully controlled to achieve the desired film properties, such as thickness, composition, and uniformity. These parameters can be adjusted based on the specific requirements of the application.

In this work, the growth pressure was selected to 5 mTorr, while the RF power was maintained at 100 W with argon gas at flow rate 50 sccm. Two SnO_2 based sensor samples were prepared with sputtering times of 90 min and 180 min to obtain an estimated thickness 300 nm to 600 nm, respectively. As prepared RF sputtered coated substrates were further calcined at 800 °C for 2h.
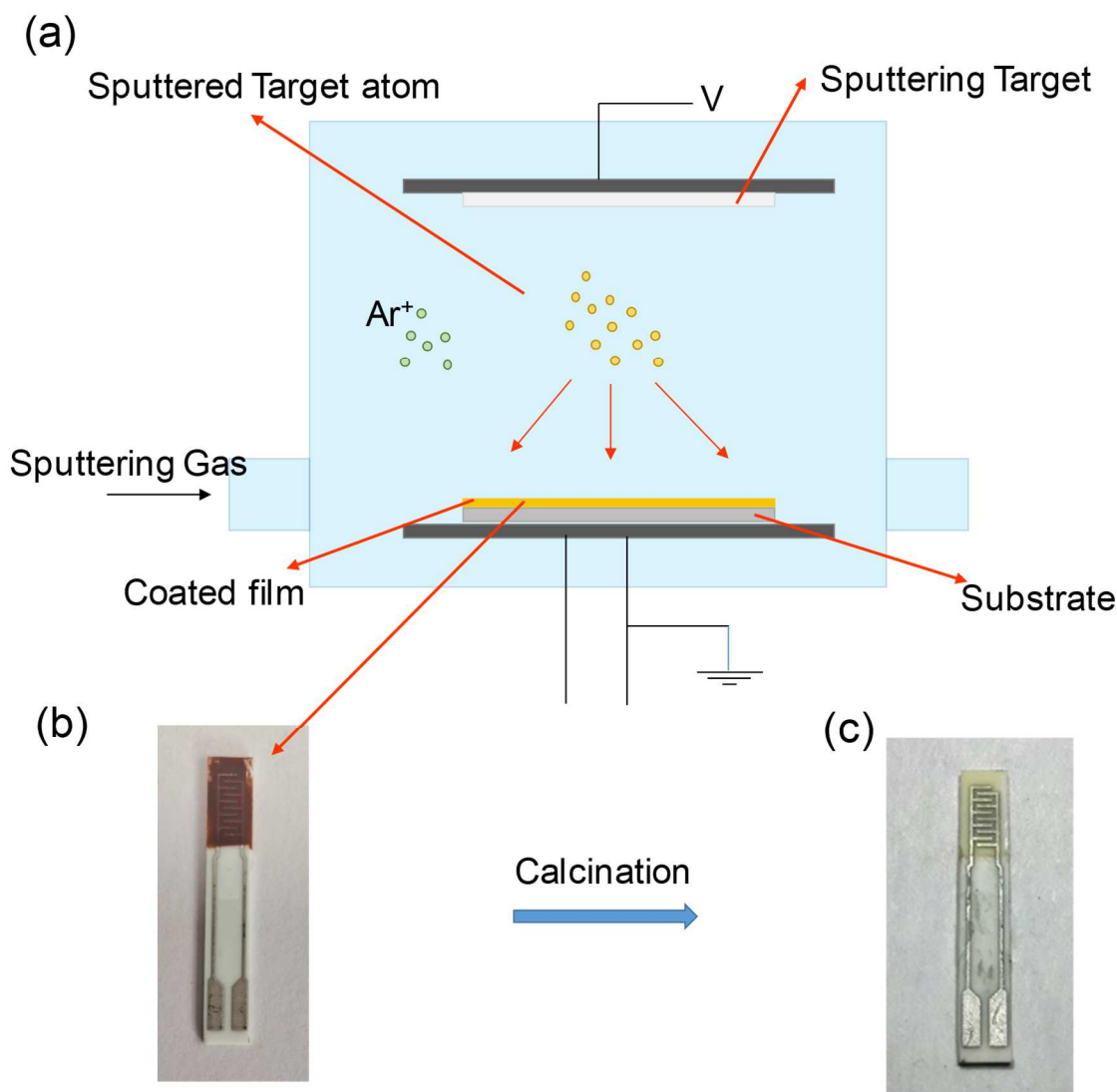
Figure 2.2 (a) Schematic of RF sputtering instrument, (b) RF sputtered as prepared SnO_2 coated sample, (c) SnO_2 coated sensor obtained after calcination of RF sputtered sensor at 800 °C.

2.3.2 Screen-printing process

Commercial SnO_2 powder (Tin (IV) oxide, 99.6% metals basis, Alfa Aesar) of an average particle size of 10 μm was mixed with 1,2-propanediol (98%, Alfa Aesar) in the weight ratio of 30:1 and then milled to obtain a homogenous paste. Using a screen with a mesh size of 420, the paste was pressed through the holes of the screen onto the sensor substrate. After printing the coated substrate

was kept at 50 °C for 2 h and followed by heat treatment in air at 600 °C for 2 h in a muffle furnace. Schematic of the screen-printing process and the actual set-up is shown in Figure 2.3.
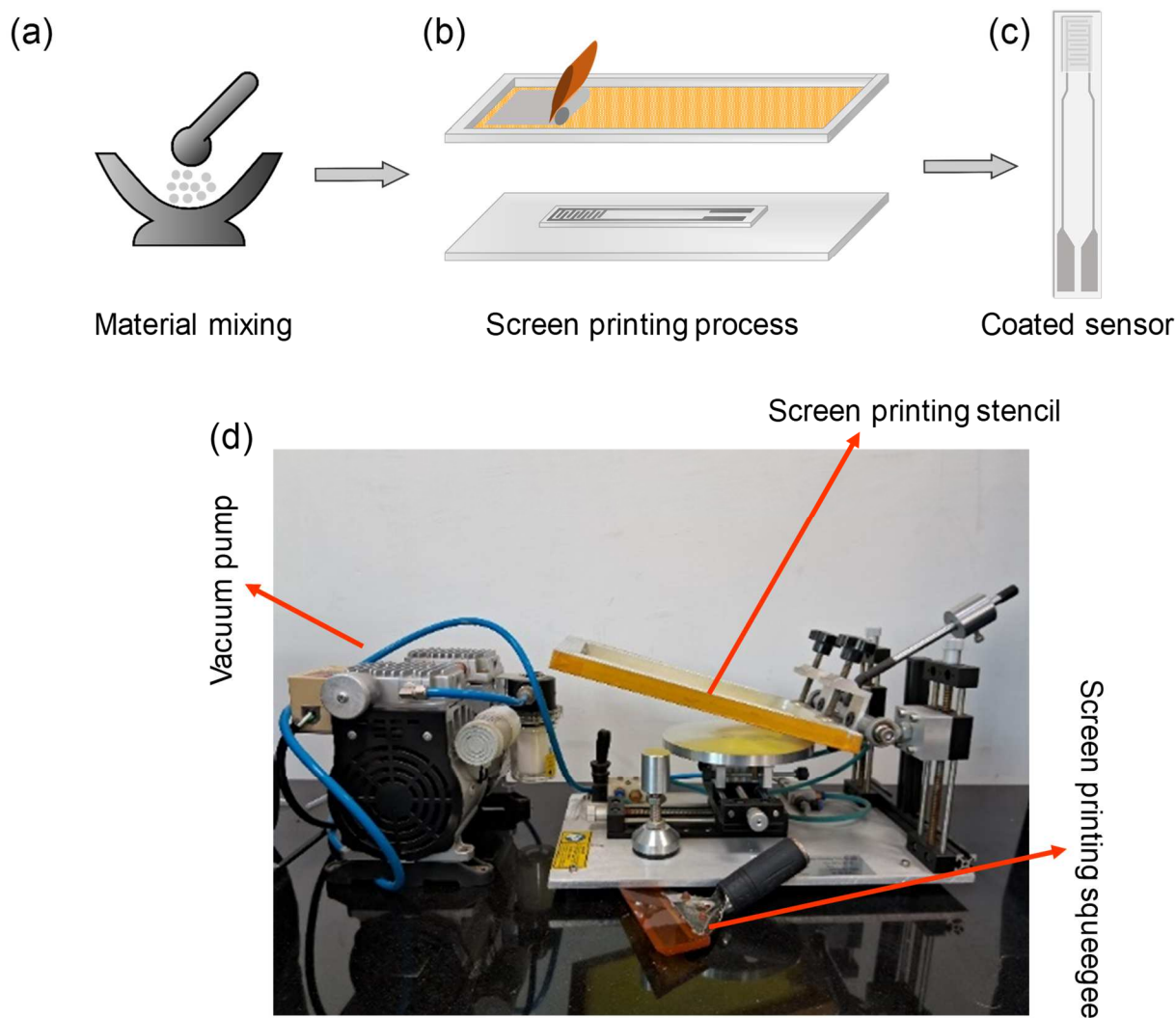
Figure 2.3 Screen-printing process: (a) preparing a homogenous paste of sensing material powder and 1,2-propanediol, (b) applying paste through a screen on sensor substrate, (c) screen-printed sensor obtained after calcination or annealing under flowing nitrogen, (d) screen-printing set up used in this.

Similarly, GaN powder (Gallium nitride, 99.99 % purity, Sigma-Aldrich) was mixed with 1,2-propanediol and screen-printed on sensing substrate. The coated sensor was dried at 50 °C for 2 h

under nitrogen followed by heating at 500 °C for 2 h under nitrogen as GaN powder oxidizes under air at higher temperatures.

2.4 Filter layer deposition on sensors

For the deposition of filter layer on the gas sensors, polymeric precursor was diluted with anhydrous toluene (40 % by volume) and mixing was done for 5 hours at 500 rpm using magnetic stirrer at room temperature to obtain pre-ceramic polymeric solution. The prepared sensors (RF sputtered and screen-printed) were dipped in pre-ceramic polymeric solutions for 3-4 min and were taken out at a speed of 2 cm min^{-1} followed by subsequent pyrolysis under argon environment using the pyrolysis parameters as described in section 2.1; Pt-heater on the back-side of sensor support was protected during dip-coating process using scotch tape during polymer coating process and then carefully removed before pyrolysis. For depositing multiple coatings of filter layer, pyrolysis of polymer coated sensor was done before depositing the successive layers. The schematic of dip-coating process on sensor substrate is shown in the Figure 2.4.
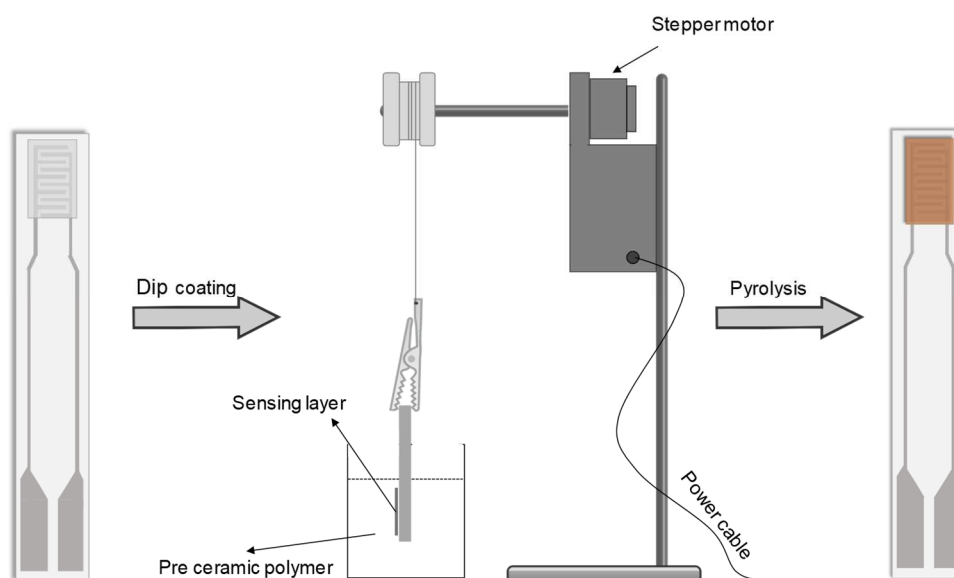
Figure 2.4 Schematic of dip-coating process for filter layer deposition on gas sensors.

2.5 Gas sensing measurement and data acquisition

To characterize gas sensors, DC-resistance measurements were performed using digital multimeter (Keithley 2450 SMU). Uncoated and filter-coated sensors were mounted in a

gas sensing measurement set-up which was connected to a computer controlled gas mixing system. Transient response of sensors were recorded during exposure to CO (50 ppm, 70 ppm and 100 ppm) and H_2 (50 ppm, 500 ppm and 1000 ppm) in nitrogen gas with a flow rate of 100 sccm at different temperatures. All measurements were performed several times to check the reproducibility. More details about the gas sensing experiment set-up is described in chapter 3.

2.6 Characterization techniques

2.6.1 Nuclear magnetic resonance (NMR) spectroscopy

^{29}Si, ^{13}C and ^1H liquid-state Nuclear Magnetic Resonance (NMR) spectra of as-received polymeric precursors were recorded on JNM-ECS NMR spectrometer with operating frequency range of 400 MHz using $CDCl_3$ (deuterated chloroform) as solvent. Spectra were referenced to tetramethylsilane (TMS) as the internal reference.

2.6.2 Attenuated total reflection infrared (ATR-IR) spectroscopy

ATR-IR spectra of air-sensitive polymeric precursors and synthesized ceramics were recorded using the Smart iTX single-reflection ATR assembly and Nicolet iS50 FTIR spectrometer (Thermo Scientific) with a spectral range from 500 to 4000 cm^{-1} with a spectral resolution of 1 cm^{-1}.

2.6.3 Thermal gravimetric analysis (TGA)

Thermal analysis of polymeric precursors were measured using SDT 650 Simultaneous Thermal Analyzer (TA Instruments) to obtain the ceramic yield of the precursors. Samples were heated from room temperature to 900 °C at a rate of 5 °C min^{-1} under argon atmosphere at a flow rate of 25 ml min^{-1}.

2.6.4 X-ray diffraction (XRD)

PANalytical X'Pert diffractometer with flat sample stage was used to record the X-Ray diffraction pattern of sensing powders (SnO_2 and GaN), sensing layer coated gas sensors and polymer-derived based filter coated gas sensors using Cu Kα radiation in the reflection scanning mode in the 2θ of 20-80°. Structures of the samples were analyzed using X'pert highscore software.

2.6.5 Raman spectroscopy

Raman spectra of samples were recorded on a confocal micro-Raman spectrometer (LabRAM HR Evolution, Horiba France SAS) with excitation laser wavelength of 532 nm Laser with 5% of

maximum laser power at laser head (100 mW) in the range of 500 to 4000 cm^{-1}. The data acquisition and analysis of Raman spectra was performed by labSpec 6 software.

2.6.6   Nitrogen adsorption-desorption measurements

The porosity measurements of the polymer-derived ceramic powders were done by determining nitrogen adsorption and desorption isotherms at 77 K using Anton Paar Autosorb IQ2 instrument. The samples were pre heated at 150 °C for 8 h under vacuum to remove moisture and other contaminants. Recorded isotherms was analyzed by Brunauer, Emmett and Teller (BET) method to calculate surface area from the linear part of the adsorption isotherm [121] and pore-size distribution (PSD) was calculated by Saito-Foley (SF) method [49].

2.6.7   Scanning electron microscopy (SEM)

The surface morphology and thickness of filter layers were investigated using JEOL JSM 6610LV instrument at an acceleration voltage of 10-15 kV. To measure the thickness of filter layer coated on sensor substrates, samples were carefully cut such that the cross-section of filter-coated sensors was visible for imaging purpose. To avoid the charging effect, samples were sputtered with a thin layer of conductive coating material using Auto Fine Coaters JFC-1600.

2.6.8   Elemental analysis

Elemental analysis of the ceramics synthesized were analyzed using LECO CS744 (carbon analyzer) and LECO ONH836 (N and O analyzer).

LECO CS744: The probe material is weighed and mixed with tungsten and iron and is put in an Al$_2$O$_3$ crucible. Then crucible is placed in high frequency electric field, and burned up in oxygen stream. Carbon contained in the sample is completely oxidized to CO$_2$ gas before passing it through an IR-cell. Quantification of carbon content is done based on Lambert Beer's law, where the absorption is proportional to the carbon content. Standards used were steel.

LECO ONH 836: The nitrogen and oxygen contents are measured using a hot extraction method. The powder sample is packed in a tin capsule and then placed in a nickel basket. The powdered samples is burned in a graphite crucible at about 2700 °C under helium atmosphere. Oxygen in the sample reacts with carbon forming carbon monoxide which is oxidized to CO$_2$ using CuO catalyst. CO$_2$ formed is quantitatively analyzed by IR absorption spectroscopy. Thermally released nitrogen is measured by thermal conductivity measurement. Oxygen anlaysis is accomplished in an IR-cell

as CO_2. Formed CO can be oxidized using Pt/SiO_2 catalyzer. N & O contents in the sample is compared with calibration standards like steel.

Chapter 3. Design and realization of experimental gas sensing set-up

This chapter describes the design and principle of operation of experimental gas sensing system ─ which has been constructed within the frame of this thesis work ─ for studying of selectivity of uncoated and filter coated gas sensors.

3.1 Experimental setup

Figure 3.1a and 3.1b illustrates schematic of the experimental setup and real picture of the experimental set-up which has been constructed. The set-up consists of the following components:

(i)   Gas flow and pressure regulation system: gas cylinders, pressure regulators, pressure gauges, valves, tubings

(ii)   Gas mixing station: mass flow controller (MFC), multi gas controller, stainless steel tubing, PTFE tubing, and valves

(iii)   Sensing chamber and data acquisition: Sensing chamber, multimeters, power sources, computer system with a LabVIEW program for data acquisition
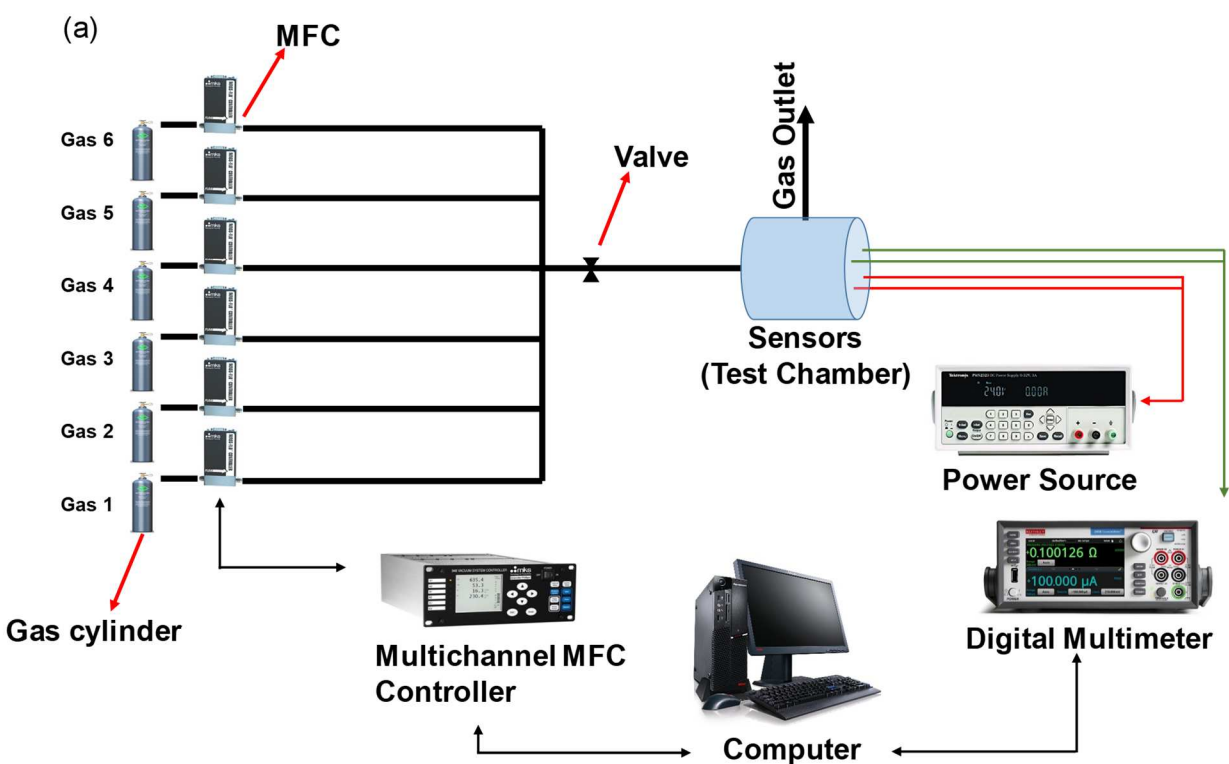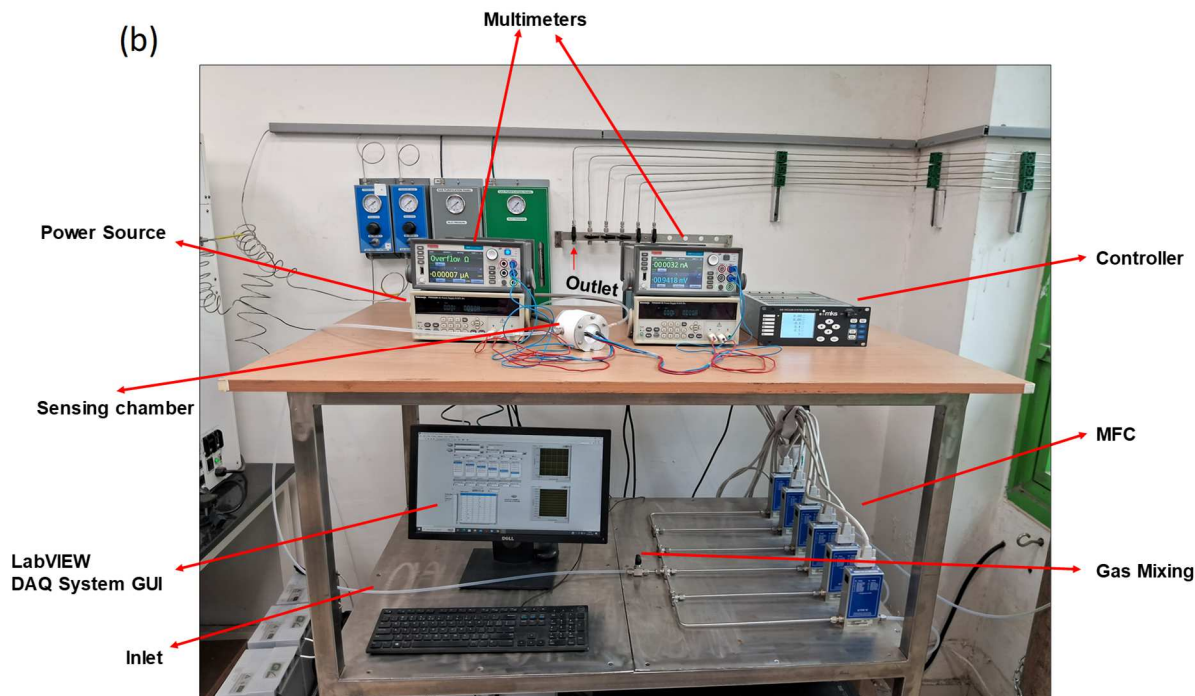
Figure 3.1 (a) Schematic view of the experimental gas sensing set-up, (b) actual photo the set-up that has been constructed in this thesis work. It consists of mass flow controllers, multi gas controller, multimeters, power source, gas sensing chamber and computer with LabVIEW DAC.

Different parts of the set-up are described in the following sections:

3.1.1 Gas mixing station
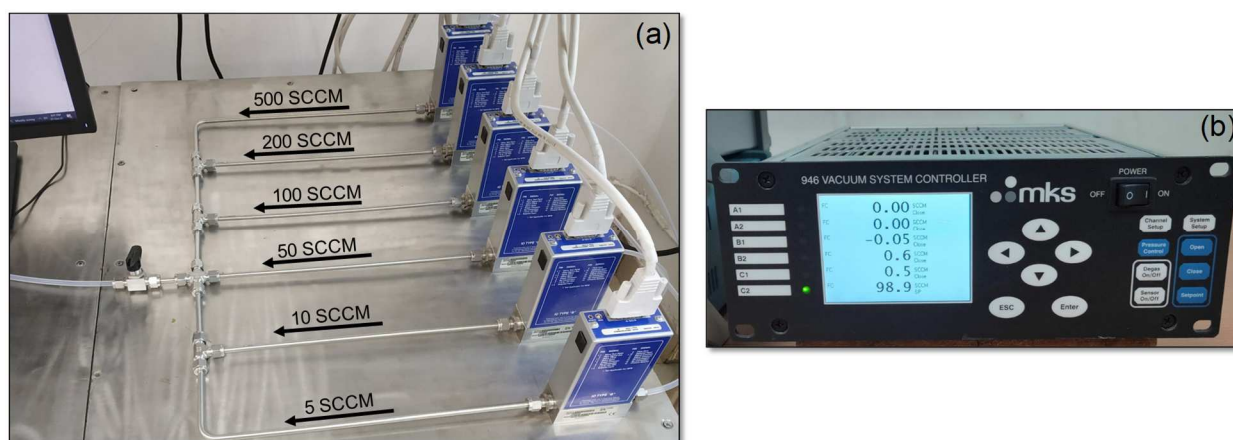
Figure 3.2 Gas mixing bench consisting of six-channel gas mixing station having (a) six mass controllers interconnected with stainless tubing, (b) multi gas controller.

To perform gas sensing measurements towards various concentrations of gases, a gas mixing facility is required. The gas mixing bench consists of six mass flow controllers (Type GM50A, MKS Instruments). Mass flow controllers are fixed on a test bench, as shown in Figure 3.2. The maximum flow rates of these controllers are 5, 10, 50, 100, 200, and 500 cm^3 min^{-1}. The MFCs cable has a settling time of less than 750 milliseconds, a typical closed conductance leak rate of less than 0.1 % of full scale, and the MFCs usual accuracy is about 1% of set point for 20 to 100 % full scale and 0.2 % of full scale for 2 to 20 % full scale. MFCs to withstand a maximum pressure of 1000 psig during testing, with a burst pressure of roughly 1500 psig. The MFCs are externally controlled by multi gas controller (946 Vacuum System Controller, MKS Instruments). A connection was established between the MFCs and the multi gas controller using a RS485 interface.

3.1.2 Gas sensing chamber and data acquisition

The gas sensing chamber was prepared using teflon material which is stable up to 350 °C. The two ports of the sensing chamber was clipped with stainless steel plate and screws to form leak proof system. In the sensing chamber, two sensors are connected through multimeters (Keithley 2450) for measuring resistance and power sources (PWS2326 DC power supply) for heating gas sensors.

The power supply maximum voltage output has been limited to a predefined amount to avoid damage of sensing chamber material.

In order to control the flow through individual mass flow controller connected channels and measuring resistance of sensors, the experimental set-up is operated by a LabVIEW program developed indigenously, as shown in Figure 3.3.
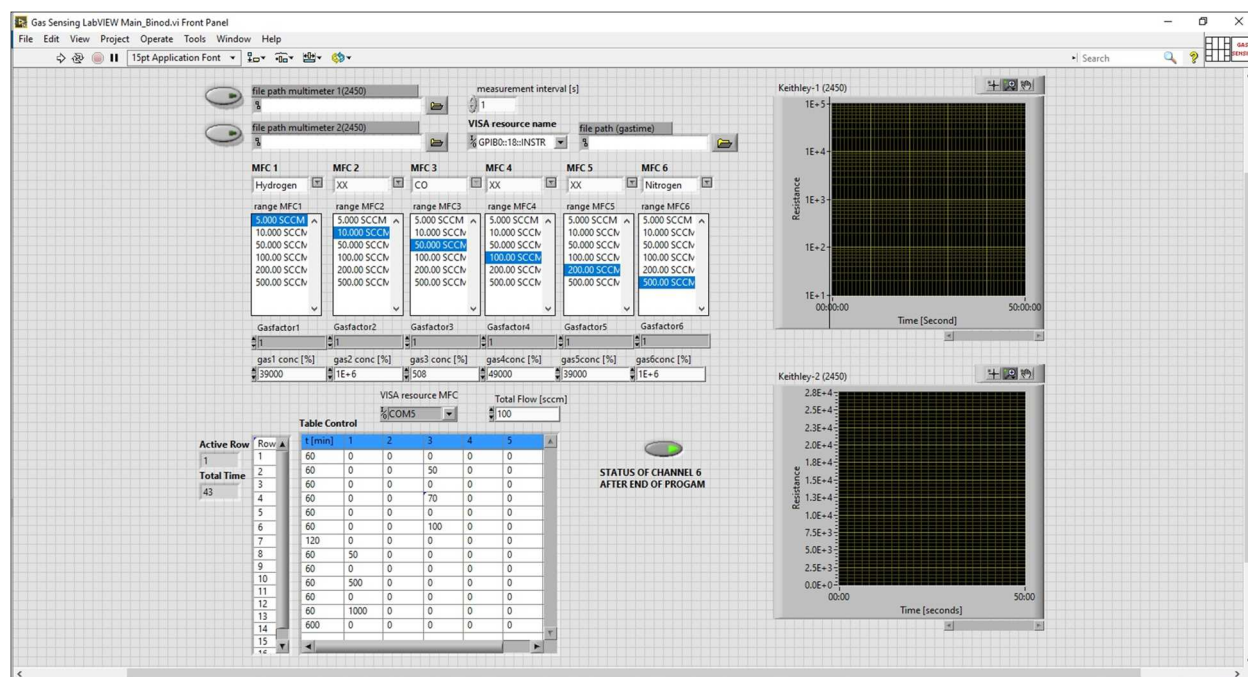
Figure 3.3 Graphical user interface (GUI) for controlling gas concentration and data acquisition using LabVIEW.

Data acquisition system for the gas sensing, developed by VISA (Virtual Instrument Software Architecture) tool in LabVIEW plays a crucial role in facilitating instrument control and data acquisition within the LabVIEW programming environment. It serves as a standardized interface, enabling seamless communication with various instruments and devices. One of the primary benefits of the VISA tool is its ability to support multiple communication protocols, including General Purpose Interface Bus (GPIB), Universal Serial Bus (USB), Ethernet, and serial interfaces [122]. This flexibility allows LabVIEW users to connect and interact with a diverse array of instruments, such as oscilloscopes, multimeters, spectrum analyzers, and more. VISA ensures

platform independence, means easily ported across different operating systems and hardware platforms, without requiring extensive modifications. VISA also offers a comprehensive set of functions (Visa tool command list, Write, Read, Clear, Close, Trigger, Property node, Open, and Write from file) and tools specifically designed for instrument control tasks. Users can utilize these functions to send commands, receive data, configure instrument settings, and perform other essential operations. The tool simplifies the communication process and frees developers from dealing with low-level protocol intricacies, enabling them to focus on higher-level application development. Moreover, VISA seamlessly integrates with other features and libraries in the LabVIEW environment. This integration allows users to combine instrument control with data processing, analysis, and visualization capabilities, creating powerful test and measurement systems.

3.2 Procedure for gas sensing measurements

After placing the sensors inside sensor chamber into the appropriate ports, the chamber is securely tightly closed and gas sensors are connected to the multimeters and power sources. After flushing sensor chamber with nitrogen to eliminate oxygen and moisture, a continuous supply of inert gas at a flow rate of 100 sccm is maintained from one of the MFCs for few hours at room temperature. Thereafter, sensors are heated up to the required temperatures of measurements. After resistance of the sensors at the set temperature flowing nitrogen gets stable, sensing measurements are started. The transient resistance data of gas sensors are recorded using the developed LabVIEW program for data acquisition, as shown in Figure 3.3.

Chapter 4. Synthesis of microporous polymer-derived ceramics

This chapter discusses synthesis and characterization of various polymer-derived ceramics for selecting suitable precursor(s) for developing microporous filter layer on chemiresistor gas sensors for enhancement of gas sensing selectivity. SiOC, SiCN and SiC ceramics were synthesized by pyrolysis of commercially available vinyl-functionalized polysiloxane (XP RV 200), polysilazane (Durazane 1800) and ally hydrido polycarbosilane (SMP10), respectively, under argon. Pyrolysis process of the forming PDCs using various precursor used in this works are already described in section 2.1. The structure of polymeric precursors are studied by liquid-state NMR spectroscopy and ATR-IR spectroscopy; polymer-to-ceramic transformation, structural characterizations and porosity characteristics of the synthesized ceramics are investigated. In the following synthesis and characterization of each of the synthesized ceramics are discussed.

4.1   SiOC ceramic derived from vinyl-functionalized polysiloxane

Molecular structure of as-received pre-ceramic polymer vinyl-functionalized polysiloxane is shown in Figure 4.1 (as provided from the supplier, Evonik Industries AG, Germany) and verified using ^{1}H, ^{13}C and ^{29}Si liquid-state NMR and ATR-IR spectroscopic characterization.
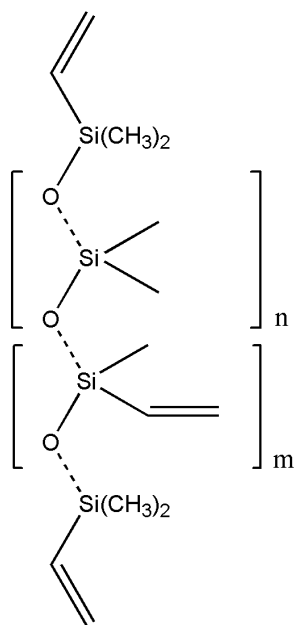
Figure 4.1 Molecular structure of vinyl-functionalized polysiloxane (XP RV 200).

4.1.1 Liquid-state NMR characterization
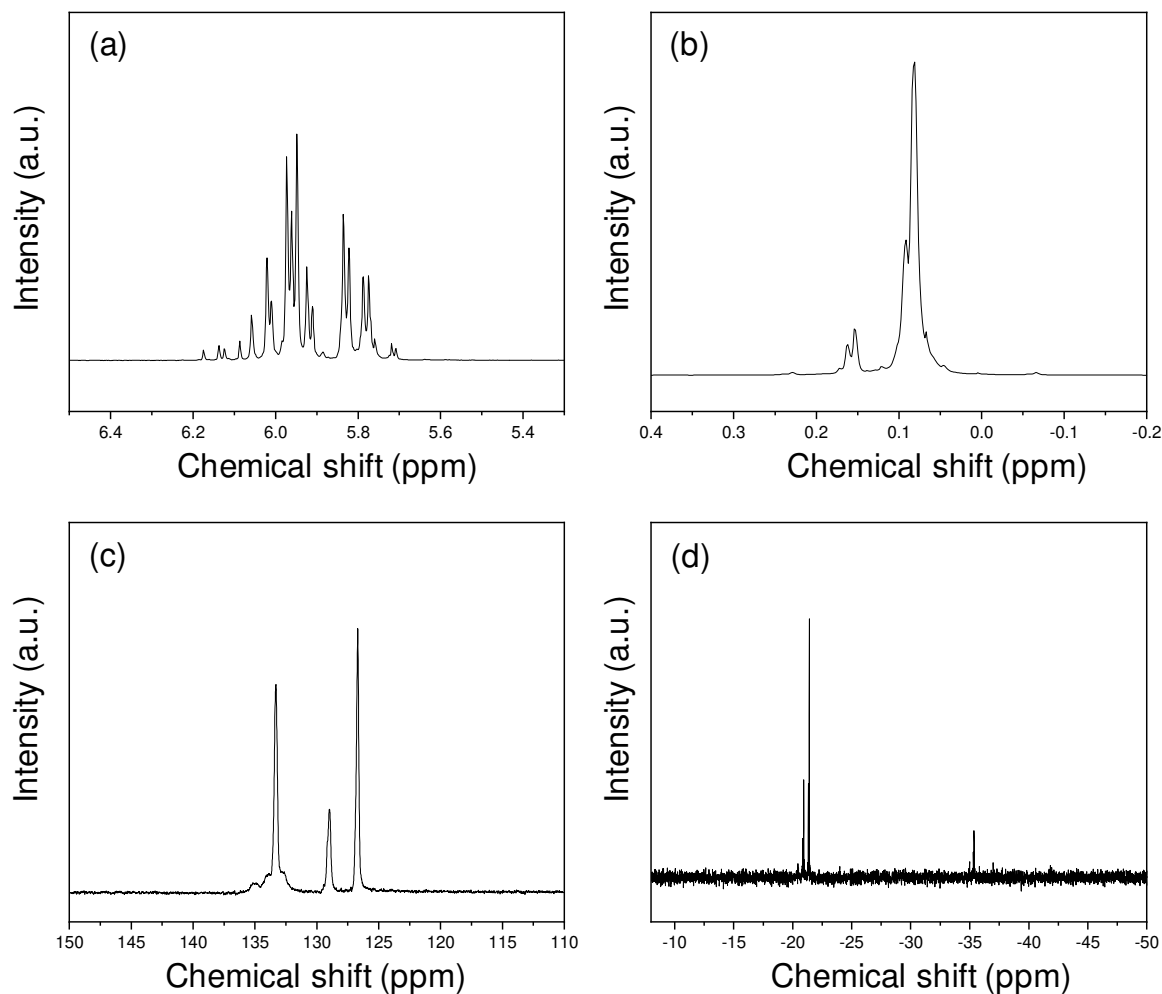
Figure 4.2 Liquid-state NMR spectrum of vinyl-functionalized polysiloxane, CDCl$_3$ as solvent: (a-b) ^{1}H, (c) ^{13}C, (d) ^{29}Si.

^{1}H NMR: The proton NMR (^{1}H) spectrum (Figure 4.2 a-b) shows two resonance peaks ranging from -0.01 to 0.24 ppm indicating the methyl groups bonding in the polymeric structure which is Si-O-(CH$_3$)$_2$, in agreement with reference [123]. The resonance shift ranging from 5.6 to 6.1 ppm indicates the vinyl group bonding in the polymer which is (CH$_2$=CH) Si-O.

^{13}C NMR: The carbon (^{13}C) NMR of the polymer shows three resonance peaks at 126 ppm, 128 ppm and 133 ppm, as shown in Figure 4.2 c, are consistent with the vinyl groups present in the polymeric structure [123].

^{29}Si NMR: Figure 4.2 d represents the silicon (^{29}Si) NMR of the polysiloxane polymer (XP RV 200). It shows two resonance peaks, one ranging from -20 to -21.5 ppm corresponds to the methyl silicon bonding in the polymer which O−Si(CH$_3$)$_2$−O and the other resonance at around -35 ppm indicating the vinyl bonding to the silicon group which is (CH$_3$)(CH$_2$=CH)-Si-O [123].

4.1.2 ATR-IR characterization

In Figure 4.3, the infrared spectra of the polymeric precursor and the SiOC ceramic are shown.
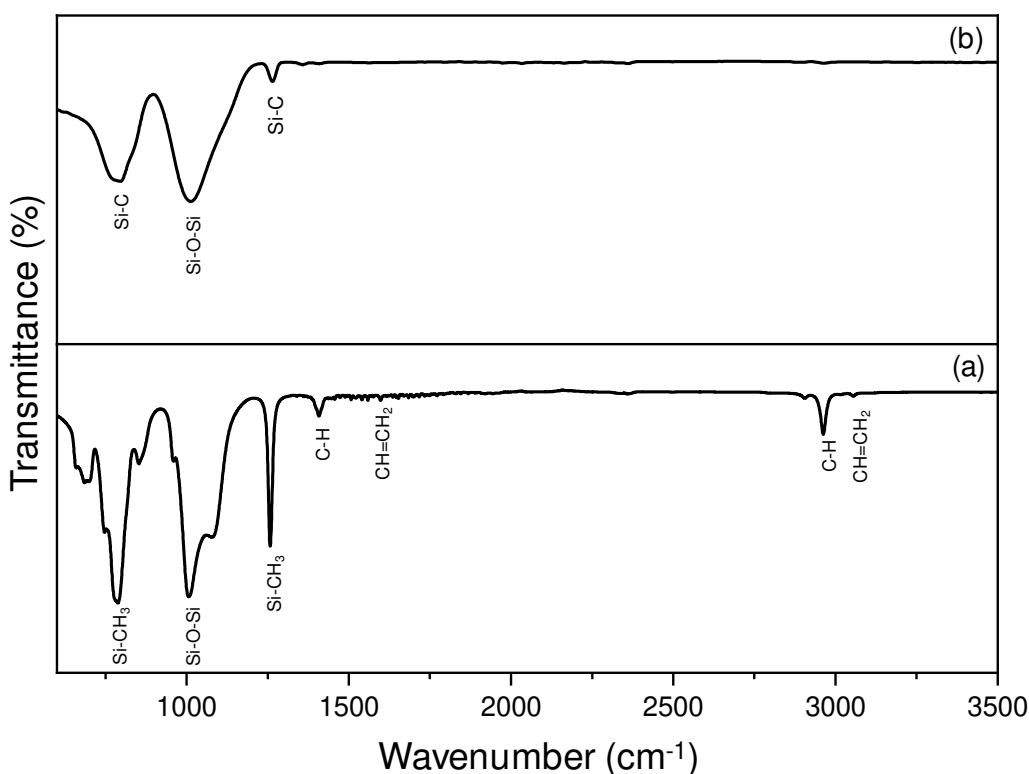
Figure 4.3 ATR-IR spectrum of: (a) vinyl-functionalized polysiloxane (XP RV 200), and (b) SiOC ceramic obtained after pyrolysis at 700 °C.

The bands observed at 788, 1007, 1257, 1407, 1597, 2962, and 3054 cm^{-1} correspond to Si-CH$_3$, Si-O-Si, Si-CH$_3$, C-H, CH=CH$_2$, C-H, and CH=CH$_2$, respectively [124, 125]. Very low intense bands at 1597 and 3054 cm^{-1} indicating presence of very low amount of vinyl groups which is in agreement with the data supplied by the supplier and these bands are absent in SiOC ceramic

confirming the cross-linking reaction of vinyl group followed by pyrolysis process leading to ceramic formation.

4.1.3   TGA characterization: Polymer-to-ceramic transformation

In order to determine polymer-to-ceramic transformation temperature and to select required pyrolysis temperature for depositing ceramic filter on gas sensors, Thermal Gravimetric Analysis (TGA) was done. Figure 4.4 shows the ceramic yield from the polymeric precursor was about 32% by mass. Simultaneously measuring the gases released via mass spectrometry during mass loss indicates the polymer-to-ceramic transformation of vinyl-functionalized polysiloxane occurs by mass loss in several steps due to the release of oligomers (vinyl component, $m/z = 28$) with low molecular weight polymers comprising a small number of repeat units between 150 and 400 °C and due to release of methane ($m/z = 16$) and hydrogen ($m/z = 2$) during ceramization process in the temperature range of 500–650 °C [120]. Negligible mass loss is observed above 700 °C indicating completion of the ceramization process.
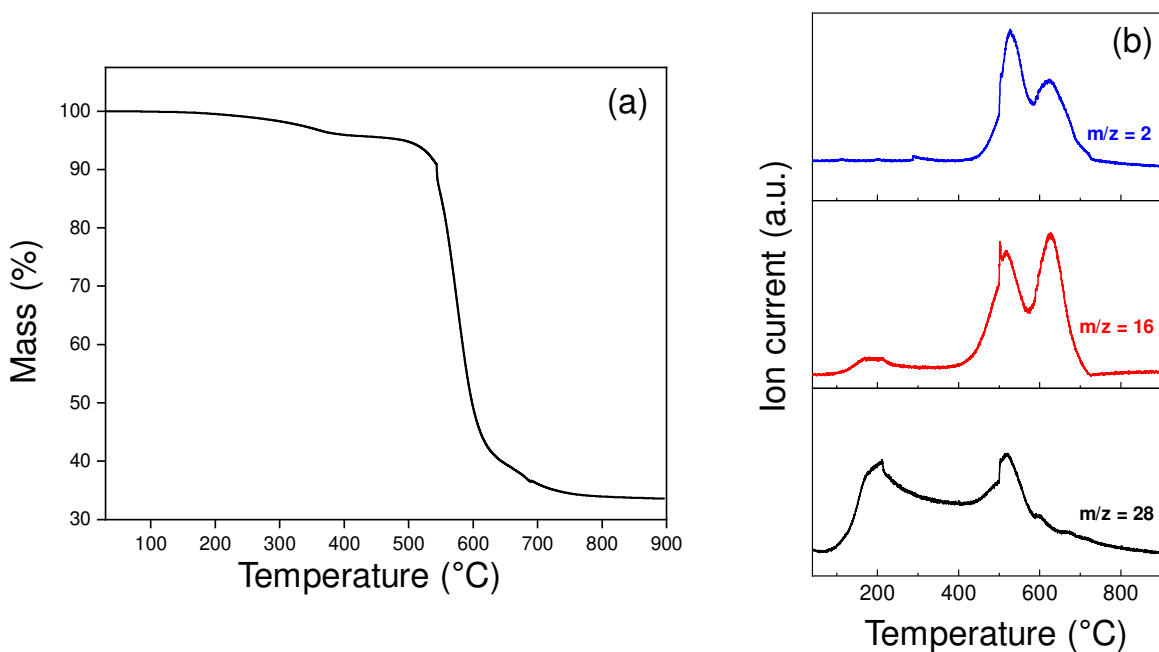
Figure 4.4 (a) Thermal gravimetric analysis (TGA), and (b) Mass spectra of vinyl functionalized polysiloxane, XP RV 200 (heating at 5 °C min⁻¹ under argon atmosphere).

The gases (H_2, CH_4, etc.) which are released during polymer-to-ceramic conversion generate micropores - in the range of the molecular diameter of released gases - in the synthesized ceramics. This step by which pore-generation occurs in polymer-derived ceramics is the crucial step for obtaining microporous polymer-derived ceramics. According to a densification mechanism based on surface reaction accommodated by viscous flow [126], microporosity is eliminated when the pyrolysis temperature of ceramization step is increased. Therefore, selection of pyrolysis temperature is one of the main factor to obtain suitable microporous ceramic filter layer for enhancement of gas sensing selectivity of gas sensors.

Based on TGA data (Figure 4.4) of the polymer, ceramic powders were synthesized by pyrolyzing vinyl-functionalized polysiloxane under argon at three different temperatures: 700 °C, 800 °C and 900 °C and further structural characterizations (XRD, porosity characterization) are performed on the SiOC ceramics obtained by the pyrolysis of polymers at and above 700 °C.

4.1.4   XRD characterization

X-ray powder diffraction patterns of SiOC powders prepared from vinyl functionalized polysiloxane at 700 °C, 800 °C and 900 °C are presented in Figure 4.5. The obtained ceramics are found to be amorphous in nature as confirmed by featureless broad x-ray diffraction pattern.
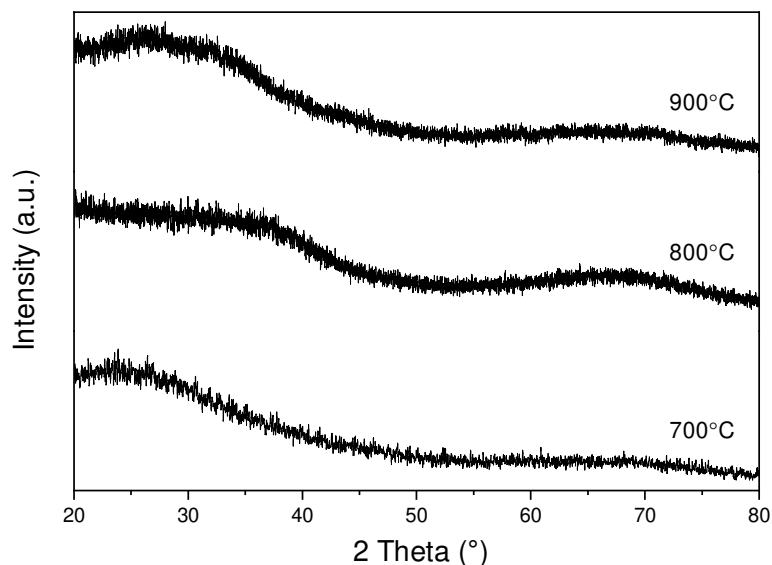
Figure 4.5 X-ray powder diffraction patterns of XP RV 200 polysiloxane-derived SiOC ceramics obtained by pyrolyzing under argon at 700 °C, 800 °C and 900 °C.

4.1.5 Porosity characteristics
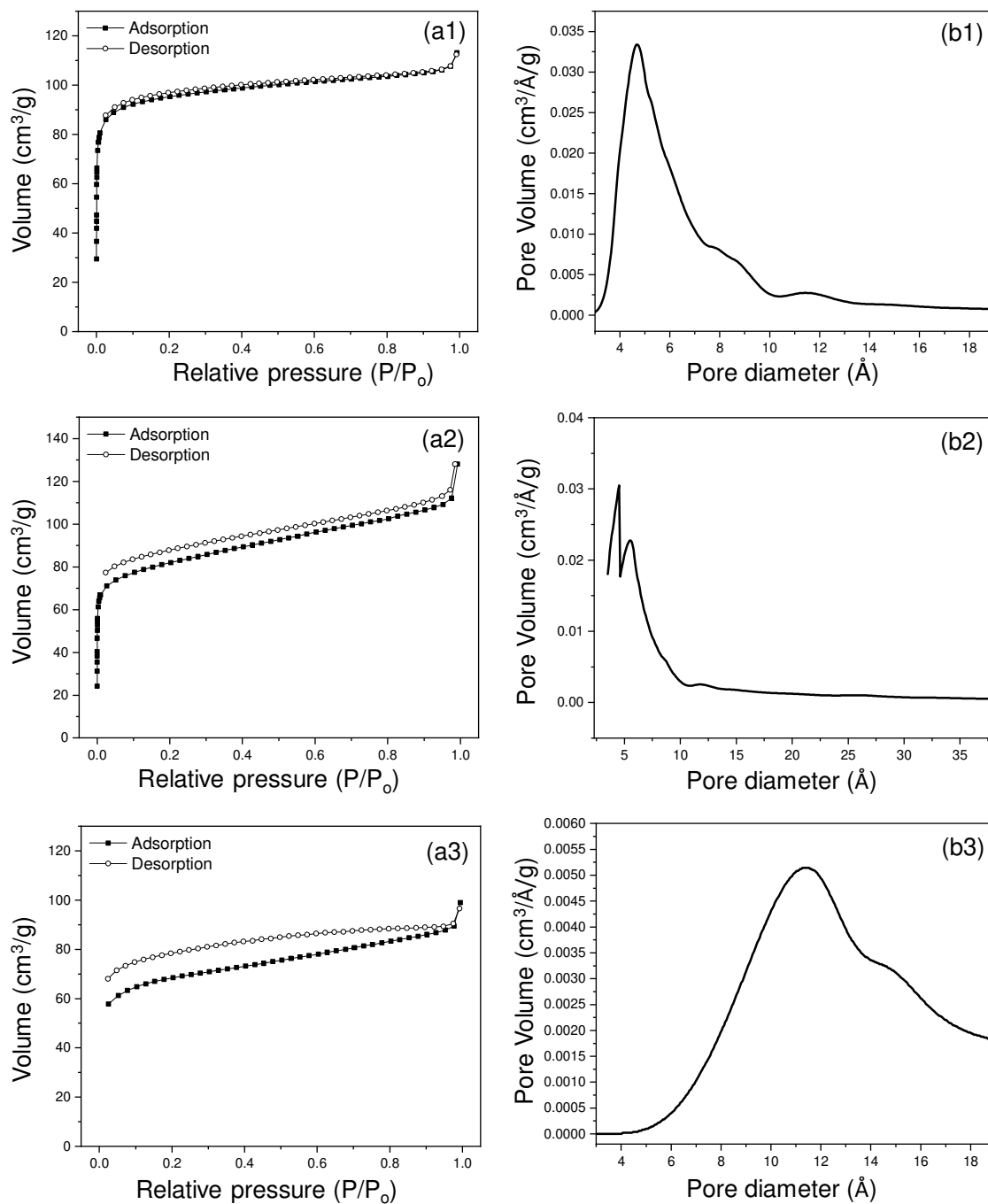
Figure 4.6 Nitrogen adsorption-desorption isotherms measured at 77 K (a1-a3) and pore-size distribution using Saito-Foley method (b1-b3) of SiOC powders obtained after pyrolysis of vinyl-functionalized polysiloxane at 700 °C, 800 °C, and 900 °C.

The nitrogen gas adsorption-desorption isotherms of SiOC ceramics powder prepared from the pyrolysis of vinyl-functionalized polysiloxane are shown in Figure 4.6. The isotherm analysis of the SiOC ceramic powder samples obtained after pyrolysis at 700 °C, 800 °C and 900 °C is found to be of Type I according to the IUPAC classification [127]. These results confirms that SiOC which is obtained at 700 ℃ is microporous with a pore diameter of about ~4.6 Å whereas the pore-size (pore-diameter) of the SiOC ceramics prepared by pyrolysis at 800 ℃ and 900 ℃ is found be larger ─ bimodal pore-size distribution of about 4.6 Å and 5.6 Å for 800 ℃ sample and more than 11.3 Å for 900 ℃ sample. BET specific surface area of the samples are summarized in Table 4.1 along with samples prepared using other precursors described in sections 4.2 & 4.3. Elemental chemical composition of as-synthesized SiOC powder at 700 °C is found be about 44 wt% Si, 33 wt% O and 23 wt% C.

4.2 SiCN ceramic derived from polysilazane

Commercially available polysilazane (Durazane 1800) was used for the synthesis of SiCN-based ceramics. Molecular structure of the as received polymeric precursor has been studied using ^{1}H, ^{29}Si and ^{13}C liquid-state NMR spectroscopy and ATR-IR spectroscopy.

4.2.1 Liquid-state NMR characterization

^{1}H NMR: ^{1}H spectrum of Durazane 1800 is shown in Figure 4.7 a. SiH protons appear as multiplets between 4.1 and 4.9 ppm [127]. NH resonace can be observed as broad signals at around 0.76 ppm [128]. SiCH$_3$ protons are found as a broad resonance at around 0 ppm [128]. Methyl groups can be seen as broad resonance centred at 0 ppm due to different chemical environments. Multiplets between 5.6 and 6.2 ppm can be attributed to the presence of Si-CH=CH$_2$ [129].

^{13}C NMR: In the ^{13}C spectrum (Figure 4.7 b), the signals corresponding to methyl and vinyl groups attached to silicon are observed. The broad resonance signals in the range from -2.4 to 5 ppm is related to Si-CH$_3$. Chemical shifts of 131–142 ppm are assigned to Si-CH=CH$_2$ [8][129].

^{29}Si NMR: In agreement with the literature [130] the recorded broad resonance peaks ranging from -16 to -27 ppm confirms dominant peaks are related to [-Si(CH$_3$)(CH=CH$_2$)-NH], Figure 4.7 c. The minor ^{29}Si peak at -32.6 ppm could be assigned to presence of trace amount of -SiH$_2$- functionality [131].
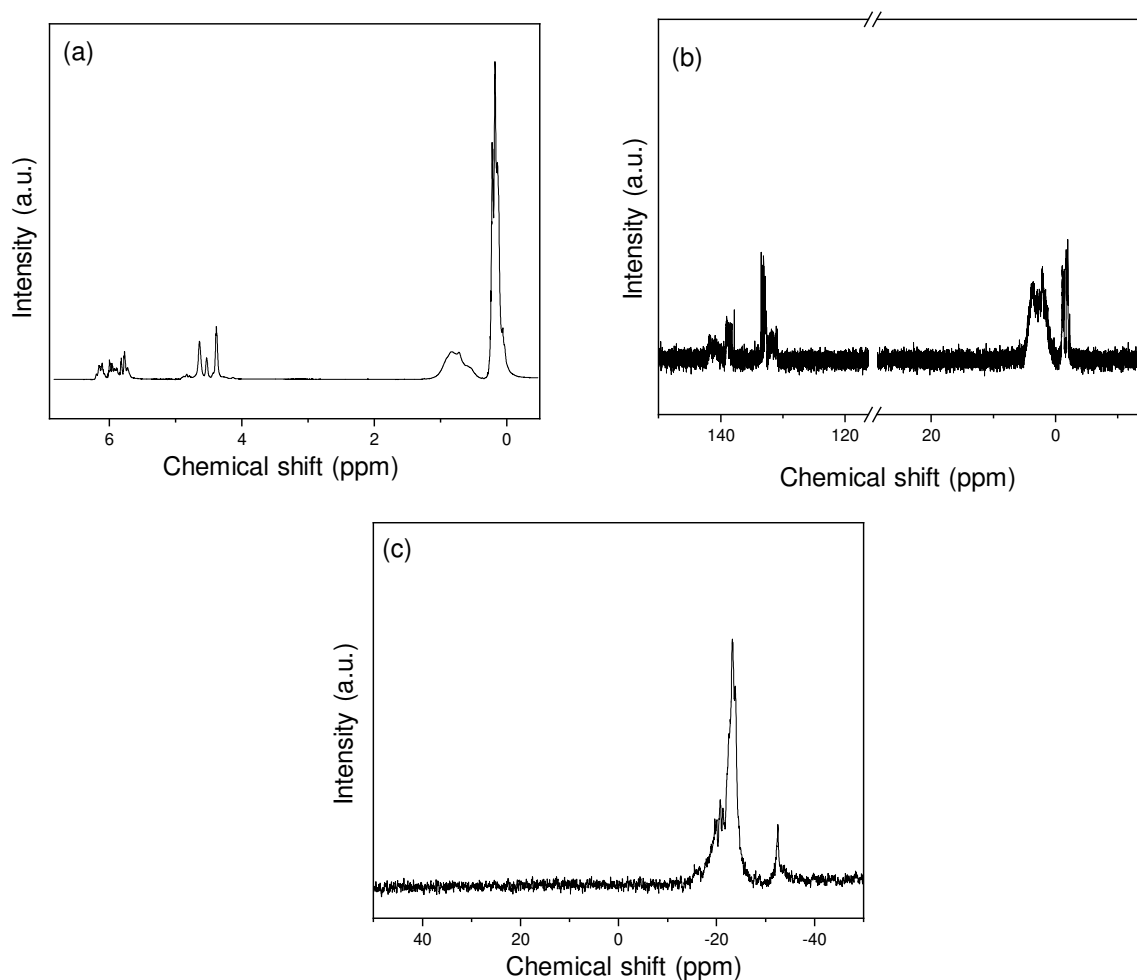
Figure 4.7 Liquid-state NMR of: (a) ^{1}H spectrum, (b) ^{13}C spectrum, (c) ^{29}Si spectrum of Durazane 1800, using CDCl$_3$ as solvent.

4.2.2 ATR-IR characterization

ATR-IR spectrum of polymeric precursor Durazane 1800 is shown in Figure 4.8 a. Absorption bands lines at 870, 1157, 1253, 1402, 1584, 2117, 2957, 3047 and 3387 cm^{-1} correspond to Si-N, Si-NH-Si, Si-CH$_3$, CH=CH$_2$, C=C, Si-H, C-H, CH=CH$_2$, N-H functional groups [128]. For the SiCN ceramic obtained at 800 °C, a broad absorption band ranging from 750 to 1100 cm^{-1} is assigned to Si-C and Si-N bonds.
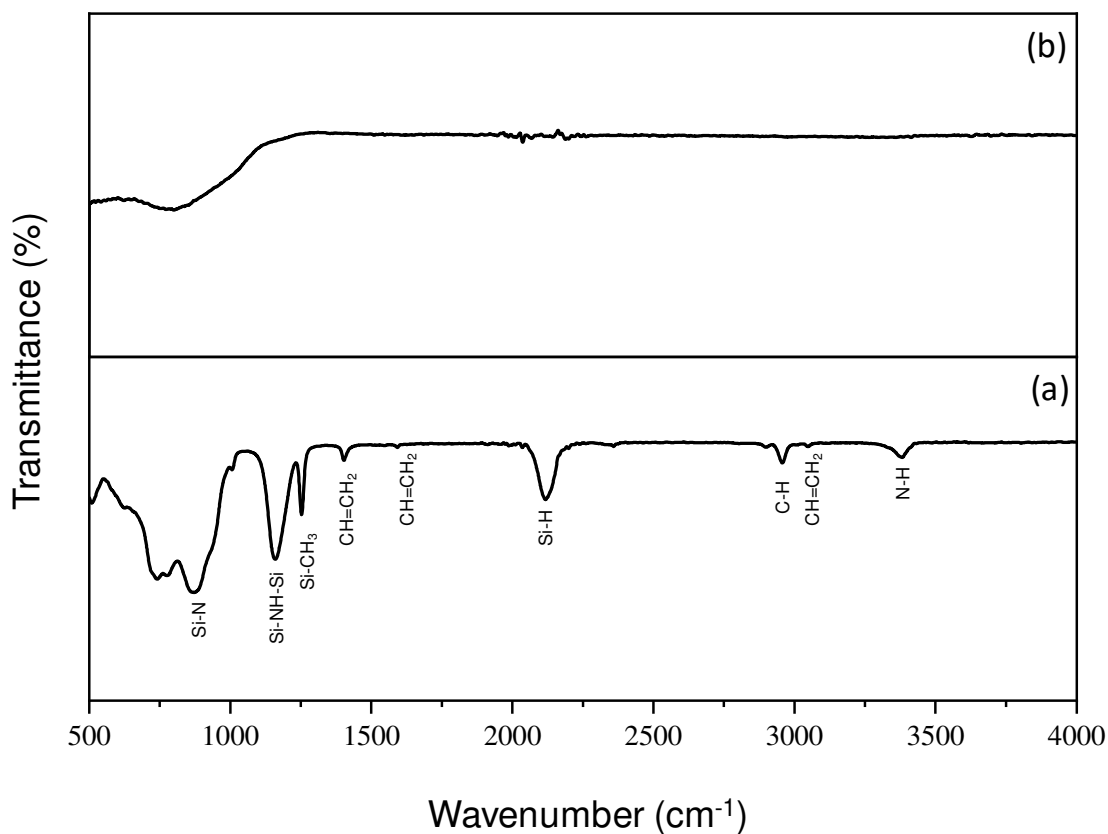
Figure 4.8 ATR IR spectra of (a) precursor Durazane 1800, and (b) SiCN derived by pyrolysis of the polymeric precursor at 800 °C.

Based on above liquid-state NMR and ATR-IR spectroscopic measurements, molecular structure of Durazane 1800 is proposed as shown in Figure 4.9.
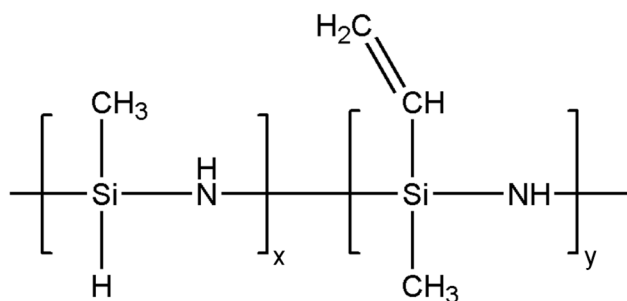
Figure 4.9 Molecular structure of polysilazane (Durazane 1800) polymer.

4.2.3   TGA characterization: Polymer-to-ceramic transformation

Figure 4.10 shows TGA curve of polymer Durazane 1800 indicating that mass of lost in three steps. Mass spectrometry data shows that during cross-linking reaction in the region 150 °C and 300 °C releases hydrogen (m/z = 2), methane (m/z = 16) and vinyl fragments (C_2, m/z = 28) are released. In the second region up to 500 °C ammonia (m/z = 17), methane and vinyl fragments are detected. During the ceramization step from 500 and 750 °C, masses are lost mainly as methane and ammonia. Very low mass is lost above 750 °C indicating completion of polymer-to-ceramic transformation process with a ceramic yield of ~65 % by mass.
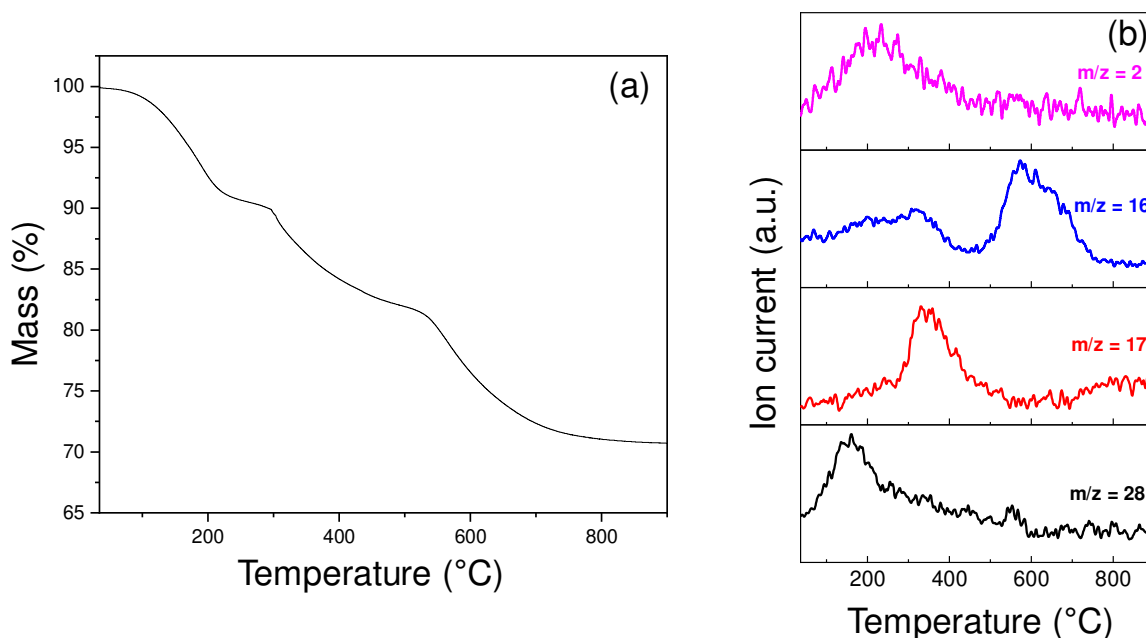
Figure 4.10 (a) Thermal gravimetric analysis (TGA) curve, and (b) Mass spectra of Durazane 1800 (heating at 5 °C min^{-1} under argon atmosphere).

4.2.4   XRD characterization

X-ray diffraction patterns of Durazane 1800 polysilazane derived SiCN ceramics obtained at various temperature (700 °C, 800 °C and 900 °C) are shown in Figure 4.11. Broad x-ray diffractions patterns of ceramics confirms formation of amorphous SiCN.
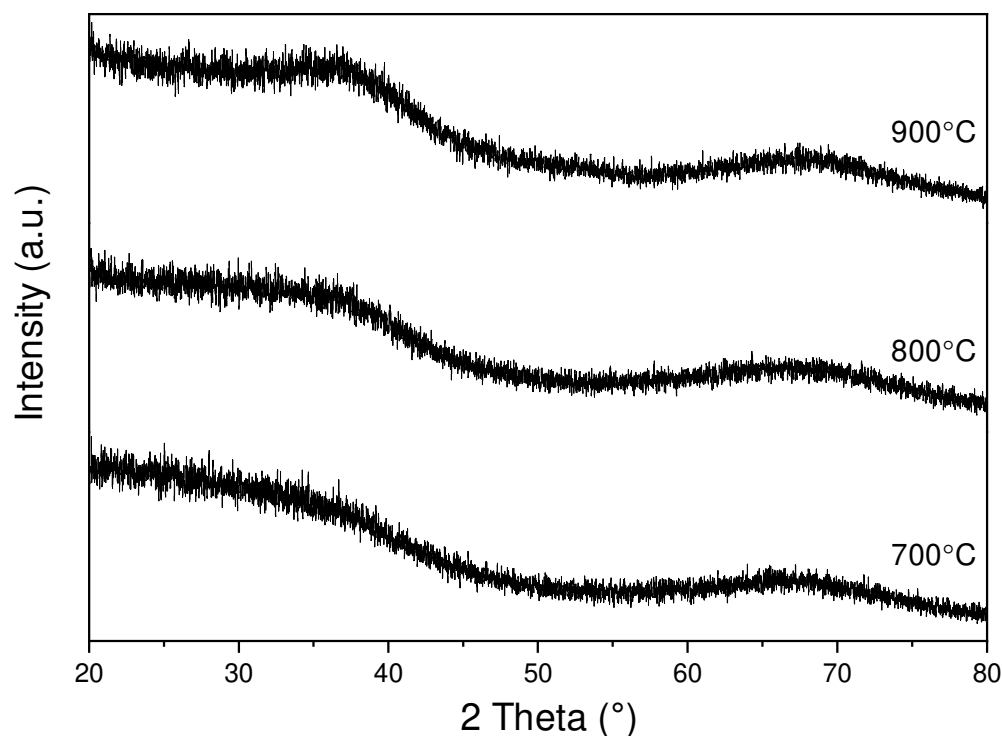
Figure 4.11 X-ray powder diffraction patterns of Durazane 1800 polysilazane-derived SiCN ceramics obtained by pyrolyzing under argon at 700 °C, 800 °C and 900 °C.

4.2.5 Porosity characteristics

Nitrogen adsorption isotherm analysis of powdered samples of SiCN ceramics derived from Durazane 1800 polysilazane were performed and the isotherms are presented in Figure 4.12. Isotherms are found to be of Type III as per IUPAC classification [127][6]; this indicates weak interaction between SiCN ceramic surface and adsorbate (N_2) gas molecules. Very low nitrogen uptake at low relative pressure indicates absence of microporosity and gradual increasing uptake at high relative pressure could be due to interparticle void space or macroporosity. As the synthesized SiCN ceramics are not microporous in nature, therefore, these ceramics were not selected for depositing on a gas sensor substrate for sensing measurements.
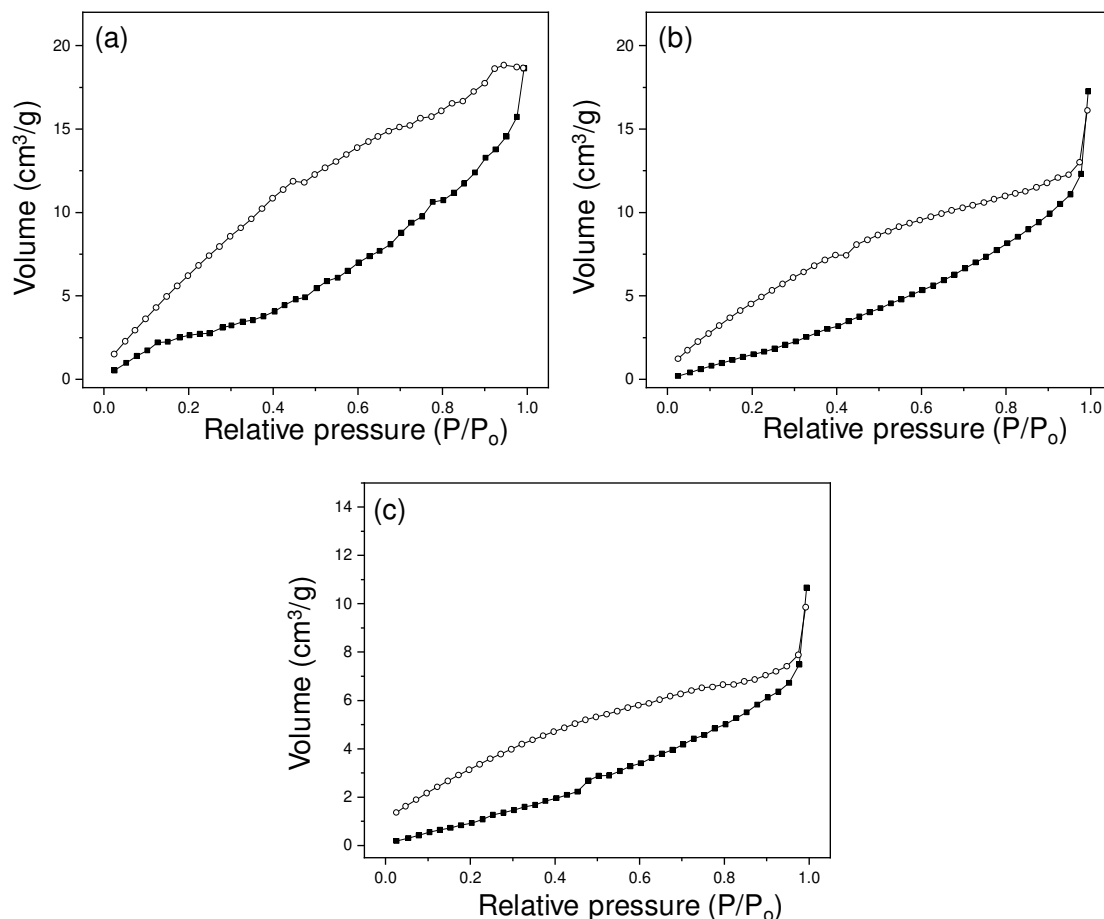
Figure 4.12 Nitrogen adsorption-desorption isotherms measured at 77 K of SiCN powders obtained after pyrolysis of Durazane 1800 polysilazane at: (a) 700 °C, (b) 800 °C, and (c) 900 °C.

4.3 SiC ceramic derived from ally hydrido polycarbosilane

The third and the last polymer used in this work is commercially available ally hydrido polycarbosilane (SMP-10). ^{1}H, ^{13}C and ^{29}Si liquid-state NMR and ATR-IR spectroscopic measurements are done to find the molecular structure of the precursor.

4.3.1 Liquid-state NMR characterization

^{1}H NMR: ^{1}H spectrum of Durazane 1800 is shown in Figure 4.13 a. Resonances corresponding to $CH_2=CH$, SiH, and $SiCH_2$ and SiC_3 are observed in the region of 4.6–5.9, 3.2–4.4, and 1.5–2.0 ppm, respectively [132]. A broad resonance at around 0 ppm corresponds to $SiCH_3$ proton.

13C NMR: In the ^{13}C spectrum (Figure 4.13 b), the resonances corresponding to –CH and CH$_2$ of allyl carbons are observed at 134.3 and 114.3 ppm respectively. Multiple resonances observed in the region 18.5–30.5 ppm are due to –CH$_2$– of allyl groups. Resonances corresponding to Si–CH$_3$ carbon are observed at 0.6 to −15 ppm. These resonance peaks are in agreement with literature [132][11]. Resonances observed in the range 76–78 ppm corresponds to carbon of solvent CDCl$_3$ used.

29Si NMR: Resonances corresponding to silyl linkages are observed in the region −5 to −15 ppm as also observed in literature [132][11].
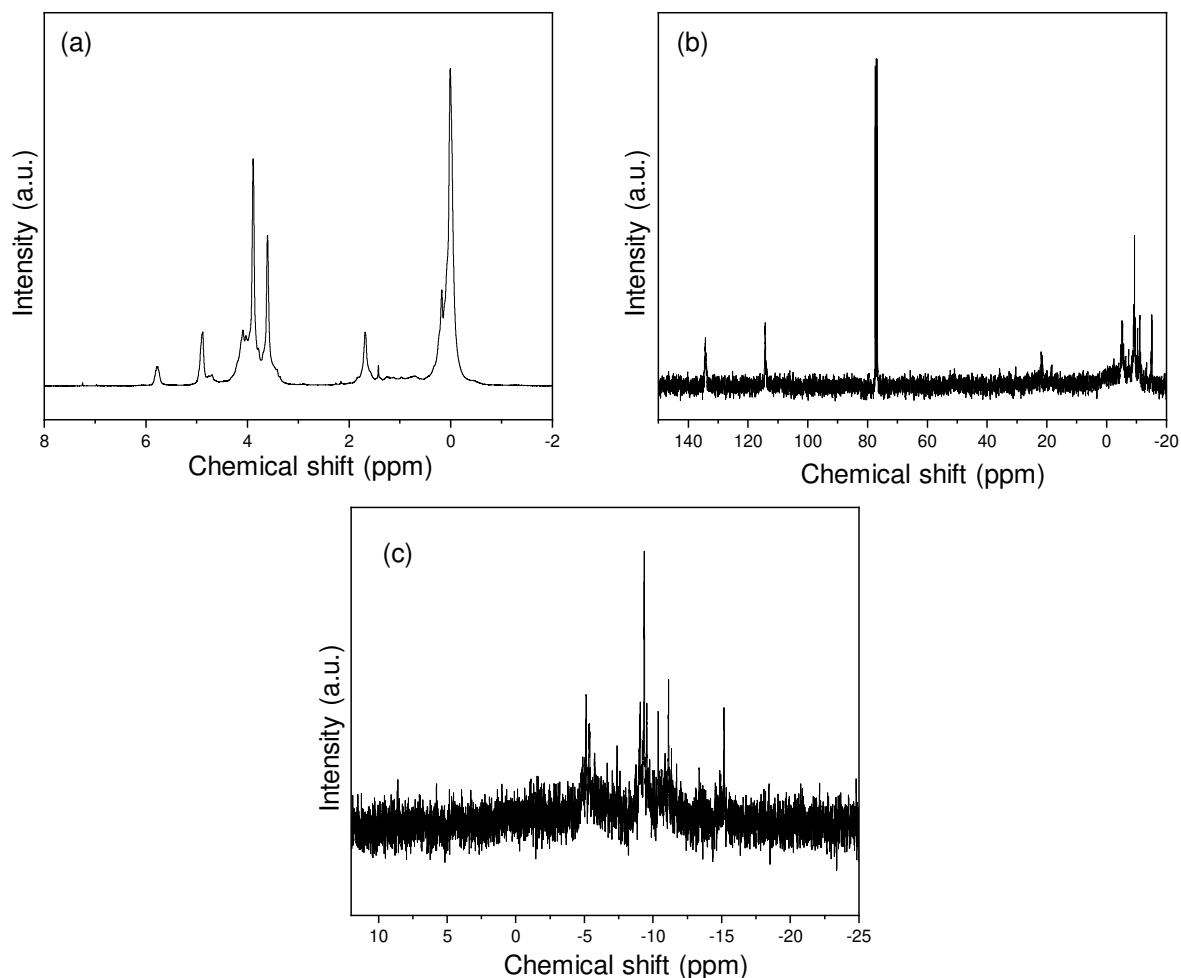
Figure 4.13 Liquid-state NMR spectra of: (a) ^{1}H spectrum, (b) ^{13}C spectrum, (c) ^{29}Si spectrum of SMP-10, using CDCl$_3$ as solvent.

Based on the results of liquid-state NMR and ATR-IR spectroscopic analysis, the structure of allyl hydrido polycarbosilane polymer is presented in Figure 4.14.
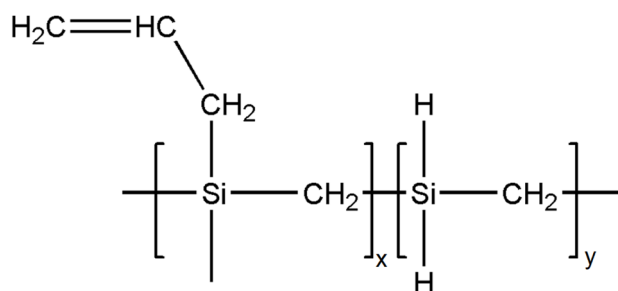
Figure 4.14 Molecular structure of the allyl hydrido polycarbosilane (SMP-10) polymer.

4.3.2 ATR-IR characterization
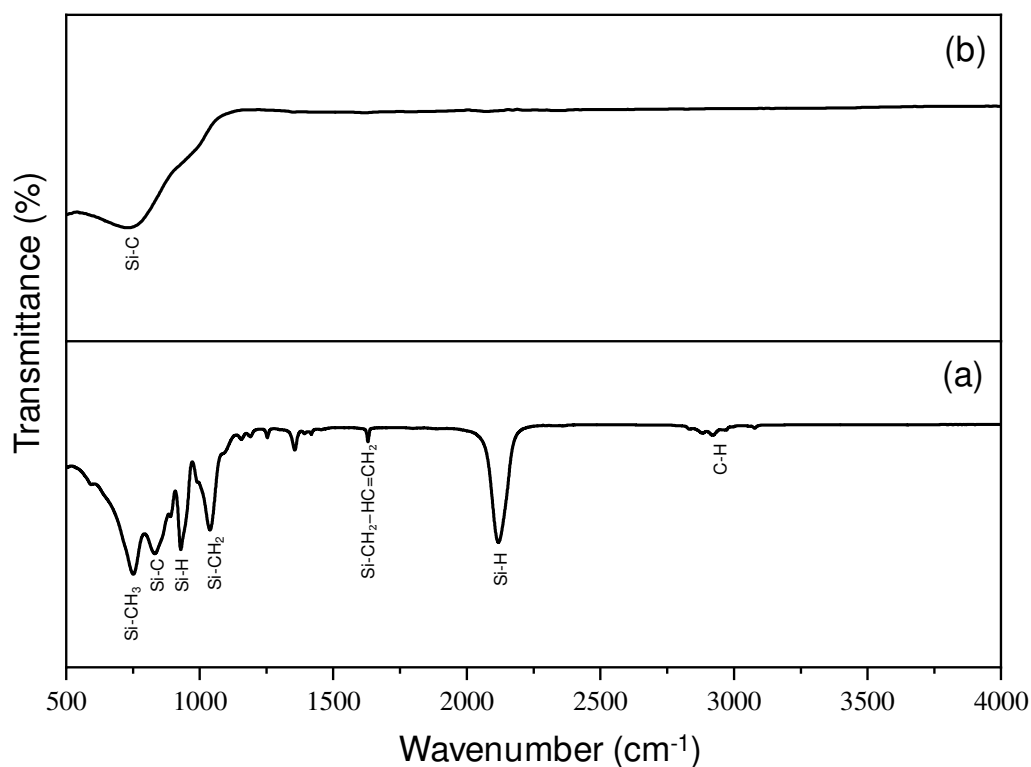
Figure 4.15 ATR-IR spectra of (a) allyl hydrido polycarbosilane (SMP-10) polymer, and (b) SiC powder sample prepared at 700°C.

Figure 4.15 shows infrared spectrum of polymer SMP-10. The bands at 743, 830, 933, 1036, 1629, 2116, 2915, and 3077 cm^{-1} are attributed to functional groups of Si-CH$_3$, Si-C, Si-H, Si-CH$_2$-Si, C=C, Si-H, C-H and C=C, respectively, in agreement with reference [133]. For the ceramic obtained after pyrolysis at 800 °C, broad band corresponding to Si-C is observed confirming formation of SiC ceramic.

4.3.3 TGA characterization: Polymer-to-ceramic transformation

The polymer-to-ceramic transformation of SMP-10 was studied using thermal gravimetric analysis (TGA), Figure 4.16. TGA curve shows mass loss by decomposition of sample occurs in mainly in two steps. In the first mass loss step (150 to 300 °C), hydrogen and oligomer (small polymer fragments) are released. Major mass loss step occurs in the temperature range from 400-800 °C with the release of H$_2$ (m/z = 2), SiH$_4$ (m/z = 32) and CH$_3$SiH$_3$ (m/z = 46). No significant mass loss is observed beyond 800 °C confirming completion of polymer-to-ceramic conversion with a ceramic yield of ~77 % by mass at 800 °C; similar observation were found by Kaur et al. [133][12].
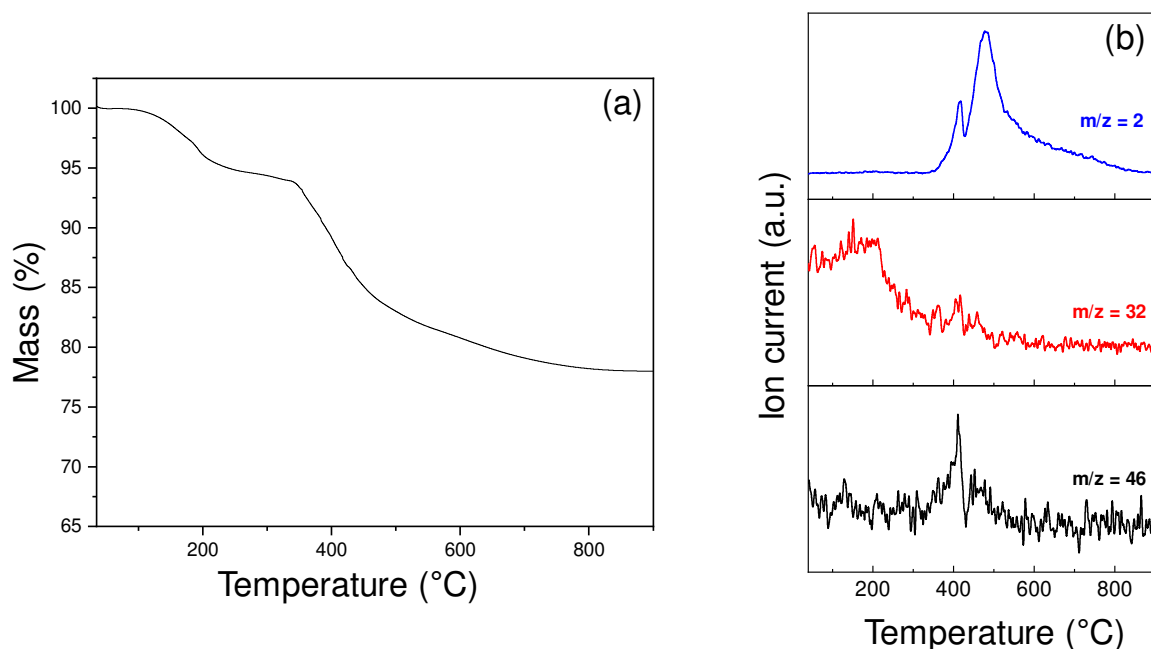
Figure 4.16 (a) Thermal gravimetric analysis (TGA) curve, and (b) Mass spectra of ally hydrido polycarbosilane (SMP 10) (heating at 5 °C min^{-1} under argon atmosphere).

4.3.4 XRD characterization

Figure 4.17 shows XRD pattern of SiC derived by pyrolysis of SMP-10 polycarbosilane at 700 °C, 800 °C and 900 °C. Features broad x-ray diffraction pattern of all the three ceramics synthesized confirms formation of amorphous SiC.
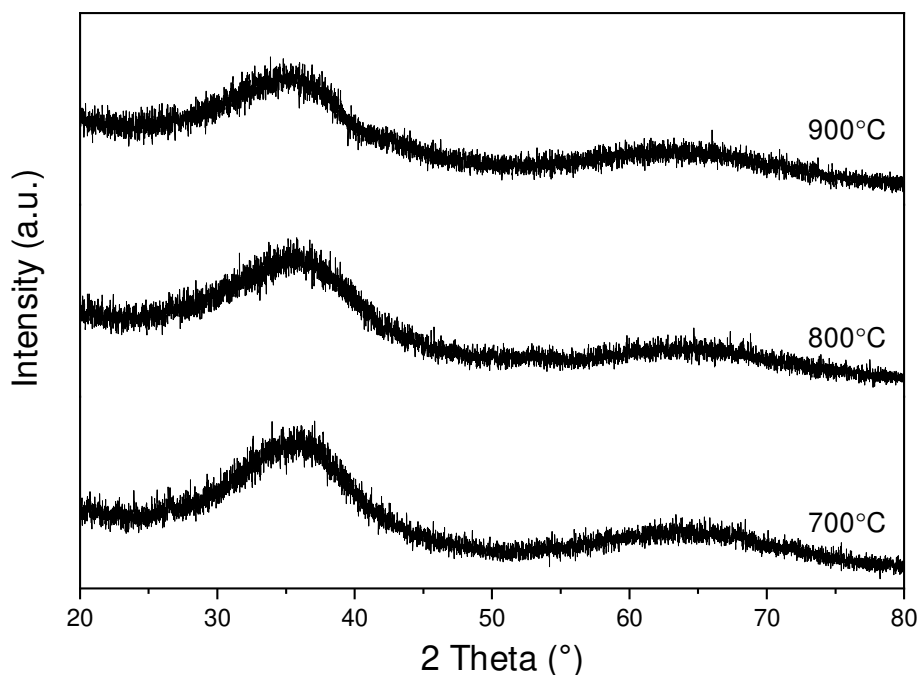
Figure 4.17 X-ray diffraction patterns of SiC prepared by the pyrolysis of SMP-10 under argon at 700 °C, 800 °C and 900 °C.

4.3.5 Porosity characteristics

Nitrogen adsorption measurements were conducted to characterize the porosity of SiC ceramics obtained after pyrolysis at 700°C, 800°C and 900°C; corresponding isotherms are shown in Figure 4.18. All the isotherms are found to be of Type III [126] suggesting weak interaction between SiC surface and adsorbate (N_2) gas molecules and also indicating formation of non-microporous SiC ceramics and therefore, these SiC ceramics are not a prospective ceramic filter for coating on gas sensors for selectivity enhancement.
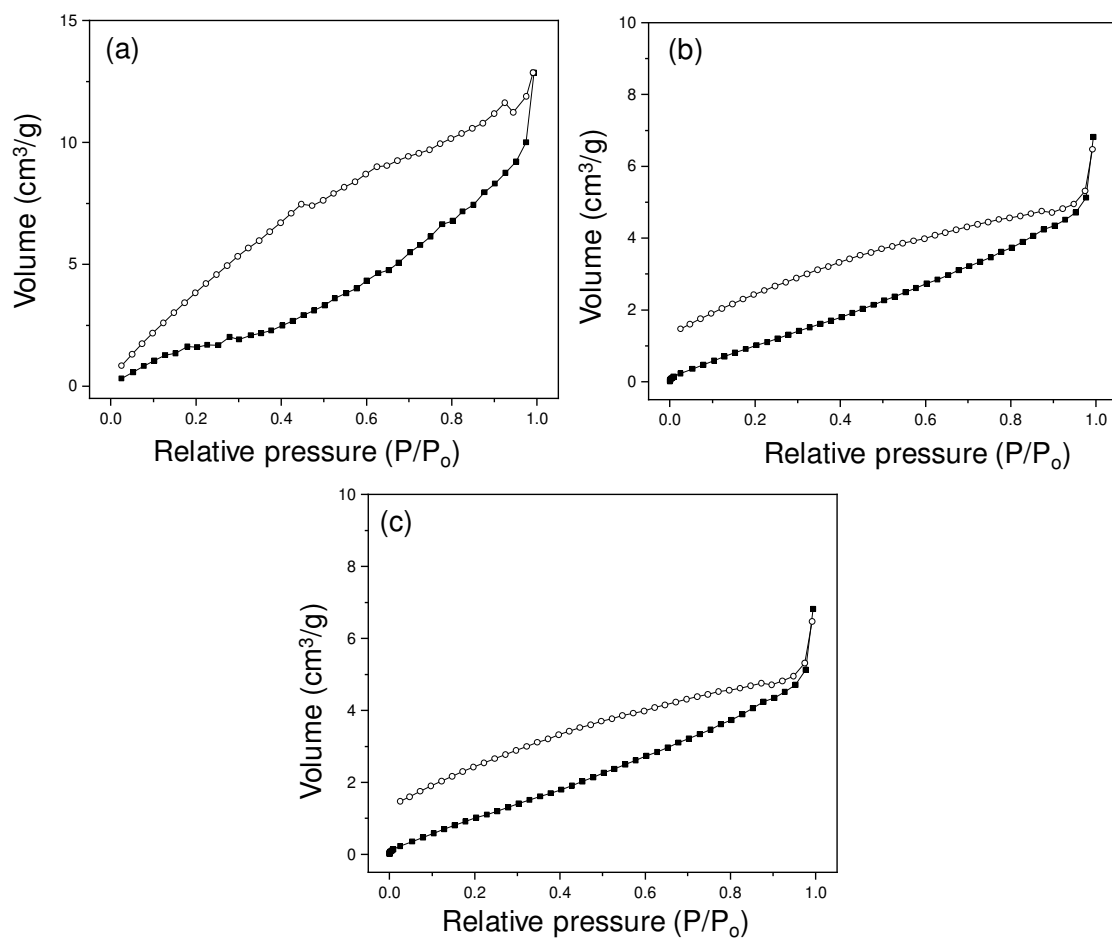
Figure 4.18 Nitrogen adsorption-desorption isotherms measured at 77 K of SiC powders obtained after pyrolysis of SMP-10 at: (a) 700 °C, (b) 800 °C, and (c) 900 °C.

Table 4.1 Summary of nitrogen physisorption measurement results (specific surface area, micropore volume and pore-type) of polymer-derived ceramics (SiOC, SiCN and SiC) by pyrolysis under argon at different temperatures.

Pre-ceramic polymer / Derived ceramics	Pyrolysis temperature & environment	BET specific surface area ($m^2 g^{-1}$)	Micropore volume[a] ($cm^3 g^{-1}$)	Porous structure
XP RV 200 / SiOC	700 °C, argon	350	0.126	microporous
	800 °C, argon	307	0.128	microporous
	900 °C, argon	258	0.089	microporous
HTT 1800 / SiCN	700 °C, argon	11	-	non-porous
	800 °C, argon	11	-	non-porous
	900 °C, argon	6.5	-	non-porous
SMP10 / SiC	700 °C, argon	7.5	-	non-porous
	800 °C, argon	6	-	non-porous
	900 °C, argon	nil	-	non-porous

[a] calculated using SF method

Based on porosity characterization results (Table 4.1), it can be concluded that only the SiOC ceramics derived from polysiloxane (XP RV 200) are found to be microporous (pore-size < 2 nm), whereas SiCN and SiC ceramics are non-porous. Moreover, the SiOC ceramic synthesized at 700 °C with a pore-size of about 4.6 Å and high BET specific surface area of about 350 $m^2 g^{-1}$ is a prospective filter material for deposition on gas sensors, compared to the SiOC ceramics prepared at 800 °C and 900 °C due to relatively larger pore-size. Therefore, for further investigation of polymer-derived porous ceramics as a filter material on gas sensors in this thesis work, solution of XP RV 200 was prepared and SiOC filter layers on gas sensors were deposited at 700 °C under argon.

Chapter 5. Microporous SiOC-coated SnO₂ and SiOC-coated GaN sensors

Trace amount of CO (few ppm) causes a substantial degradation in the fuel cell performance as CO acts as a poison for Pt-based catalysts, therefore, residual CO concentration in the hydrogen rich stream should be monitored. Hence, gas sensing measurements of low CO concentration ranges (50-100 ppm) compared to higher H_2 concentration ranges (50-1000 ppm) have been performed and described in this chapter. Gas sensing performances of SiOC-coated SnO_2 sensor and SiOC-coated GaN sensor ─ obtained by dip-coating of polysiloxane solution on sensing material coated planar alumina substrate with Pt electrodes followed by pyrolysis under inert atmosphere ─ have been studied for the H_2/CO gas sensing selectivity in harsh reducing conditions.

5.1   SiOC-coated SnO₂ sensors

RF sputtered coated SnO_2 sensors (described in section 2.3.3) under exposure to H_2 at 500 ppm and 1000 ppm showed similar very low value of resistance; this indicates that RF sputtered sensors get saturated with H_2 under these concentration ranges. Hence, it is difficult to estimate accurate sensor signals of RF sputtered sensors; details are presented in Annexure I. In the following, structural characterization and sensing performance of screen-printed sensors are discussed.

5.1.1 Structural characterization of uncoated SnO₂ sensor and SiOC-coated SnO₂ sensor
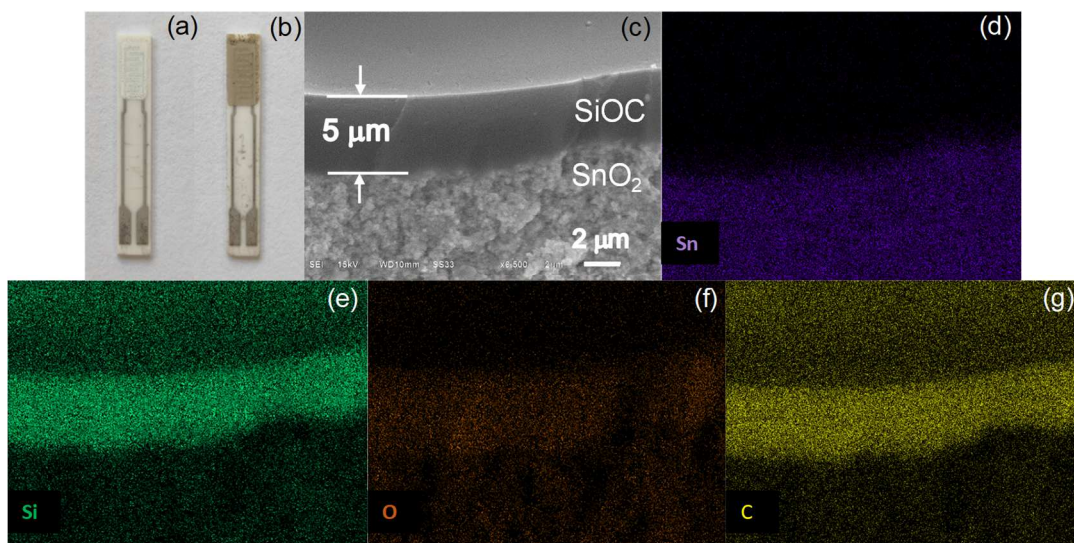
Figure 5.1 Digital images of: (a) SnO₂ coated sensor, (b) two-times polymer-derived SiOC-coated SnO₂ sensor; (c) SEM image of fractured cross-section of SiOC-coated SnO₂ sensor, (d-h) EDS mapping images of elements Sn, Si, O and C in SiOC-coated SnO₂ layer.

SnO$_2$ sensor, prepared by screen-printing method onto sensor substrate, was coated with two-fold SiOC layer by dip-coating of polysiloxane solution followed by pyrolysis process at 700 °C under argon, as described in the experimental procedures (sections 2). SiOC layer is found to be crack-free with a thickness of ~5 μm after two-fold coating/pyrolysis steps, as shown in the cross-sectional view of sensor (Figure 5.1 c). EDS elemental confirms the presence of elements Si, O, C, and Sn in the SiOC-coated SnO$_2$ sensing layer (Figure 5.1 d-g).

XRD measurements of commercial SnO$_2$ powder, screen-printed SnO$_2$ sensor and SiOC-coated SnO$_2$ sensor were performed and the recorded diffraction patterns are plotted in Figure 5.2. XRD patterns of uncoated SnO$_2$ sensor and SiOC-coated SnO$_2$ sensor are found to be identical; SiOC ceramic obtained after pyrolysis at 700 ºC is amorphous in nature (section 4.1.4) as the depth of penetration of x-rays are in the range of several μm.
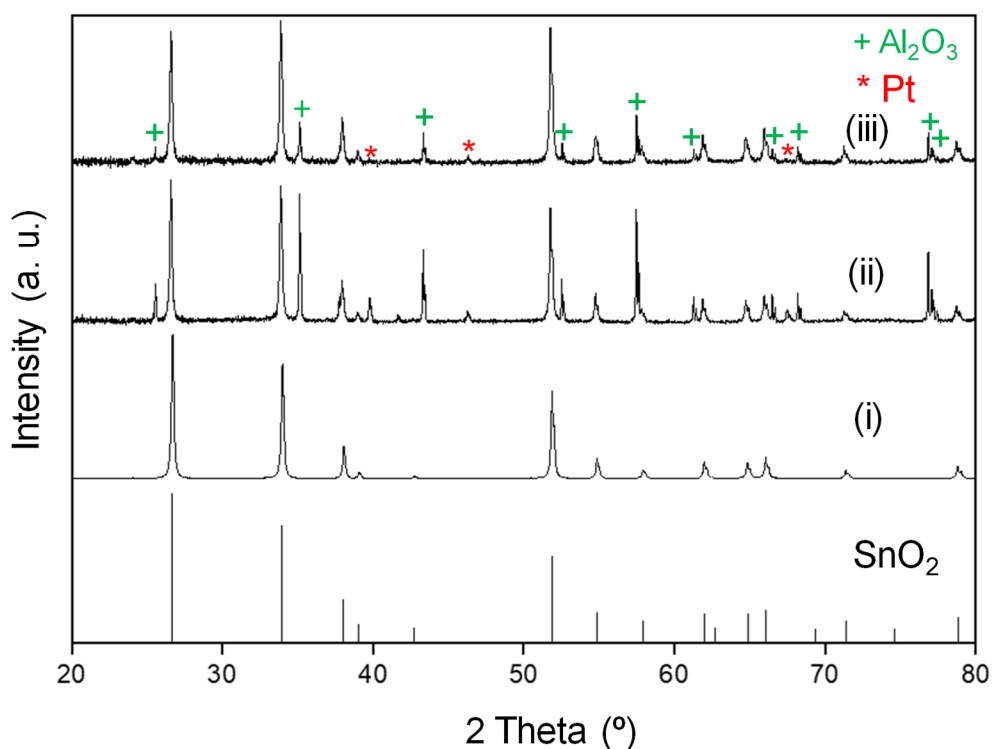
Figure 5.2 X-ray diffraction patterns of: (i) SnO$_2$ powder, (ii) screen-printed SnO$_2$ sensor, and (iii) SiOC-coated SnO$_2$ sensor. The diffraction pattern of reference SnO$_2$ (ICSD PDF Code: 01-072-1147, Tetragonal) is shown at the bottom. Al$_2$O$_3$ and Pt reflections are due to sensor substrate and electrode.

The peak positions of SnO_2 powder, SnO_2 sensor and SiOC-coated SnO_2 sensor at 26.61º, 33.92°, 37.99º, 39.02°, 42.68º, 51.83°, 54.81°, 57.92°, 61.94º, 62.68°, 64.84º, 66.04°, 69.32º, 71.39°, 74.56º, and 78.80° are well matched with reference standard SnO_2 (ICSD PDF code: 01-072-1147, Tetragonal) indicating chemical stability of SnO_2 layer on sensor substrate after coating with SiOC ceramic using polymer-pyrolysis route. The appearance of peaks corresponding Al_2O_3 and Pt in the sensors are due to presence of Al_2O_3 (base substrate) and Pt (as electrode) in the sensor substrate, as discussed in section 2.1.

To further verify coating of SiOC on SnO_2 sensor, Raman spectroscopy study of SnO_2 sensor and SiOC-coated SnO_2 sensor was done. The Raman shifts of screen-printed uncoated SnO_2 gas sensor are observed at 474 cm^{-1}, 633 cm^{-1}, and 775 cm^{-1} showed the typical feature of the rutile phase [134]; however, for two-times SiOC-coated SnO_2 gas sensor the Raman shift of SnO_2 is absent due to uniform coating of amorphous SiOC ceramic layer on screen-printed SnO_2 sensing layer which suppresses the Raman active peaks of SnO_2.
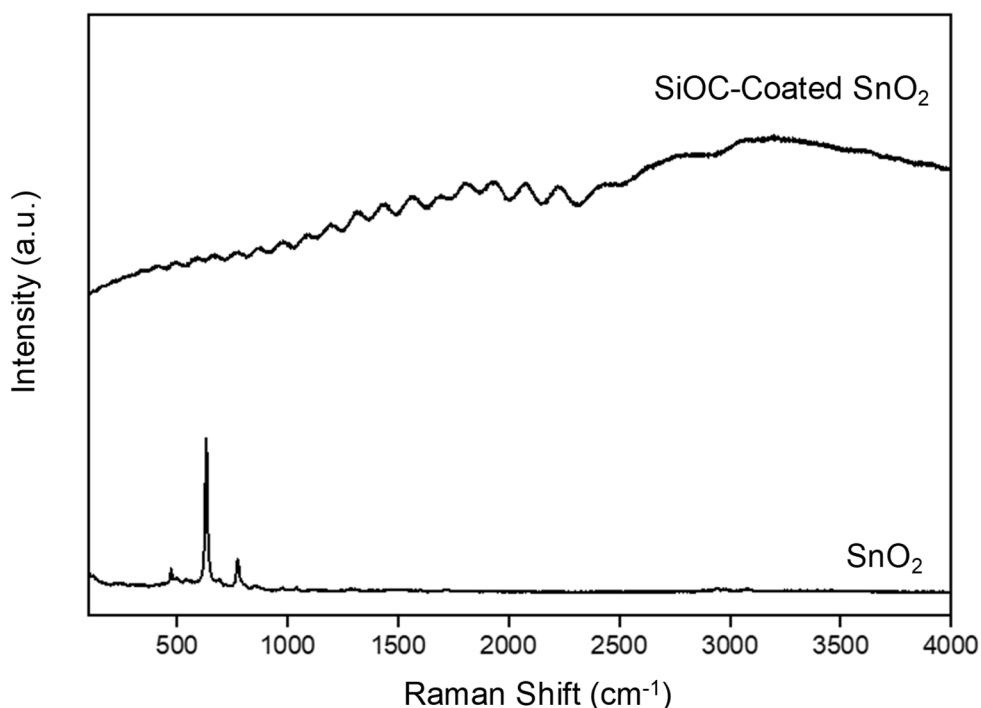
Figure 5.3 Raman spectra of SnO_2 sensor and SiOC-coated SnO_2 sensor.

5.1.2 Gas sensing performance of uncoated SnO$_2$ sensor and SiOC-coated SnO$_2$ sensor

Gas sensing performance SnO$_2$ sensor and SiOC-coated SnO$_2$ sensor were measured towards H$_2$ (50, 500, 1000 ppm) and CO (50, 70, 100 ppm) at 400 °C. H$_2$ (kinetic diameter of 2.89 Å) and CO (kinetic diameter of 3.76 Å) gases diffuses through microporous SiOC filter layer towards SnO$_2$ sensing layer, however, SiOC layer acts as a barrier for the diffusion of gases due to difference in kinetic diameter of H$_2$ and CO. Detailed gas transport mechanism of gases through SiOC layer is discussed in section 5.3.

Reversible resistance changes towards H$_2$ and CO are observed for all sensors indicating stability of sensors under the sensing measurement conditions (gas concentration and temperature). The transient sensing response (Figure 5.4 and Figure 5.5) of uncoated SnO$_2$ and SiOC-coated SnO$_2$ sensors to H$_2$ and CO is significantly distinct. Response and recovery time towards CO sensing are significantly slower and longer for SiOC-coated sensors compared to uncoated SnO$_2$ sensors; response/recovery time towards 100 ppm CO are around 59 s/346 s (SnO$_2$ sensor) and 867 s/1347 s (SiOC-coated SnO$_2$ sensor). Whereas towards H$_2$ sensing, not significant difference in response and recovery time are observed for uncoated and SiOC-coated sensors; response/recovery time towards 1000 ppm H$_2$ are 82 s/5842 s (SnO2 sensor) and 179 s/4176 s (SiOC-coated SnO$_2$ sensor). It can be observed that response time of SiOC-coated SnO$_2$ is higher compared to uncoated SnO$_2$ sensor as the SiOC layer acts as a barrier for the diffusion of gases towards sensing layer. Moreover, a larger increase in response time can be found towards CO sensing (~15-fold increase) compared to H$_2$ (2-fold increase) SiOC-coated sensor compared to uncoated sensor.
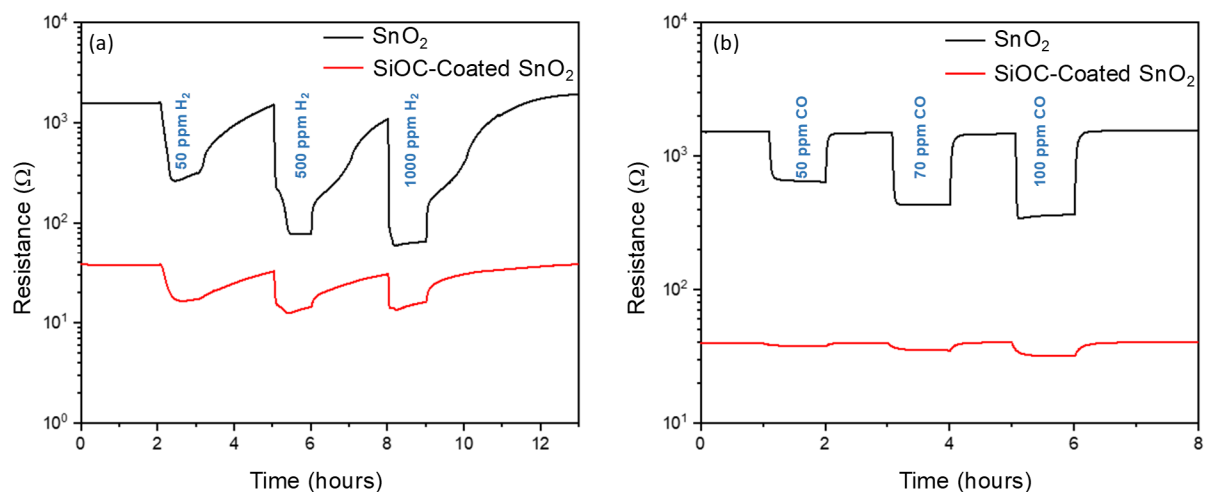
Figure 5.4 Transient response of screen-printed uncoated SnO$_2$ sensor and SiOC-coated SnO$_2$ sensor at 400 °C: (a) under H$_2$ concentrations (50, 500, 1000 ppm in nitrogen), and (b) under CO concentrations (50, 70, 100 ppm in nitrogen).
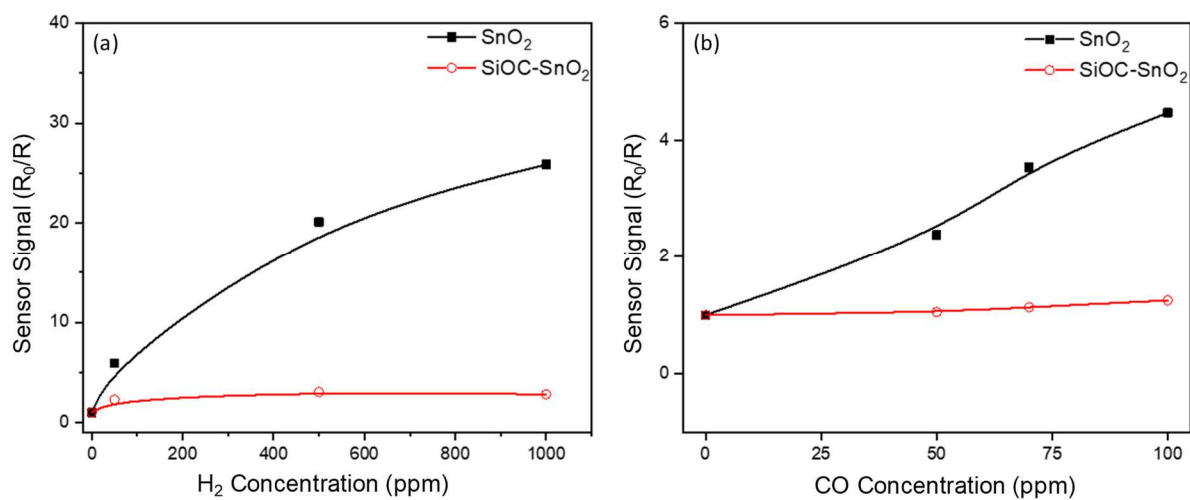
Figure 5.5 Sensor signal (R$_o$/R) for uncoated SnO$_2$ sensor and SiOC-coated SnO$_2$ sensor at 400 °C: (a) H$_2$ (50-1000 ppm), (b) CO (50-100 ppm); R$_o$ is baseline resistance in N$_2$ and R is the resistance during target gas exposure (CO in N$_2$).

5.2   SiOC-coated GaN sensors

5.2.1 Structural characterization of uncoated GaN sensor and SiOC-coated GaN sensor

Screen-printed GaN sensor was coated with a crack-free a SiOC filter layer, with a thickness of about 6 µm, achieved through a two-fold coating/pyrolysis process (as depicted in Figure 5.6 a-c). EDS elemental mapping validates the presence of elements Si, O, and C in the SiOC layer (Figure 5.6 d-f), while presence of elements Ga and N is confirmed in the GaN sensing layer (Figure 5.6 g-h).
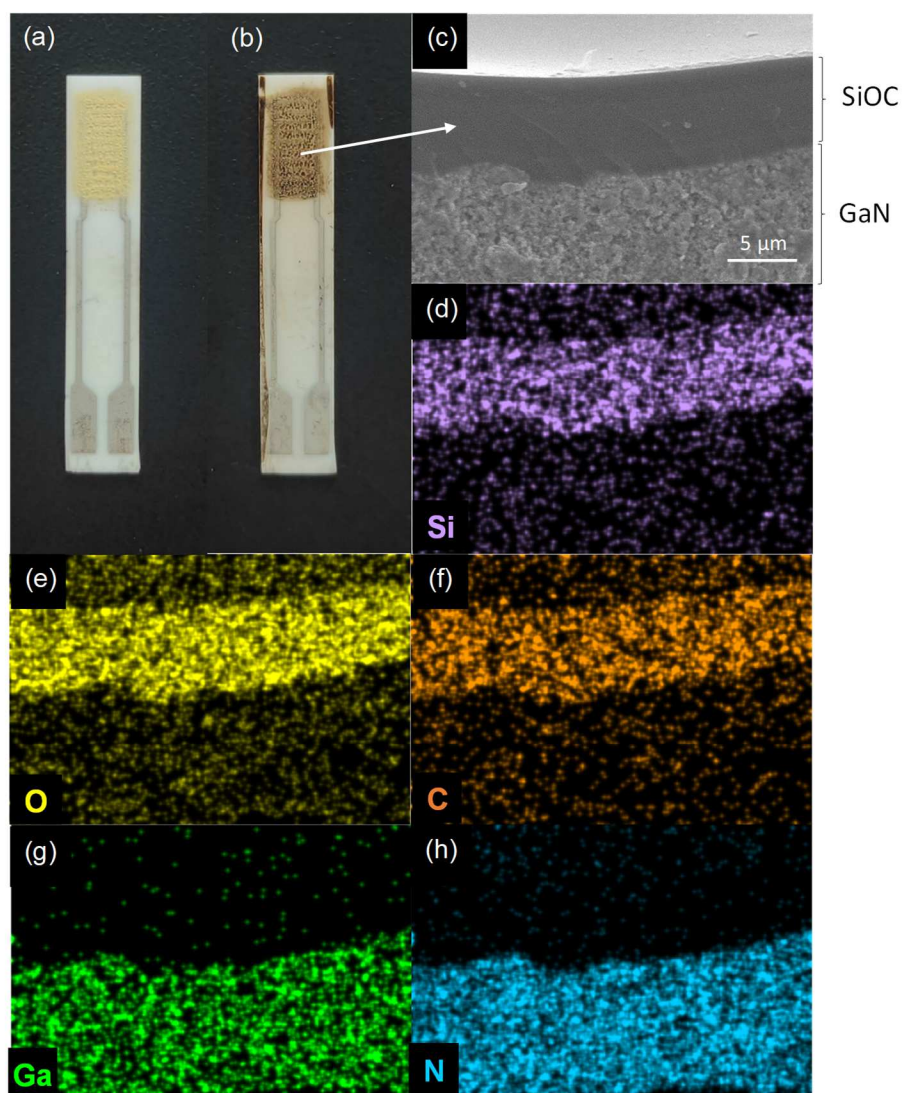
Figure 5.6 Digital images of: (a) screen printed GaN sensor, (b) two-fold SiOC-coated GaN sensor; (c) SEM image of fractured cross-section of SiOC-coated GaN sensor. EDS elemental mapping images of elements: (d) Silicon, (e) Oxygen, (f) Carbon, (g) Gallium, and (h) Nitrogen.

X-ray diffraction (XRD) patterns of GaN sensor and SiOC-coated GaN sensor, as shown in Figure 5.7, exhibit no significant difference due to presence of thin amorphous SiOC layer on GaN. When comparing the XRD diffraction patterns, the peak positions of both sensors measured at 32.41°, 34.63°, 36.88°, 48.17°, 57.83°, 63.54°, 67.88°, 69.19°, 70.60°, 73.06°, and 78.50° are matched with the standard GaN (ICSD PDF Code: 01–074–0243). It should be noted that the presence of reflections corresponding to Al_2O_3 and Pt in the GaN sensor and SiOC-coated GaN sensor is attributed to the sensor substrate and electrodes. To verify the coating of SiOC layer on GaN sensor, a comparative Raman spectroscopy study was conducted. In Figure 5.8, the Raman shift of the screen-printed GaN sensor is observed at 420 cm^{-1}, 569 cm^{-1}, and 730 cm^{-1}. The peaks at 569 cm^{-1} and 730 cm^{-1} represent the TO (transverse optical) and LO (longitudinal optical) vibrational density of states of GaN, respectively; the peak at 420 cm^{-1} indicates the formation of a Ga-N$_6$ bond in GaN, in agreement with reference [135]. Notably, the SiOC-coated GaN sensor does not exhibit the Raman active peaks of GaN, as shown in Figure 8. Absence of GaN peaks confirms proper coating of amorphous polymer-derived SiOC ceramic on the GaN sensor.
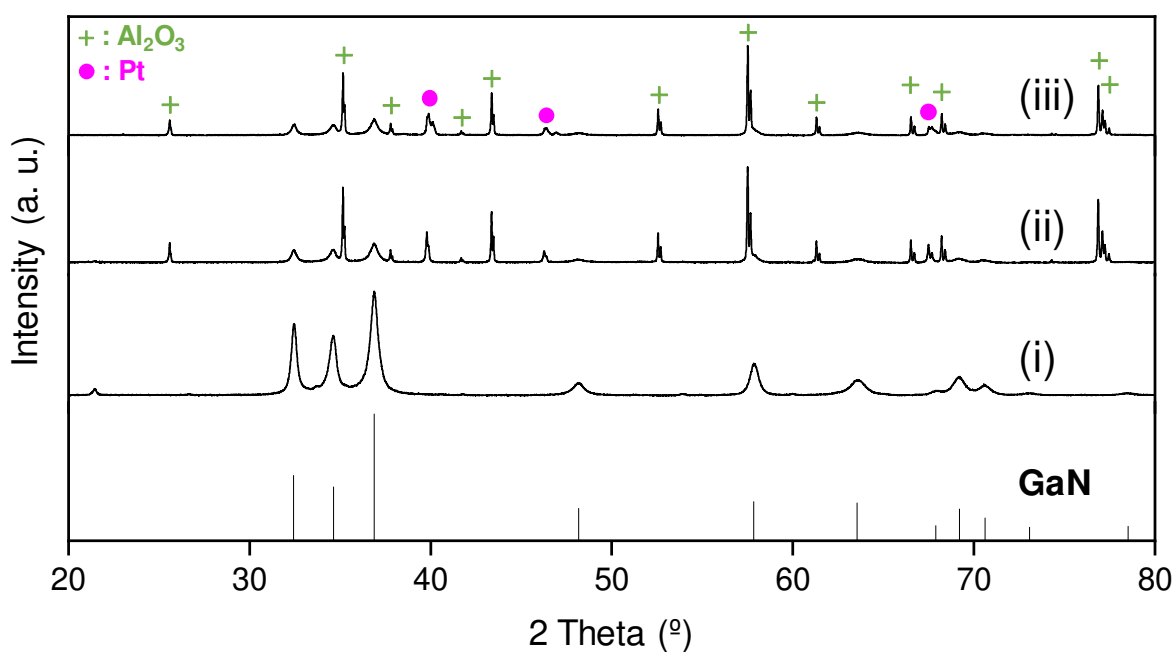
Figure 5.7 XRD patterns of: (i) GaN powder, (ii) screen-printed GaN sensor, and (iii) SiOC-coated GaN sensor. The diffraction pattern of reference GaN (ICSD PDF Code: 01-074-0243, Hexagonal) is shown at the bottom. Al_2O_3 and Pt reflections are due to sensor substrate and electrodes.
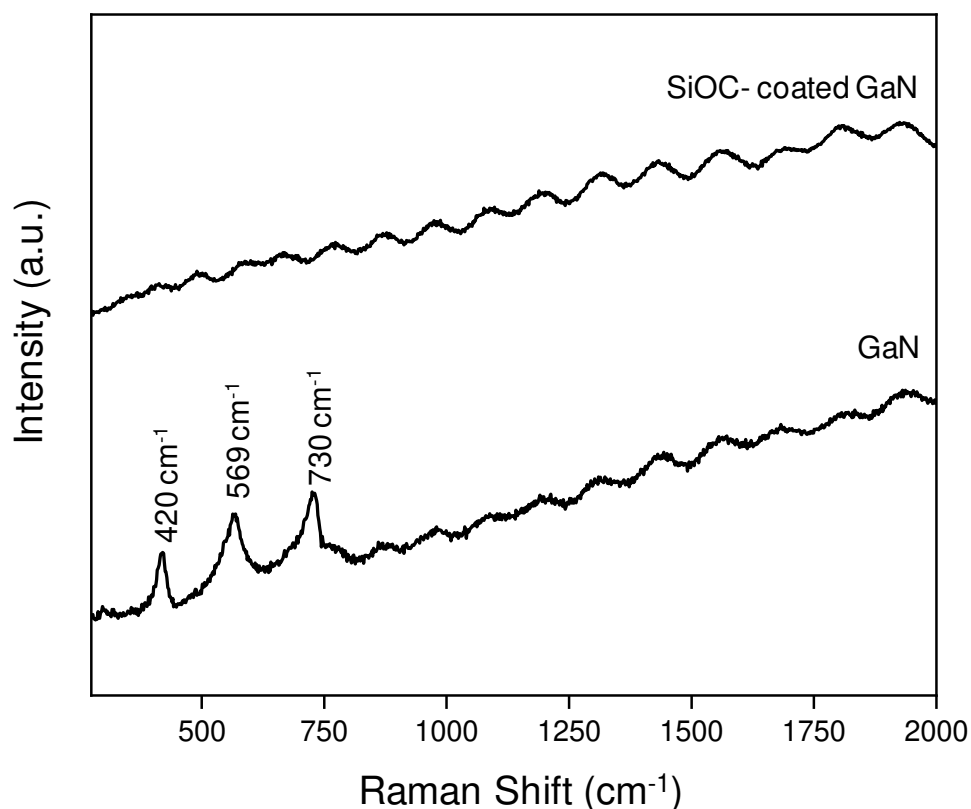
Figure 5.8 Raman shift of screen-printed GaN sensor and SiOC-coated GaN sensor.

5.2.2 Gas sensing performance of uncoated GaN sensor and SiOC-coated GaN sensor

Gas sensing properties of GaN and two-fold SiOC-coated GaN sensors were studied towards different H_2 (50–1000 ppm) and CO (50–100 ppm) concentrations at 400 °C, Figure 5.9 (a, b). Reversible DC resistance changes towards H_2 and CO are observed for both sensors. A significant difference is observed between sensor response towards H_2 and CO for uncoated GaN and SiOC-coated GaN sensors. SiOC-coated sensors show relatively slow response and larger recovery times towards CO sensing compared to uncoated GaN sensors, however, the response and recovery times towards H_2 sensing did not show significant change. A dramatic decrease in response towards CO sensing (almost negligible CO sensing) was observed for SiOC-coated sensors compared to uncoated GaN sensors (Figure 5.9 a). The response/recovery time towards 100 ppm CO are around 92 s/120 s (GaN sensor) and 1364 s/788 s (SiOC-coated GaN sensor); whereas response/recovery time towards 1000 ppm H_2 are 72 s/7878 s (GaN sensor) and 190 s/7170 s (SiOC-coated GaN sensor). Larger increase in response time is found towards CO sensing (~15 fold increase)

compared to H_2 (~2.5-fold increase). These measurements confirm that response time of SiOC-coated GaN is higher compared to uncoated GaN sensor as the SiOC layer acts as a barrier for the diffusion of gases towards GaN sensing layer. This indicates significantly lower diffusion of CO through SiOC layer compared to that of H_2 diffusion towards sensing layer.
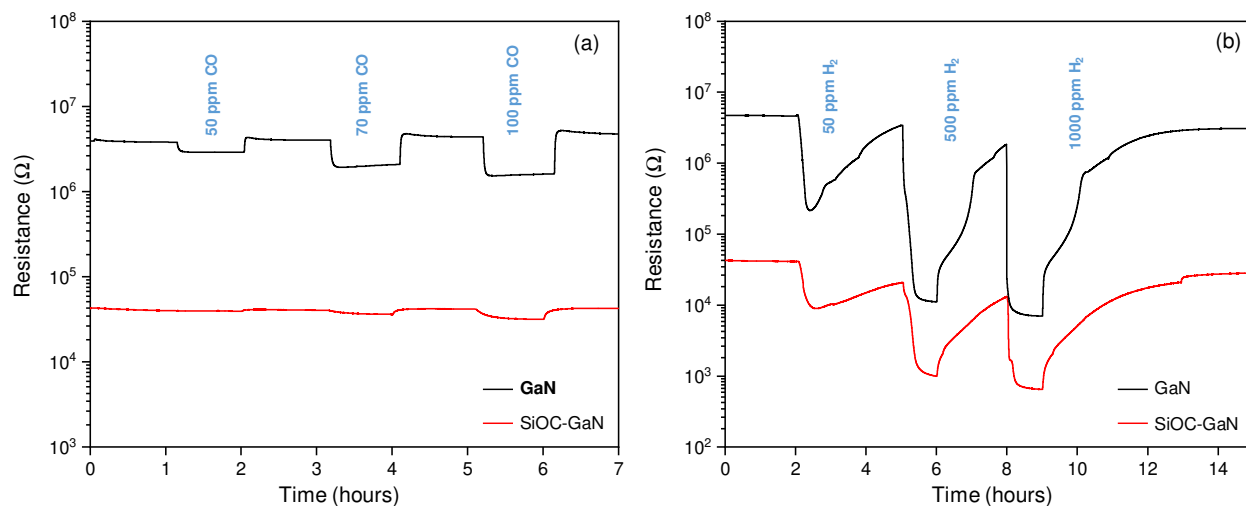
Figure 5.9 Transient response of screen-printed GaN and SiOC-coated GaN sensors at 400°C: (a) under CO concentrations (50, 70, 100 ppm in nitrogen), and (b) under H_2 concentrations (50, 500, 1000 ppm in nitrogen).
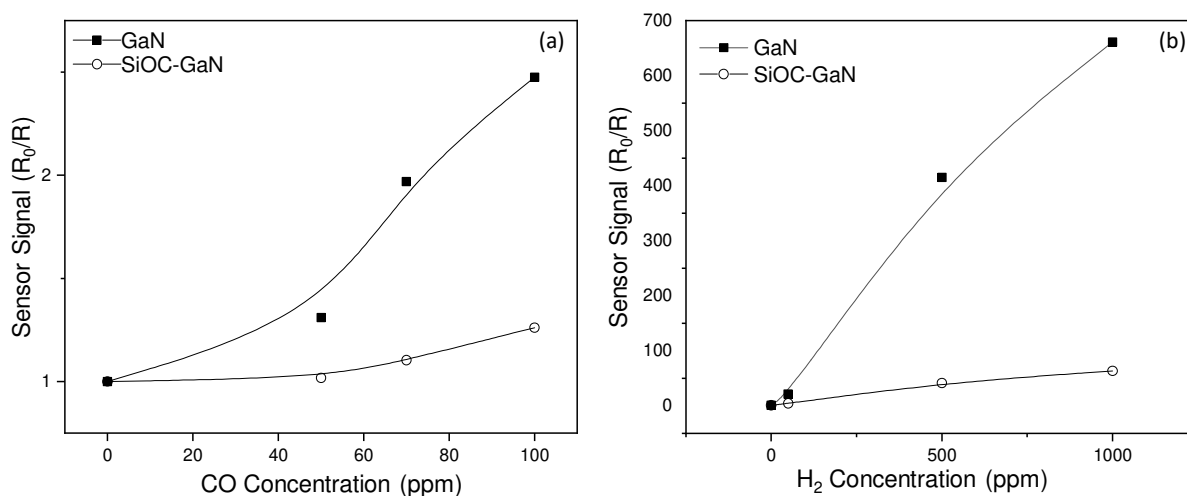
Figure 5.10 Sensor signal (R_o/R) for uncoated GaN sensor and SiOC-coated GaN Sensor at 400 °C: (a) CO (50-100 ppm), (b) H_2 (50-1000); R_o is baseline resistance in N_2 and R is the resistance during target gas exposure (CO in N_2).

5.3 Mechanism of transport of H_2 and CO through amorphous SiOC filter towards sensing layer

In this section, a proposed model of diffusion of H_2 and CO through amorphous SiOC filter layer coated on gas sensors is discussed and presented. Prasad et al. [136] studied gas permeance measurements of SiOC-coated γ-Al_2O_3/α-Al_2O_3 tubular membranes and showed that permeance of H_2 (kinetic diameter of 2.89 Å) increases with the increase in measurement temperatures, where as that of larger gas molecules (CO_2 (kinetic diameter: 3.3 Å), N_2 (kinetic diameter: 3.64 Å)) decreases. H_2 follows solid-state diffusion mechanism [137] with a larger vibration frequency and lower activation energy of H_2; whereas larger molecules such as CO_2, N_2, etc., follows gas-translational mechanism [137] – a combination of Knudsen diffusion and surface diffusion also called as activated Knudsen diffusion mechanism – due to size effect. Solid-state diffusion occurs when pore-size of the membrane is very small (and membrane behaves as a dense material) where interaction of gas molecules with pore-wall of membrane becomes stronger and therefore the solubility of gas with the membrane material plays an important role; permeating gas molecules reside in the solubility sites as well as are in equilibrium with the surrounding gas molecules. In Knudsen diffusion [137], gas molecule collides frequently with the pore wall than with other diffusing gas molecules and gas permeance of a particular molecule decreases with the increase in temperature. Surface diffusion [137] generally occurs at low temperature, when the interaction between the gas molecules and the pore-wall surface gets stronger compared to the kinetic energy of gas molecules and therefore they cannot escape from the surface potential fields of the pore-wall.

Polymeric precursor (vinyl-functionalized polysiloxane) that is used in this thesis work to synthesize SiOC filter was also used in work of Prasad et al. [136] to study gas permeance characterization of SiOC-coated γ-Al_2O_3/α-Al_2O_3 based tubular membranes. Therefore, it is logically coherent to suggest that gas permeance of relatively larger CO molecules (kinetic diameter of 3.76 Å) through the SiOC-coated sensors decreases at higher temperature compared to activated transport of H_2. A model representing gas transport through SiOC-coated sensor is shown in Figure 5.11. Some micropore channel (pore diameter ~4.6 Å, as confirmed by nitrogen-adsorption measurements, section 4.1.5) may have formed by interconnection of several micropores acting as 'defects', herein the gas flows gas-translational diffusion, which allows

diffusion of both smaller H_2 and relatively larger CO gas molecules. The lower value of time response towards H_2 indicating higher gas selectivity of H_2 compared to CO indicates the presence of pores of diameter of about 3 Å ─ which cannot be detected by N_2-adsorption method ─ in microporous amorphous SiOC network through which solid-state diffusion of H_2 occurs. Accordingly, the H_2 and CO gas selectivity of SiOC-coated sensors could be explained taking into account the contribution of both mechanisms. Hence, significantly reduced sensing response towards CO for SiOC-coated sensors compared to uncoated sensors is observed (Figures 5.9 and 5.10). The sensor signal (R_o/R) shown in the Figure 5.5 and Figure 5.10 confirms that SiOC-coated sensors offers very low sensing response to carbon monoxide (CO), whereas screen-printed uncoated sensors show high sensing response for both CO and H_2.
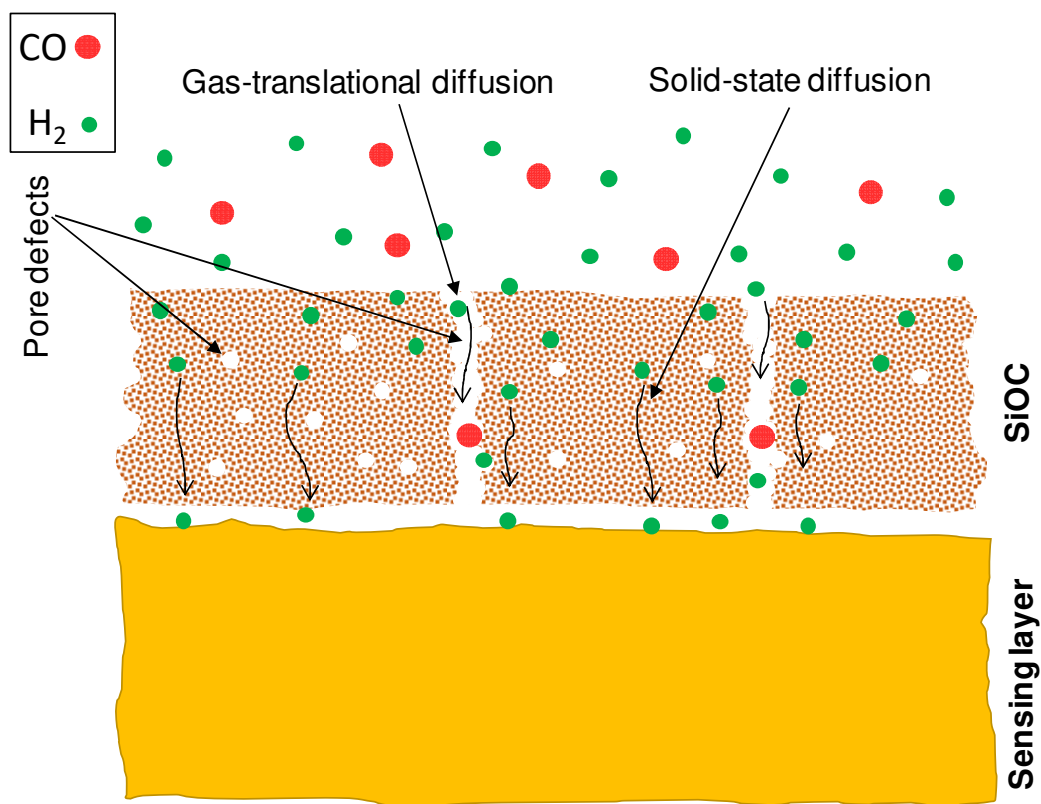

Figure 5.11 A model representing mechanism of transport of H_2 and CO through amorphous SiOC filter towards sensing layer.

Chapter 6. Conclusions and outlook

In this thesis work, enhancement of H_2/CO sensing selectivity of gas sensors coated with amorphous microporous polymer-derived ceramic filter layers has been studied. Three different classes of ceramics (SiOC, SiCN and SiC) have been synthesized and characterized. Microporous ceramics are coated on planar gas sensors using dip-coating method. Gas sensing performance of uncoated and ceramic-coated gas sensors are measured. Potential application of microporous ceramic coated gas sensors with enhanced selectivity of H_2 with respect to CO is explored under harsh reducing conditions (oxygen free conditions).

In the first step, laboratory-scale gas sensing experimental set-up has been designed and realized. It consists of mass flow controllers, multi gas controller, multimeters, power source, and gas sensing chamber; experimental set-up is operated by a LabVIEW program developed indigenously.The experimental set-up is capable of measuring gas sensing characteristics from room temperature to 500 °C under oxygen-free conditions. Planar sensor substrates ─ have been used in this work for coating of sensing material ─ consisting of planar Al_2O_3 substrate with interdigited Pt-electrodes on the front side for measuring resistance and a Pt-heater on the backside to heat the sensor at the required temperature of sensing measurement. Gas sensing materials have been coated on sensors substrates using RF sputtering method and screen-printing process.

Three pre-ceramic polymers, namely vinyl-functionalized polysiloxane, polysilazane and ally hydrido polycarbosilane, are used for the synthesis of SiOC, SiCN and SiC ceramics, respectively. Structures of the polymers were studied using liquid-state NMR and ATR-IR spectroscopic methods. Thermal analysis of the polymers shows ceramic yields of about 32 %, 65% and 76 % by mass for polysiloxane, polysilazane and polycarbosilane, respectively, obtained at 900 °C under flowing argon. XRD measurements of ceramics prepared at 700 °C, 800 °C and 900 °C showed formation of amorphous ceramics. Pore-size characteristics of the unsupported ceramic powders obtained by pyrolysis of all three polymers at 700 °C, 800 °C, and 900 ºC are evaluated by N_2 physisorption isothermal analysis; however, microporous nature is found only for the ceramics derived from vinyl-functionalized polysiloxane. Therefore, the polysiloxane polymer has been selected for the deposition of microporous SiOC filter layers on SnO_2 and GaN sensors.

SiOC layer with a thickness of about 5-6 µm are coated on screen-printed SnO_2 and GaN sensor substrates after two-fold coating/pyrolysis steps by dip-coating of sensors in polysiloxane solution followed by pyrolysis 700 °C under argon. Gas sensing performances of SiOC-coated SnO_2 sensor and SiOC-coated GaN sensor have been studied at 400 °C for the H_2/CO gas sensing selectivity in harsh reducing conditions wre measured towards H_2 (50, 500, 1000 ppm) and CO (50, 70, 100 ppm). Reversible resistance changes towards H_2 and CO are observed for both sensors. Significant difference is observed between sensor response towards H_2 and CO for uncoated and SiOC-coated sensors. SiOC-coated sensors show relatively slow response and larger recovery times towards CO sensing compared to uncoated sensors, however, the response and recovery times towards H_2 sensing does not show significant change. Almost negligible CO sensing is observed for SiOC-coated sensors compared to uncoated sensors.

Finally, a model for diffusion of H_2 and CO through microporous SiOC filter layer coated on sensors has been proposed. Gas permeance measurements of SiOC-coated γ-Al_2O_3/α-Al_2O_3 tubular membranes by Prasad et al. (reference [137], in chapter 5) showed that permeance of H_2 (kinetic diameter of 2.89 Å) increases with temperatures, where as that of larger gas molecules CO_2 (kinetic diameter: 3.3 Å) decreases. H_2 follows solid-state diffusion mechanism whereas larger molecule CO_2 follows gas-translational mechanism – a combination of Knudsen diffusion and surface diffusion – due to size effect. Therefore, gas permeance of larger molecule CO (kinetic diameter: 3.76 Å) will decrease at higher temperatures compared to that of H_2. Hence, reduced sensing response towards CO for SiOC-coated sensors compared to uncoated sensors is observed.

The experimental results obtained within the framework of the present thesis work allows for the following recommendations for future research work:

i) *Improving the set-up for gas sensing measurements*: The experimental gas sensing set-up realized in this work has a detection limit of up to 10 ppm. By using mass flow controllers of lower flow rates, this limit can be lowered for detecting H_2 and CO in the range of ppb.

ii) *Exploring the mechanism of gas detection*: As demonstrated in the present work that uncoated sensors show high sensor signals towards both H_2 and CO and almost no sensing signals to CO for SiOC-coated sensors. The difference in the H_2 and CO sensing mechanisms of uncoated- and SiOC-coated sensors needs to be studied under operando

conditions using surface specific spectroscopic techniques like Diffuse Reflectance Infrared Fourier Transform (DRIFT) spectroscopy.

iii) *Improving membrane-sensor integration*: In the present work, the membrane-sensor integration is achieved by the coating of microporous ceramic layer on the top of screen-printed planar sensors. Further studies can be done for slightly modified filter-sensor integration system by introducing an intermediate mesoporous layer between the microporous ceramic layer and the gas sensing layer. A sharp thickness gradient between the sensing layer and the sensor support, due to the thickness (~ 30-50 μm) of the sensing layer, exists at the edges of a screen-printed sensing layer which can result in cracks within the membrane layer. Therefore, an intermediate mesoporous layer can provide a smooth porous surface between the sensing layer and the top microporous ceramic coating and hence eliminate in this way the crack formation.

iv) *Testing under humid conditions*: Sensing of H_2 and CO under moisture (relative humidity) conditions can be conducted in future.

References

[1] T. Hübert, L. Boon-Brett, G. Black, U. Banach, Hydrogen sensors – A review, Sensors and Actuators B: Chemical, 157 (2011) 329-52.

[2] H. Nazemi, A. Joseph, J. Park, A. Emadi, Advanced micro-and nano-gas sensor technology: A review, Sensors, 19 (2019) 1285.

[3] D.K. Aswal, S.K. Gupta, Science and technology of chemiresistor gas sensors: Nova Publishers; 2007.

[4] A. Gurlo, N. Bârsan, U. Weimar, Gas sensors based on semiconducting metal oxides, Metal oxides, CRC press2005, pp. 705-60.

[5] Z.P. Tshabalala, D.N. Oosthuizen, H.C. Swart, D.E. Motaung, Chapter 5 - Tools and techniques for characterization and evaluation of nanosensors, in: B. Han, V.K. Tomer, T.A. Nguyen, A. Farmani, P. Kumar Singh (Eds.), Nanosensors for Smart Cities, Elsevier 2020, pp. 85-110.

[6] T. Aldhafeeri, M.-K. Tran, R. Vrolyk, M. Pope, M. Fowler, A review of methane gas detection sensors: Recent developments and future perspectives, Inventions, 5 (2020) 28.

[7] O.A.M. Popoola, G.B. Stewart, M.I. Mead, R.L. Jones, Development of a baseline-temperature correction methodology for electrochemical sensors and its implications for long-term stability, Atmospheric Environment, 147 (2016) 330-43.

[8] A. Petculescu, B. Hall, R. Fraenzle, S. Phillips, R.M. Lueptow, A prototype acoustic gas sensor based on attenuation, The Journal of the Acoustical Society of America, 120 (2006) 1779-82.

[9] J.G. Firth, A. Jones, T.A. Jones, The principles of the detection of flammable atmospheres by catalytic devices, Combustion and Flame, 20 (1973) 303-11.

[10] P.T. Moseley, B.C. Tofield, Solid state gas sensors, Bristol: Adam Hilger; 1987.

[11] L. Xu, T. Li, X. Gao, Y. Wang, A high heating efficiency two-beam microhotplate for catalytic gas sensors, 2012 7th IEEE International Conference on Nano/Micro Engineered and Molecular Systems (NEMS), IEEE 2012, pp. 65-8.

[12] W.H. Brattain, J. Bardeen, Surface properties of germanium, The Bell System Technical Journal, 32 (1953) 1-41.

[13] T. Seiyama, A. Kato, K. Fujiishi, M. Nagatani, A new detector for gaseous components using semiconductive thin films, Analytical Chemistry, 34 (1962) 1502-3.

[14] M. de la L. Olvera, R. Asomoza, SnO_2 and SnO_2:Pt thin films used as gas sensors, Sensors and Actuators B: Chemical, 45 (1997) 49-53.

[15] A. Dey, Semiconductor metal oxide gas sensors: A review, Materials Science and Engineering: B, 229 (2018) 206-17.

[16] K. Dieter, Function and applications of gas sensors, Journal of Physics D: Applied Physics, 34 (2001) R125.

[17] F. Yun, S. Chevtchenko, Y.-T. Moon, H. Morkoç, T.J. Fawcett, J.T. Wolan, GaN resistive hydrogen gas sensors, Applied Physics Letters, 87 (2005).

[18] C.-Y. Chang, G.-C. Chi, W.-M. Wang, L.-C. Chen, K.-H. Chen, F. Ren, et al., Electrical transport properties of single GaN and InN nanowires, Journal of electronic materials, 35 (2006) 738-43.

[19] G. Koley, Z. Cai, InN nanowire based sensors, SENSORS, IEEE 2008, pp. 118-21.

[20] M. Kerlau, O. Merdrignac-Conanec, P. Reichel, N. Bârsan, U. Weimar, Preparation and characterization of gallium (oxy)nitride powders: Preliminary investigation as new gas sensor materials, Sensors and Actuators B: Chemical, 115 (2006) 4-11.

[21] A. Gurlo, Interplay between O_2 and SnO_2: Oxygen Ionosorption and Spectroscopic Evidence for Adsorbed Oxygen, ChemPhysChem, 7(2006) 2041-52.

[22] A. Gurlo, R. Riedel, In situ and operando spectroscopy for assessing mechanisms of gas sensing, Angewandte Chemie International Edition, 46 (2007) 3826-48.

[23] N. Barsan, U. Weimar, Conduction Model of Metal Oxide Gas Sensors, Journal of Electroceramics, 7 (2001) 143-67.

[24] K. Ihokura, J. Watson, The stannic oxide gas sensorprinciples and applications: CRC press; 2017.

[25] N. Bârsan, U. Weimar, Understanding the fundamental principles of metal oxide based gas sensors; the example of CO sensing with SnO_2 sensors in the presence of humidity, Journal of Physics: Condensed Matter, 15(2003) R813.

[26] S.R. Morrison, Selectivity in semiconductor gas sensors, Sensors and Actuators, 12 (1987) 425-40.

[27] B. Yang, Z. Zhang, C. Tian, W. Yuan, Z. Hua, S. Fan, et al., Selective detection of methane by HZSM-5 zeolite/Pd-SnO_2 gas sensors, Sensors and Actuators B: Chemical, 321 (2020) 128567.

[28] I. Kocemba, T. Paryjczak, Metal films on a SnO_2 surface as selective gas sensors, Thin Solid Films, 272 (1996) 15-7.

[29] C. Imawan, H. Steffes, F. Solzbacher, E. Obermeier, Structural and gas-sensing properties of V_2O_5–MoO_3 thin films for H_2 detection, Sensors and Actuators B: Chemical, 77 (2001) 346-51.

[30] K. Fukui, S. Nishida, CO gas sensor based on Au–La_2O_3 added SnO_2 ceramics with siliceous zeolite coat, Sensors and Actuators B: Chemical, 45 (1997) 101-6.

[31] K. Sahner, R. Moos, M. Matam, J.J. Tunney, M. Post, Hydrocarbon sensing with thick and thin film p-type conducting perovskite materials, Sensors and Actuators B: Chemical, 108 (2005) 102-12.

[32] S. Kitsukawa, H. Nakagawa, K. Fukuda, S. Asakura, T. Shigemori, S. Takahashi, Elimination of Alcohol Interference for a CO Sensor by Catalytic Filter, Denki Kagaku oyobi Kogyo Butsuri Kagaku, 66 (1998) 651-3.

[33] J. Kneer, A. Eberhardt, P. Walden, A. Ortiz Pérez, J. Wöllenstein, S. Palzer, Apparatus to characterize gas sensor response under real-world conditions in the lab, Review of Scientific Instruments, 85 (2014).

[34] M. Fleischer, H. Meixner, Selectivity in high-temperature operated semiconductor gas-sensors, Sensors and Actuators B: Chemical, 52 (1998) 179-87.

[35] G. Tournier, C. Pijolat, Selective filter for SnO_2-based gas sensor: application to hydrogen trace detection, Sensors and Actuators B: Chemical, 106 (2005) 553-62.

[36] C.H. Kwon, D.H. Yun, H.-K. Hong, S.-R. Kim, K. Lee, H.Y. Lim, et al., Multi-layered thick-film gas sensor array for selective sensing by catalytic filtering technology, Sensors and Actuators B: Chemical, 65 (2000) 327-30.

[37] A. Cabot, J. Arbiol, A. Cornet, J.R. Morante, F. Chen, M. Liu, Mesoporous catalytic filters for semiconductor gas sensors, Thin Solid Films, 436 (2003) 64-9.

[38] O. Hugon, M. Sauvan, P. Benech, C. Pijolat, F. Lefebvre, Gas separation with a zeolite filter, application to the selectivity enhancement of chemical sensors, Sensors and Actuators B: Chemical, 67 (2000) 235-43.

[39] M. Schweizer-Berberich, S. Strathmann, U. Weimar, R. Sharma, A. Seube, A. Peyre-Lavigne, et al., Strategies to avoid VOC cross-sensitivity of SnO_2-based CO sensors, Sensors and Actuators B: Chemical, 58 (1999) 318-24.

[40] M. Fleischer, S. Kornely, T. Weh, J. Frank, H. Meixner, Selective gas detection with high-temperature operated metal oxides using catalytic filters, Sensors and Actuators B: Chemical, 69 (2000) 205-10.

[41] J. Hubálek, K. Malysz, J. Prášek, X. Vilanova, P. Ivanov, E. Llobet, et al., Pt-loaded Al_2O_3 catalytic filters for screen-printed WO_3 sensors highly selective to benzene, Sensors and Actuators B: Chemical, 101 (2004) 277-83.

[42] W.A. Bollinger, D.L. Maclean, R.S. Narayan, Separation systems for oil refining and production, Chem. Eng. Prog.; (United States), Vol. 78:10

[43] T.M. Nenoff, R.J. Spontak, C.M. Aberg, Membranes for Hydrogen Purification: An Important Step toward a Hydrogen-Based Economy, MRS Bulletin, 31 (2006) 735-44.

[44] N.W. Ockwig, T.M. Nenoff, Membranes for Hydrogen Separation, Chemical Reviews, 107 (2007) 4078-110.

[45] M. van der Spek, C. Banet, C. Bauer, P. Gabrielli, W. Goldthorpe, M. Mazzotti, et al., Perspective on the hydrogen economy as a pathway to reach net-zero CO2 emissions in Europe, Energy & Environmental Science, 15 (2022) 1034-77.

[46] K.S.W. Sing, Reporting physisorption data for gas/solid systems with special reference to the determination of surface area and porosity (Provisional), Pure and applied chemistry, 54 (1982) 2201-18.

[47] Horv, Aacute, G. Th, Eacute, Za, K. Kawazoe, METHOD FOR THE CALCULATION OF EFFECTIVE PORE SIZE DISTRIBUTION IN MOLECULAR SIEVE CARBON, Journal of Chemical Engineering of Japan, 16 (1983) 470-5.

[48] L.S. Cheng, Y. Ralph T, Improved Horvath—Kawazoe equations including spherical pore models for calculating micropore size distribution, Chemical Engineering Science, 49 (1994) 2599-609.

[49] A. Saito, H. Foley, Curvature and parametric sensitivity in models for adsorption in micropores, AIChE journal, 37 (1991) 429-36.

[50] J. Landers, G.Y. Gor, A.V. Neimark, Density functional theory methods for characterization of porous materials, Colloids and Surfaces A: Physicochemical and Engineering Aspects, 437 (2013) 3-32.

[51] M.V. López-Ramón, J. Jagiełło, T.J. Bandosz, N.A. Seaton, Determination of the Pore Size Distribution and Network Connectivity in Microporous Solids by Adsorption Measurements and Monte Carlo Simulation, Langmuir, 13 (1997) 4435-45.

[52] W. Thomson, 4. On the Equilibrium of Vapour at a Curved Surface of Liquid, Proceedings of the Royal Society of Edinburgh, 7 (1872) 63-8.

[53] E.P. Barrett, L.G. Joyner, P.P. Halenda, The Determination of Pore Volume and Area Distributions in Porous Substances. I. Computations from Nitrogen Isotherms, Journal of the American Chemical Society, 73 (1951) 373-80.

[54] C.A. León y León, New perspectives in mercury porosimetry, Advances in Colloid and Interface Science, 76-77 (1998) 341-72.

[55] A.J. Burggraaf, K. Keizer, Synthesis of Inorganic Membranes, in: R.R. Bhave (Ed.) Inorganic Membranes Synthesis, Characteristics and Applications, Springer Netherlands, Dordrecht, 1991, pp. 10-63.

[56] M. Knudsen, The law of molecular flow and viscosity of gases moving through tubes, Ann Phys, 28 (1909) 75.

[57] M.B. Rao, S. Sircar, Performance and pore characterization of nanoporous carbon membranes for gas separation, Journal of Membrane Science, 110 (1996) 109-18.

[58] R.J.R. Uhlhorn, Ceramic membranes for gas separation: Synthesis and transport properties, Universiteit Twente, (1992).

[59] F. Casanova, C.E. Chiang, C.-P. Li, I.V. Roshchin, A.M. Ruminski, M.J. Sailor, et al., Gas adsorption and capillary condensation in nanoporous alumina films, Nanotechnology, 19 (2008) 315709.

[60] A. Shelekhin, A. Dixon, Y. Ma, Theory of gas diffusion and permeation in inorganic molecular-sieve membranes, AIChE Journal, 41 (1995) 58-67.

[61] R.S.A. de Lange, K. Keizer, A.J. Burggraaf, Analysis and theory of gas transport in microporous sol-gel derived ceramic membranes, Journal of Membrane Science, 104 (1995) 81-100.

[62] J.G. Wijmans, R.W. Baker, The solution-diffusion model: a review, Journal of Membrane Science, 107 (1995) 1-21.

[63] T.L. Ward, T. Dao, Model of hydrogen permeation behavior in palladium membranes, Journal of Membrane Science, 153 (1999) 211-31.

[64] A. Damle, Hydrogen separation and purification, Hydrogen Fuel, CRC Press2008, pp. 295-336.

[65] R.E. Buxbaum, A.B. Kinney, Hydrogen Transport through Tubular Membranes of Palladium-Coated Tantalum and Niobium, Industrial & Engineering Chemistry Research, 35 (1996) 530-7.

[66] H. Wipf, Solubility and diffusion of hydrogen in pure metals and alloys, Physica Scripta, 2001 (2001) 43.

[67] F.A. Lewis, Solubility of hydrogen in metals, Pure and applied chemistry, 62 (1990) 2091-6.

[68] S. Uemiya, Brief Review of Steam Reforming Using a Metal Membrane Reactor, Topics in Catalysis, 29 (2004) 79-84.

[69] P.P. Mardilovich, Y. She, Y.H. Ma, M.-H. Rei, Defect-free palladium membranes on porous stainless-steel support, AIChE Journal, 44 (1998) 310-22.

[70] Y.H. Ma, B.C. Akis, M.E. Ayturk, F. Guazzone, E.E. Engwall, I.P. Mardilovich, Characterization of Intermetallic Diffusion Barrier and Alloy Formation for Pd/Cu and Pd/Ag Porous Stainless Steel Composite Membranes, Industrial & Engineering Chemistry Research, 43 (2004) 2936-45.

[71] M.E. Ayturk, I.P. Mardilovich, E.E. Engwall, Y.H. Ma, Synthesis of composite Pd-porous stainless steel (PSS) membranes with a Pd/Ag intermetallic diffusion barrier, Journal of Membrane Science, 285 (2006) 385-94.

[72] D.S. Sholl, Y.H. Ma, Dense Metal Membranes for the Production of High-Purity Hydrogen, MRS Bulletin, 31 (2006) 770-3.

[73] Y.H. MA, I.P. MARDILOVICH, E.E. ENGWALL, Thin Composite Palladium and Palladium/Alloy Membranes for Hydrogen Separation, Annals of the New York Academy of Sciences, 984 (2003) 346-60.

[74] S. Uemiya, State-of-the-Art of Supported Metal Membranes for Gas Separation, Separation and Purification Methods, 28 (1999) 51-85.

[75] H. Gao, Y.S. Lin, Y. Li, B. Zhang, Chemical Stability and Its Improvement of Palladium-Based Metallic Membranes, Industrial & Engineering Chemistry Research, 43 (2004) 6920-30.

[76] A.J. deRosset, Diffusion of Hydrogen through Palladium Membranes, Industrial & Engineering Chemistry, 52 (1960) 525-8.

[77] S. Uemiya, T. Matsuda, E. Kikuchi, Hydrogen permeable palladium-silver alloy membrane supported on porous ceramics, Journal of Membrane Science, 56 (1991) 315-25.

[78] S. Uemiya, N. Sato, H. Ando, T. Matsuda, E. Kikuchi, Steam reforming of methane in a hydrogen-permeable membrane reactor, Applied Catalysis, 67 (1990) 223-30.

[79] S. Uemiya, Y. Kude, K. Sugino, N. Sato, T. Matsuda, E. Kikuchi, A Palladium/Porous-Glass Composite Membrane for Hydrogen Separation, Chemistry Letters, 17 (2006) 1687-90.

[80] S. Uemiya, N. Sato, H. Ando, Y. Kude, T. Matsuda, E. Kikuchi, Separation of hydrogen through palladium thin film supported on a porous glass tube, Journal of Membrane Science, 56 (1991) 303-13.

[81] A. Darling, The diffusion of hydrogen through palladium, Platinum metals review, 2 (1958) 16-22.

[82] T. Maruno, H. Tsuji, R. Otsuka, Hydrogen embrittlement of Pd-Ag binary alloys, Nippon Kinzoku Gakkaishi, 47 (1983) 768-75.

[83] K.L. Yeung, R. Aravind, J. Szegner, A. Varma, Metal composite membranes: Synthesis, characterization and reaction studies, in: J.W. Hightower, W. Nicholas Delgass, E. Iglesia, A.T. Bell (Eds.), Studies in Surface Science and Catalysis, Elsevier 1996, pp. 1349-58.

[84] J.P. Collins, R.W. Schwartz, R. Sehgal, T.L. Ward, C.J. Brinker, G.P. Hagen, et al., Catalytic Dehydrogenation of Propane in Hydrogen Permselective Membrane Reactors, Industrial & Engineering Chemistry Research, 35 (1996) 4398-405.

[85] H.C. Foley, A.W. Wang, B. Johnson, J.N. Armor, Effect of a Model Hydrogenation on a Catalytic Palladium Membrane, Selectivity in Catalysis, American Chemical Society1993, pp. 168-84.

[86] F. Roa, J.D. Way, R.L. McCormick, S.N. Paglieri, Preparation and characterization of Pd–Cu composite membranes for hydrogen separation, Chemical Engineering Journal, 93 (2003) 11-22.

[87] P. Kamakoti, B.D. Morreale, M.V. Ciocco, B.H. Howard, R.P. Killmeyer, A.V. Cugini, et al., Prediction of Hydrogen Flux Through Sulfur-Tolerant Binary Alloy Membranes, Science, 307 (2005) 569-73.

[88] A.G. Knapton, Palladium alloys for hydrogen diffusion membranes, Platinum Metals Review, 21 (1977) 44-50.

[89] G.Q. Lu, J.C. Diniz da Costa, M. Duke, S. Giessler, R. Socolow, R.H. Williams, et al., Inorganic membranes for hydrogen production and purification: A critical review and perspective, Journal of Colloid and Interface Science, 314 (2007) 589-603.

[90] G. Xomeritakis, Y.-S. Lin, CVD synthesis and gas permeation properties of thin palladium/alumina membranes, AIChE journal, 44 (1998) 174-83.

[91] L.-Q. Wu, N. Xu, J. Shi, Preparation of a Palladium Composite Membrane by an Improved Electroless Plating Technique, Industrial & Engineering Chemistry Research, 39 (2000) 342-8.

[92] K.-S. Chou, S.-M. Wang, Studies on the preparation of Pd/alumina/porous stainless steel membranes for hydrogen separation, Journal of the Chinese Institute of Chemical Engineers, 31 (2000) 499-506.

[93] S.-E. Nam, K.-H. Lee, Hydrogen separation by Pd alloy composite membranes: introduction of diffusion barrier, Journal of Membrane Science, 192 (2001) 177-85.

[94] S.-E. Nam, K.-H. Lee, A study on the palladium/nickel composite membrane by vacuum electrodeposition, Journal of Membrane Science, 170 (2000) 91-9.

[95] H.D. Tong, F.C. Gielens, J.G.E. Gardeniers, H.V. Jansen, C.J.M. van Rijn, M.C. Elwenspoek, et al., Microfabricated Palladium−Silver Alloy Membranes and Their Application in Hydrogen Separation, Industrial & Engineering Chemistry Research, 43 (2004) 4182-7.

[96] N.R. Council, D.o. Engineering, P. Sciences, B.o. Energy, E. Systems, C.o. Alternatives, et al., The hydrogen economy: opportunities, costs, barriers, and R&D needs: National Academies Press; 2004.

[97] S. Kluiters, Status review on membrane systems for hydrogen separation, Energy Center of the Netherlands, Petten, The Netherlands, (2004).

[98] S. Adhikari, S. Fernando, Hydrogen Membrane Separation Techniques, Industrial & Engineering Chemistry Research, 45 (2006) 875-81.

[99] C.J. Orme, M.L. Stone, M.T. Benson, E.S. Peterson, Testing Of Polymer Membranes For The Selective Permeability Of Hydrogen, Separation Science and Technology, 38 (2003) 3225-38.

[100] H. Suzuki, Composite membrane having a surface layer of an ultrathin film of cage-shaped zeolite and processes for production thereof, U.S. Patent No. 4,699,892. 13 Oct. 1987.

[101] J. Dong, Y.S. Lin, M. Kanezashi, Z. Tang, Microporous inorganic membranes for high temperature hydrogen purification, Journal of Applied Physics, 104 (2008).

[102] H. Verweij, Y.S. Lin, J. Dong, Microporous Silica and Zeolite Membranes for Hydrogen Purification, MRS Bulletin, 31 (2006) 756-64.

[103] J. Dong, Y.S. Lin, W. Liu, Multicomponent hydrogen/hydrocarbon separation by MFI-type zeolite membranes, AIChE Journal, 46 (2000) 1957-66.

[104] M. Kanezashi, J. O'Brien-Abraham, Y.S. Lin, K. Suzuki, Gas permeation through DDR-type zeolite membranes at high temperatures, AIChE journal, 54 (2008) 1478-86.

[105] T. Masuda, N. Fukumoto, M. Kitamura, S.R. Mukai, K. Hashimoto, T. Tanaka, et al., Modification of pore size of MFI-type zeolite by catalytic cracking of silane and application to preparation of H2-separating zeolite membrane, Microporous and Mesoporous Materials, 48 (2001) 239-45.

[106] Z. Zheng, A.S. Hall, V.V. Guliants, Synthesis, characterization and modification of DDR membranes grown on α-alumina supports, Journal of Materials Science, 43 (2008) 2499-502.

[107] W. Böcker, H. Landfermann, H. Hausner, Sintering of alpha silicon carbide with additions of aluminium, Powder Met. Int 11(2) (1979), 83–85.

[108] G. Ziegler, J. Heinrich, G. Wötting, Relationships between processing, microstructure and properties of dense and reaction-bonded silicon nitride, Journal of Materials Science, 22 (1987) 3041-86.

[109] R. Riedel, G. Passing, H. Schönfelder, R.J. Brook, Synthesis of dense silicon-based ceramics at low temperatures, Nature, 355 (1992) 714-7.

[110] R. Riedel, A. Kienzle, W. Dressler, L. Ruwisch, J. Bill, F. Aldinger, A silicoboron carbonitride ceramic stable to 2,000°C, Nature, 382 (1996) 796-8.

[111] G. Fritz, B. Raabe, Bildung siliciumorganischer Verbindungen. V. Die Thermische Zersetzung von $Si(CH_3)_4$ und $Si(C_2H_5)_4$, Zeitschrift für anorganische und allgemeine Chemie 286(1956) 149-67.

[112] S. Yajima, J. Hayashi, M. Omori, CONTINUOUS SILICON CARBIDE FIBER OF HIGH TENSILE STRENGTH, Chemistry Letters, 4 (1975) 931-4.

[113] W. Verbeek, Production of shaped articles of homogeneous mixtures of silicon carbide and nitride, U.S. Patent No. 3,853,567. 10 Dec. 1974.

[114] M.D. Mansmann, W.D. Verbeek, G.D. Winter, Formkoerper aus homogenen mischungen von siliciumcarbid und siliciumnitrid und verfahren zu ihrer herstellung, (1974). No. 2243527A.

[115] P. Colombo, G. Mera, R. Riedel, G.D. Sorarù, Polymer-Derived Ceramics: 40 Years of Research and Innovation in Advanced Ceramics, Journal of the American Ceramic Society 93 (2010) 1805-37.

[116] P. Colombo, Polymer derived ceramics: from nano-structure to applications: DEStech Publications, Inc; 2010.

[117] N.S. Choong Kwet Yive, R.J.P. Corriu, D. Leclercq, P.H. Mutin, A. Vioux, Silicon carbonitride from polymeric precursors: thermal cross-linking and pyrolysis of oligosilazane model compounds, Chemistry of Materials, 4 (1992) 141-6.

[118] B. Sørensen, Hydrogen and Fuel Cells: Emerging Technologies and Applications: Elsevier Science; 2011.

[119] I.S. Wieland, I.T. Melin, I.A. Lamm, Membrane reactors for hydrogen production, Chemical Engineering Science, 57 (2002) 1571-6.

[120] B. Kumar, R.M. Prasad, Polymer-derived microporous SiOC ceramic coated gallium nitride sensor for selective H_2/CO detection, Sensors and Actuators B: Chemical, 379 (2023) 133226.

[121] S. Brunauer, P.H. Emmett, E. Teller, Adsorption of Gases in Multimolecular Layers, Journal of the American Chemical Society, 60 (1938) 309-19.

[122] L.P. Deshmukh, T.H. Mujawar, M.S. Kasbe, S.S. Mule, J. Akhtar, N.N. Maldar, A LabVIEW based remote monitoring and controlling of wireless sensor node for LPG gas leakage detection, 2016 International Symposium on Electronics and Smart Devices (ISESD) 2016, pp. 115-20.

[123] J. Chruściel, M. Fejdyś, W. Fortuniak, Synthesis and characterization of new, liquid, branched poly(methylvinylborosiloxanes), e-Polymers, vol. 13, no. 1, 2013, pp. 034.

[124] E. Ionescu, C. Linck, C. Fasel, M. Müller, H.J. Kleebe, R. Riedel, Polymer-Derived SiOC/ZrO_2 Ceramic Nanocomposites with Excellent High-Temperature Stability, Journal of the American Ceramic Society, 93 (2010) 241-50.

[125] D. Su, Y.-L. Li, H.-J. An, X. Liu, F. Hou, J.-Y. Li, et al., Pyrolytic transformation of liquid precursors to shaped bulk ceramics, Journal of the European Ceramic Society, 30 (2010) 1503-11.

[126] J. Wan, M.J. Gasch, A.K. Mukherjee, InSitu Densification Behavior in the Pyrolysis Consolidation of Amorphous Si-N-C Bulk Ceramics from Polymer Precursors, Journal of the American Ceramic Society, 84 (2001) 2165-9.

[127] M. Thommes, K. Kaneko, A.V. Neimark, J.P. Olivier, F. Rodriguez-Reinoso, J. Rouquerol, et al., Physisorption of gases, with special reference to the evaluation of surface area and pore size distribution (IUPAC Technical Report), Pure and applied chemistry, 87 (2015) 1051-69.

[128] M. Hörz, A. Zern, F. Berger, J. Haug, K. Müller, F. Aldinger, et al., Novel polysilazanes as precursors for silicon nitride/silicon carbide composites without "free" carbon, Journal of the European Ceramic Society, 25 (2005) 99-110.

[129] Q.D. Nghiem, J.-K. Jeon, L.-Y. Hong, D.-P. Kim, Polymer derived Si–C–B–N ceramics via hydroboration from borazine derivatives and trivinylcyclotrisilazane, Journal of Organometallic Chemistry, 688 (2003) 27-35.

[130] M.A. Schiavon, G. Domenico Sorarù, I.V.P. Yoshida, Synthesis of a polycyclic silazane network and its evolution to silicon carbonitride glass, Journal of Non-Crystalline Solids, 304 (2002) 76-83.

[131] N.R. Dando, A.J. Perrotta, C. Strohmann, R.M. Stewart, D. Seyferth, Methylhydridopolysilazane and its pyrolytic conversion to silicon nitride-silicon carbide (Si_3N_4/SiC) ceramics, Chemistry of Materials, 5 (1993) 1624-30.

[132] R. Sreeja, B. Swaminathan, A. Painuly, T.V. Sebastian, S. Packirisamy, Allylhydridopolycarbosilane (AHPCS) as matrix resin for C/SiC ceramic matrix composites, Materials Science and Engineering: B, 168 (2010) 204-7.

[133] S. Kaur, R. Riedel, E. Ionescu, Pressureless fabrication of dense monolithic SiC ceramics from a polycarbosilane, Journal of the European Ceramic Society, 34 (2014) 3571-8.

[134] S.H. Sun, G.W. Meng, G.X. Zhang, T. Gao, B.Y. Geng, L.D. Zhang, et al., Raman scattering study of rutile SnO_2 nanobelts synthesized by thermal evaporation of Sn powders, Chemical Physics Letters, 376 (2003) 103-7.

[135] J.Q. Ning, S.J. Xu, D.P. Yu, Y.Y. Shan, S.T. Lee, 418cm−1 Raman scattering from gallium nitride nanowires: Is it a vibration mode of N-rich Ga–N bond configuration?, Applied Physics Letters, 91 (2007).

[136] R.M. Prasad, Y. Jüttke, H. Richter, I. Voigt, R. Riedel, A. Gurlo, Mechanism of Gas Separation through Amorphous Silicon Oxycarbide Membranes, Advanced Engineering Materials, 18 (2016) 721-7.

[137] S.T. Oyama, M. Yamada, T. Sugawara, A. Takagaki, R.J.J.o.t.J.P.I. Kikuchi, Review on mechanisms of gas permeation through inorganic membranes, Journal of the Japan Petroleum Institute, 54 (2011) 298-309.

Annexure I

In this section, structural characterization and gas sensing performance of RF sputtered SnO_2 and SiOC-coated RF sputtered SnO_2 sensors are summarized; Parameters applied for the deposition process of RF sputtered SnO_2 are described in section 2.3.1. Recorded x-ray diffraction patterns of as prepared RF sputtered SnO_2 sensor and RF sputtered SnO_2 sensor calcined at 800 °C are shown in Figure A1. Absence of SnO_2 peaks in the as prepared RF sputtered SnO_2 sensor indicates that as deposited untreated RF sputtered SnO_2 is amorphous whereas the as prepared sensor calcined at 800 °C shows broader peaks − confirming formation of nanocrystalline SnO_2 − compared to screen-printed SnO_2 sensors. The appearance of peaks corresponding Al_2O_3 and Pt in the sensors are due to presence of Al_2O_3 (base substrate) and Pt (as electrode) in the sensor substrate. Raman spectroscopic measurements (Figure A2) also shows Raman shifts corresponding to SnO_2 in case of RF sputtered SnO_2 sensor treated in air at 800 °C.
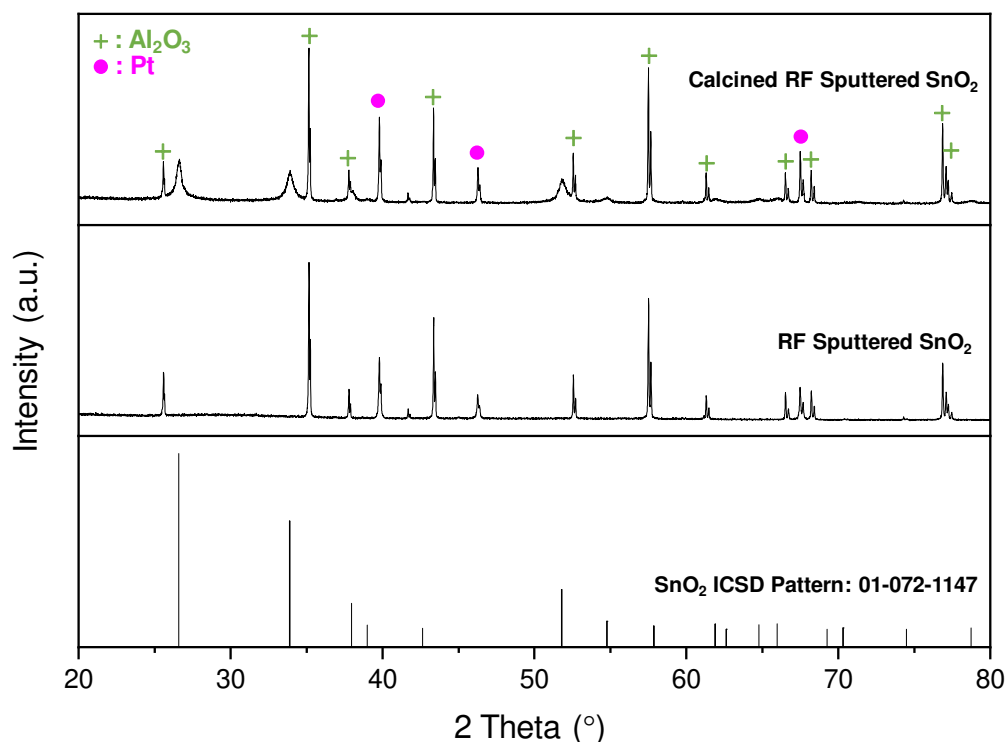

Figure A1. XRD patterns of as prepared RF sputtered SnO_2 sensor and RF sputtered SnO_2 sensor calcined at 800 °C. The diffraction pattern of reference SnO_2 (ICSD PDF Code: 01-072-1147,

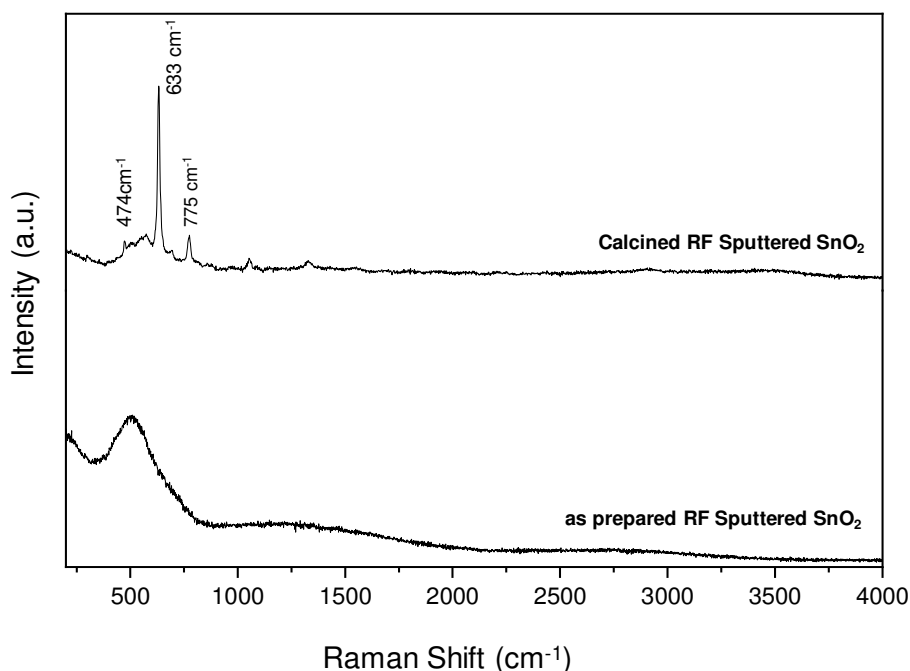Tetragonal) is shown at the bottom. Al_2O_3 and Pt reflections are due to sensor substrate and electrodes.

Figure A2. Raman shift of as prepared RF sputtered SnO_2 sensor and RF sputtered SnO_2 sensor calcined at 800 °C.

Gas sensing properties of calcined RF sputtered SnO_2 and SiOC-coated RF sputtered SnO_2 sensors were studied towards different H_2 (50 ppm, 500 ppm, 1000 ppm) and CO (50 ppm, 70 ppm, 100 ppm) concentrations at 400 °C. Transient response characteristics and sensors signals of the sensors are presented in Figure A3 and Figure A4, respectively. Both sensors show reversible resistance changes towards H_2 and CO exposure. Due to formation of nanocrystalline SnO_2, very fast and high sensing response is measured towards 50 ppm of H_2 and CO. Under H_2 exposure at 500 ppm and 1000 ppm, resistance of SiOC-coated RF sputtered coated sensor are found to be about 9.4 Ω and 9.3 Ω, respectively (Figure A3 d); for calcined RF sputtered sensor the resistance values are measured to be of about 39.2 Ω and 39.1 Ω, respectively (Figure A3 b). This indicates that RF sputtered based SnO_2 sensors get saturated under H_2 under high concentration ranges, therefore, gas sensing characterization measurements using RF sputtered SnO_2 sensors under high H_2 concentration is not accurate under the high H_2 concentration ranges applied in this thesis work.

Similar finding are observed when gas sensing tests were performed at 350 °C as shown in Figure A5 and Figure A6.
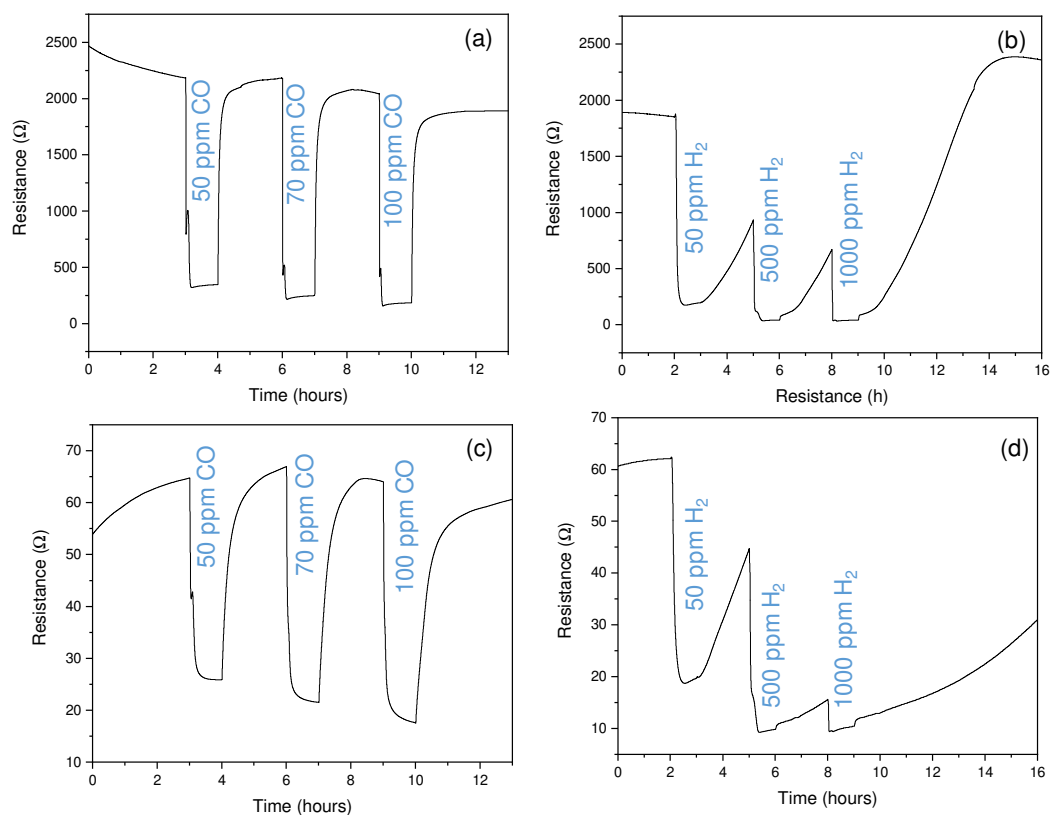

Figure A3. Transient response under CO concentrations (50, 70, 100 ppm in nitrogen), and under H_2 concentrations (50, 500, 1000 ppm in nitrogen) at 400 °C of: calcined RF sputtered coated SnO_2 sensor (a, b) and SiOC-coated calcined RF sputtered SnO_2 sensor (c,d).
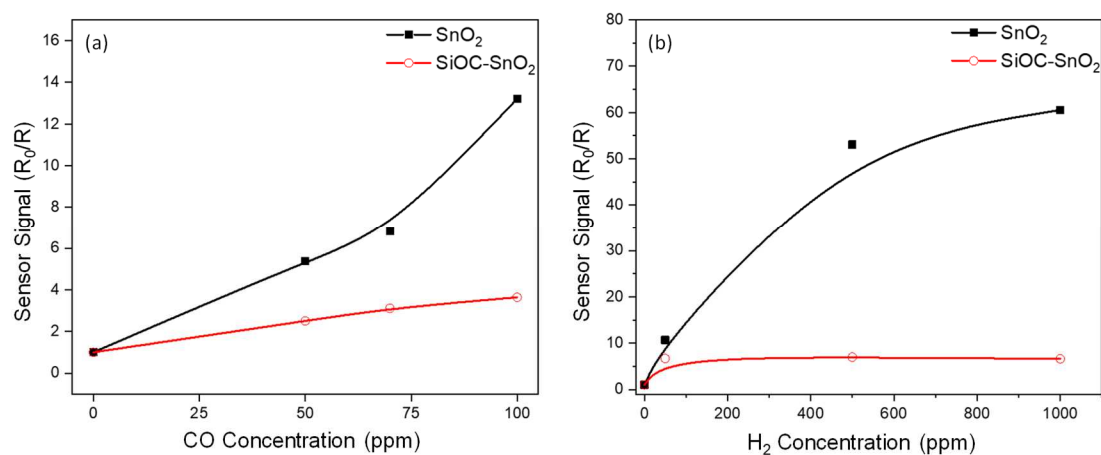
Figure A4. Sensor signal (R_o/R) of calcined RF sputtered coated SnO_2 sensor and SiOC-coated calcined RF sputtered SnO_2 sensor at 400 °C: (a) CO (50-100 ppm), (b) H_2 (50-1000); R_o is baseline resistance in N_2 and R is the resistance during target gas exposure (CO in N_2).
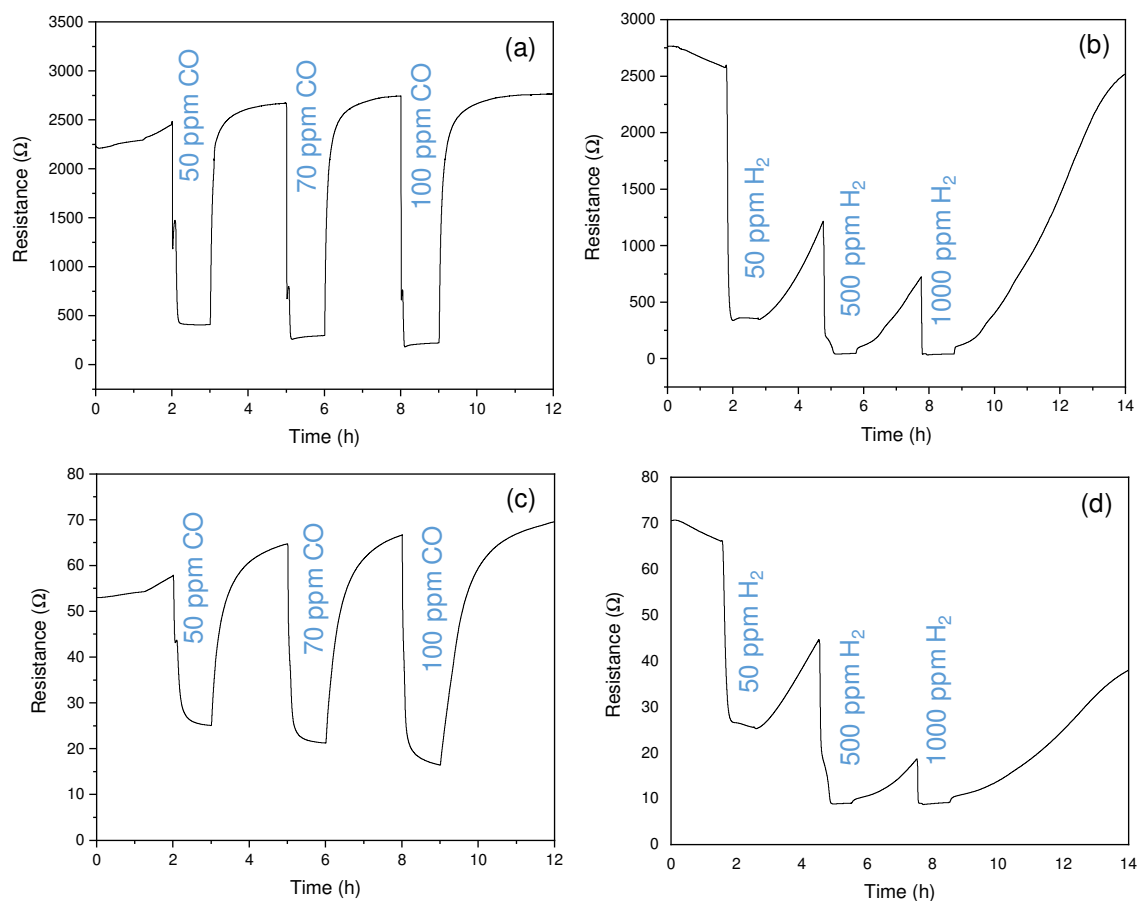

Figure A5. Transient response under CO concentrations (50, 70, 100 ppm in nitrogen), and under H_2 concentrations (50, 500, 1000 ppm in nitrogen) at 350 °C of: calcined RF sputtered coated SnO_2 sensor (a, b) and SiOC-coated calcined RF sputtered SnO_2 sensor (c,d).
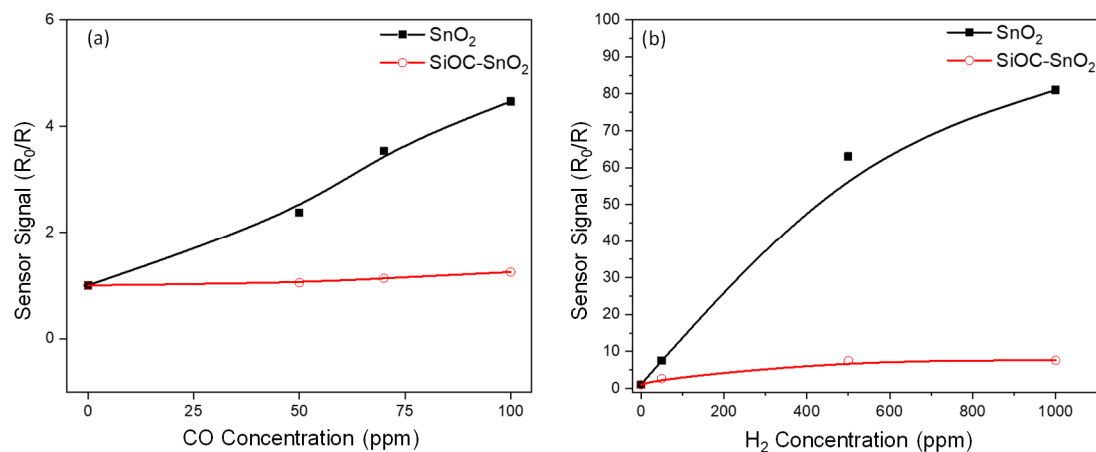
Figure A6. Sensor signal (R_o/R) of calcined RF sputtered coated SnO_2 sensor and SiOC-coated calcined RF sputtered SnO_2 sensor at 350 °C: (a) CO (50-100 ppm), (b) H_2 (50-1000); R_o is baseline resistance in N_2 and R is the resistance during target gas exposure (CO in N_2).